This is to certify that the
dissertation entitled

Study of ^{69}Br Ground State Proton Emission and
Effects on the rp-Process ^{68}Se Waiting Point

presented by

Andrew Michael Rogers

has been accepted towards fulfillment
of the requirements for the

Ph.D. degree in Physics

Major Professor's Signature

11/11/2009

Date

Study of ^{69}Br Ground State Proton Emission and Effects on the rp-Process ^{68}Se Waiting Point

By

Andrew Michael Rogers

A DISSERTATION

Submitted to
Michigan State University
in partial fulfillment of the requirements
for the degree of

DOCTOR OF PHILOSOPHY

Physics

2009

ABSTRACT

STUDY OF ^{69}Br GROUND STATE PROTON EMISSION AND EFFECTS ON THE RP-PROCESS ^{68}Se WAITING POINT

By

Andrew Michael Rogers

The rp-process determines the characteristic properties of the tail in X-ray burst lightcurves and the nucleosynthesis occurring during such events. In high temperature, hydrogen-rich environments the rp-process results from the breakout of the hot CNO cycle leading to a series of fast proton captures and β-decays involving nuclei along the proton drip-line up to masses possibly as heavy as Te. Type I X-ray bursts are thought to be key sites for this process. To realistically model the rp-process in these systems experimental data such as masses, lifetimes, and proton capture rates along the proton drip-line are required. Such data are currently lacking for many of these nuclei.

The ^{68}Se waiting point is of particular interest, where a long beta-decay half-life coupled with inhibited proton capture restricts the amount of material that is processed beyond mass 68 in the rp-process. However, the reaction rate for the 2p-capture process ^{68}Se+p $\rightarrow^{69}$Br+p $\rightarrow^{70}$Kr depends exponentially on the ^{69}Br proton separation energy and may bypass the waiting point. This separation energy is poorly constrained.

The first direct measurement of the proton separation energy for the proton unbound nucleus ^{69}Br has been performed. The newly developed MSU High Resolution Array (HiRA) and a MicroChannel Plate (MCP) beam tracking system were used for the first time together with the existing S800 spectrograph at the National Superconducting Cyclotron Laboratory (NSCL). The experiment was designed to reconstruct the decays of proton unbound nuclei, specifically ^{69}Br, by detecting the decay protons using HiRA in coincidence with a heavy residue, *e.g.* ^{68}Se, which is

measured in the large acceptance S800 magnetic spectrograph. We find that the proton separation energy of ^{69}Br is $S_p = 785^{+34}_{-40}$ keV. In addition, the influence of this new measurement on the rp-process is investigated using a one-zone X-ray burst model.

To my family,

who have supported me during this long journey ...

ACKNOWLEDGMENTS

I would like to begin by expressing my deepest thanks to my adviser Bill Lynch. His support over these past few years and his guidance have been invaluable. I will always appreciate his ability to continue to hammer away at a problem until it is understood and solved.

I would also like to thank Mike Famiano and Mark Wallace. Without their hard work and determination this dissertation would not have been possible. I am indebted to both of you.

I would like to thank all of the members of the HiRA group that I have had the pleasure of working with during my time as a graduate student. In particular, I would like to thanks Betty Tsang for all her work and encouragement. I would also like thank Vladimir and Daniela Henzl who are both wonderful and inspiring colleagues as well as an excellent pair of friends.

I would like to thank all of my collaborators that I have had the privilege to work with over the years. It was always an adventure running experiments with Lee Sobotka, Bob Charity, Jon Elson, Romualdo de Souza, and Dan Shapira. I learned a lot from all of them and I am greatly appreciative for everything they have done for me.

I would like to thank all of the laboratory staff that have contributed in so many different ways to my experiences at NSCL. I would like to thank in particular Len Morris and Ronan Fontus who were always helpful when anything needed to be designed (especially for all those parts that needed to be done now).

I would like to thank all of my friends that I have made during my time as graduate student. I would especially like to thank Karinita for making so many of my days so much brighter.

Finally, I would like to thank my family. Without the support of my parents, Mike and Marlene Rogers, and my brother Matt and sister Michelle I would not be where I am today. Whenever I needed them they were always there.

Contents

List of Tables

List of Figures

IMAGES IN THIS DISSERTATION ARE PRESENTED IN COLOR.

Acronyms

ADC analog-to-digital converter.

AME Atomic Mass Evaluation.

ASIC application specific integrated circuit.

CB chipboard.

CCF Coupled Cyclotron Facility.

CDE Coulomb displacement energy.

CDF cumulative distribution function.

CED Coulomb energy difference.

CFD pseudo-constant fraction discriminator.

COM center of momentum.

CPT Canadian Penning Trap.

CRDC cathode readout drift chamber.

CSA charge sensitive amplifier.

CSS1 first cyclotron.

CSS2 second cyclotron.

DAC digital-to-analog converter.

DAQ data acquisition.

DSSD double-sided strip detector.

EB E-back.

ECR electron cyclotron resonance.

EDF empirical distribution function.

EF E-front.

FEE front end electronics.

FPGA field-programable gate array.

FRDM Finite-Range Drop Model.

FWHM full width at half maximum.

HCNO hot CNO.

HiRA High Resolution Array.

IAS isobaric analog states.

IMME Isobaric Mass Multiplet Equation.

ISOL Isotope Separator On-Line.

LMXB low-mass X-ray binary.

MCP micro-channel plate.

NSCL National Superconducting Cyclotron Laboratory.

OBJ object plane.

PAC proposal advisory committee.

PCB printed circuit board.

PID particle identification.

PMT photomultiplier tube.

PPAC parallel plate avalanche counter.

QDC charge-to-digital converter.

SNR signal-to-noise ratio.

SSSD single-sided strip detector.

TDC time-to-digital converter.

ToF time of flight.

TPC Time Projection Chamber.

TVC time-to-voltage converter.

WKB Wentzel-Kramers-Brillouin.

XFP extended focal plane.

XLM universal logic module.

Chapter 1

Introduction

> Man is slightly nearer to the atom than to the star. ... From his central position man can survey the grandest works of Nature with the astronomer, or the minutest works with the physicist. ... Knowledge of the stars leads through the atom; and important knowledge of the atom has been reached through the stars.

Lecture 1. Stars and Atoms (1928, 2007)

SIR ARTHUR STANLEY EDDINGTON

We interact with a world made of atomic nuclei. Atoms are composed of three fermions; protons, neutrons, and electrons. Altering the numbers of protons and consequently the number of electrons in the atom results in the vastly different properties of the chemical elements as is seen throughout the periodic table. These basic building blocks give rise to much of the complexity observed within the natural world.

One of the long-standing scientific problems of our time is a fundamental understanding of the origin and evolution of the universe and the material of which it is composed. It is now known that the universe is $13.73^{+0.16}_{-0.15}$ billion years old [5]. In this vast time the matter composition of the universe has changed dramatically. Approximately 10^{-6} s after the Big Bang conditions existed in the universe that allowed for the formation of baryons such as protons and neutrons. Light nuclei soon followed after $\sim$ 10 s resulting in primordial mass fractions for hydrogen and

deuterium of $X \simeq 0.76$, ^{3}He and ^{4}He of $Y \simeq 0.24$, and all heavier elements, generically referred to as "metals", of $Z \leq 0.01$ [6]. From this initially hot, dense plasma galaxies, stars, and even planets eventually formed. The subject of nucleosynthesis describes how the matter composition of the universe has evolved from the light nuclei characteristic of the early universe into the distribution of heavy element abundances that we observe today. In general, eight processes, first suggested by Burbidge, Burbidge, Fowler, and Hoyle (B^2FH) [7], are capable of generating almost all known nuclear species. These processes are at the core of more than 50 years of investigations into the chemical evolution of the cosmos.

Both astronomical observations and nuclear physics knowledge play critical roles in quantifying and constraining the synthesis of the elements. The energy generation in stars is due to nuclear fusion, where lighter nuclei combine to form heavier ones and release energy. Stars do not live forever however. They burn, exhaust their fuel, and die, in some instances, in energetic and violent explosions known as supernova. Other violent explosions, such as novae, can also occur on white dwarfs or in the form of X-ray bursts on the surfaces of neutron stars. Evidence for the active production of the heavy elements is found, for example, in observations of short-lived ^{44}Ti, which can only be produced in supernova events [8]. In general, precise nuclear physics data is often necessary to describe the nucleosynthetic processes in such explosions and provide a quantitative modeling of the observational data obtained by astronomers. These extreme astrophysical environments can be the factories that produce the heavy elements and eventually spew them into the interstellar medium. The measurements in this dissertation can have a bearing on the rapid proton capture process in these environments and on the nucleosynthesis that occurs during X-ray bursts.

In the remainder of this chapter, some basic concepts of nuclear physics and nuclear astrophysics are discussed; the concepts are important to later chapters in

this dissertation. Section 1.1 provides an overview of the chart of nuclides and basic properties of the nuclear landscape. Subsection 1.1.1 introduces concepts relevant to nuclear masses and separations energies. Section 1.2 discusses proton emission from nuclei. Section 1.3 discusses the astrophysical rp-process and the rp-process ^{68}Se waiting-point. Section 1.4 provides a review of the previous works on the ^{68}Se waiting point and the ground state mass of ^{69}Br. Finally, Section 1.5 provides a brief outline of the remaining chapters.

1.1 Nuclear Masses and their Relevance to Nucleosynthesis

Nuclei are composed of two types of fermions, protons and neutrons, that together are called nucleons. The nucleus itself contains over 99 % of the mass of the atom. The number of protons, Z, in the nucleus defines the element. The number of neutrons, N, defines the isotope of that element. The total number of nucleons is denoted by the mass number $A = N + Z$. While in principle any number of Z protons and N neutrons can be combined, not all combinations are bound. Suppose one places points on a graph of a specific color for each combination of proton number and neutron number where a nucleus has been observed. Or, one chooses another color to label nuclei that have not been observed but may "exist" long enough to someday be observed. Then, one produces a Segre chart such as the one shown in Figure 1.1. Here, the known stable (black squares) and unstable (blue squares) nuclei are shown together with the yet unexplored regions, "Terra Incognita", shown as the red region that represents possible nuclei that may be observed in the future. We define a nucleus as *existing* if it has a lifetime on the order of milliseconds since unbound nuclei typically have lifetimes shorter than this. In general, this means that the nucleus decays by β-decay, or in the case of heavy nuclei, by α-decay. Energetically, unstable nuclei try to minimize their energy through decay to the stable nuclei and, eventually, reach the "β-stable valley of stability."

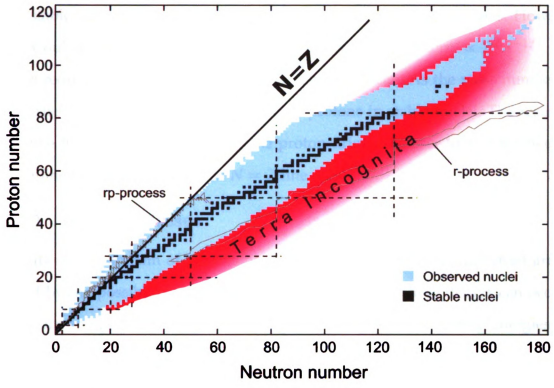

Figure 1.1 – Segre chart. (Original image from NSCL INTRA image repository)

There are a number of fundamental issues that govern the trends displayed by Figure 1.1. First, for a fixed stable Z, neutrons can be added or removed making heavier or lighter isotopes, respectively, until one creates nuclei that have no bound states. At the limits where the least bound nucleon is energetically unbound (negative separation energies) the nuclei are very short lived. Such nuclei decay by proton emission if they are at the left boundary and by neutron emission if they are at the right boundary. These boundaries are often called the proton and neutron drip-lines, respectively.

Clearly, the drip-lines on the Segre chart are not symmetric with respect to the $N = Z$ line, indicating differences in the properties of the proton and neutron. These differences are mainly due to the symmetry and Coulomb energies. The symmetry energy, which is $\propto (N - Z)^2 A^{-1}$, tends to increase the binding for nuclei with the same number of neutrons and protons. This is the case for the light-

est stable nuclei which have equal numbers of neutrons and protons. However, the Coulomb repulsion of the protons brings in an energy term $\propto Z^2 A^{-1/3}$. This term reduces the binding energy for proton-rich nuclei. As the mass number, A, increases so does the ratio of neutrons to protons in stable nuclei. The resulting change in Coulomb energy shifts the proton drip-line closer to and the neutron drip-line farther away from the $N = Z$ line.

1.1.1 Nuclear Masses

Limits on the domain of particle bound nuclei shown by the Segre chart are defined by the possibility of proton and neutron decays. These decays can occur if they are energetically allowed; this is governed by nuclear binding energies, *i.e.*, by the masses of nuclei. Nuclear and atomic masses are intimately tied to model calculations of the rp-process. Consequently, these concepts will be defined in this section, and are key to the remainder of this chapter and to this dissertation as a whole. Furthermore, this dissertation focuses on the experimental determination of the ^{69}Br proton separation energy which is equivalent to the ^{68}Se(p,γ) ground state capture Q-value. When combined with recent measurements of the mass of ^{68}Se, the proton separation energy yields the mass of ^{69}Br. These quantities are defined in this section. In addition, one may estimate masses using calculations of the Coulomb energy differences between "mirror nuclei." This relationship will also be discussed.

Masses, Binding Energies, and Q-Values

The invariant mass, m, for a single particle is defined by the well known relation,

$$mc^2 = E^2 - |\vec{p}c|^2 \tag{1.1}$$

where E is the total energy of the particle and $\vec{p}$ is its spatial momentum. This relationship is true regardless of whether the particle is point-like or a composite system composed many elementary particles. For a composite system the invariant mass, Mc^2, includes contributions from the internal energy of its components as well as from any fields, such as the Coulomb, or nuclear mean fields which contribute to its binding. Consequently, the invariant mass of a composite system will in general be different from the sum of the individual masses of which it is composed.

For a neutral atom with Z protons and N neutrons the atomic mass is defined as,

$$M_{\mathrm{A}}(Z,N)c^2 = Z(M_{\mathrm{p}} + M_{\mathrm{e}})c^2 + NM_{\mathrm{n}}c^2 - BE(Z,N) \tag{1.2}$$

where $BE(Z,N)$ is the total binding energy of the atom and M_{e}, M_{p}, and M_{n} are the free electron, proton, and neutron masses respectively. In addition, the nuclear mass can be given in terms of the atomic mass by,

$$M_{\mathrm{Nuc}}(Z,N)c^2 = M_{\mathrm{A}}(Z,N)c^2 - ZM_{\mathrm{e}}c^2 + BE_{\mathrm{e}}(Z) \tag{1.3}$$

where $BE_{\mathrm{e}}(Z)$ is the binding energy of the electrons and M_{e} is the free electron mass. Generally, unless otherwise stated, most mass tables use atomic masses as opposed to nuclear masses. It should be noted that the atomic binding energy is small compared to the nuclear binding energy. For the purposes of this dissertation one can calculate nuclear masses using the formula for the electron binding energy from Lunney, Pearson, and Thibault [9],

$$BE_e = 14.4381 \cdot Z^{2.39} + 1.554\,68 \times 10^{-6} \cdot Z^{5.35}\ \mathrm{eV} \tag{1.4}$$

as is suggested by the Atomic Mass Evaluation (AME) 2003 [10].

For calculating the energetics of nuclear reactions the atomic mass excess, $\Delta(Z,N)$, is a useful quantity,

$$\Delta(Z,N) = [M_A(Z,N) - AM_u]c^2 \tag{1.5}$$

$$= [M_A(Z,N)[\text{amu}] - A] \cdot 931.478\,\text{MeV}. \tag{1.6}$$

Here, M_u is the atomic mass unit and is defined to be 1/12 the mass of a neutral ^{12}C atom. In a reaction of the type 1+2 $\rightarrow$ 3+4 the Q-value, or the energy absorbed or released in the reaction, is given by the difference of initial and final atomic masses,

$$Q = (M_1 + M_2 - M_3 - M_4)c^2 \tag{1.7}$$

$$= \Delta_1 + \Delta_2 - \Delta_3 - \Delta_4 \tag{1.8}$$

where the Δ_i's are the respective atomic mass excesses. If the total nuclear charge changes as it does in the case of β-decay, then one must calculate the Q-value from the nuclear masses. As this dissertation is focused mainly on (p,γ) ground state capture Q-values we have,

$$Q_{\text{p},\gamma} = [M(Z,N) + M_H - M(Z+1,N)]c^2 \tag{1.9}$$

Finally, we can define the proton separation energy as the energy required to remove a proton from the nucleus and take it out to infinity,

$$S_p(Z,N) = BE(Z,N) - BE(Z-1,N) \tag{1.10}$$

$$= [-M(Z,N) + M(Z-1,N) + M_H]c^2 \tag{1.11}$$

$$= -Q_p \tag{1.12}$$

$$= Q_{p,\gamma}. \tag{1.13}$$

In case of proton decay from the ground state, the separation energy is equal in magnitude but opposite in sign to the ground state *proton decay* Q-value, Q_p. However, the *proton capture* Q-value, $Q_{p,\gamma}$, is equivalent to the proton separation energy.

Coulomb Energy Differences (CED)

This method of determining masses relies on the isospin independence or invariance of nuclear forces [11]. In the isospin formalism, the proton and neutron are treated as two states of a nucleon (Isospin is completely analogous to spin). All nucleons are assigned an isospin of $t = 1/2$, where the 3rd component of the isospin vector determines whether the nucleon eigenstate is a proton ($t_z = -1/2$) or a neutron ($t_z = +1/2$). The total isospin quantum number, T, of a nucleus is the magnitude of the vector sum of the individual nucleon isospins. The group theory formalism for isospin is similar to spin: one constructs corresponding T^+ (raising) and T^- (lowering) operators acting within isospin space. The isospin operators commute with the strong interaction part of the Hamiltonian. If one operates with T^- on an eigenstate of a nucleus with (Z,N), one either creates an eigenstate of the nucleus with proton number $Z+1$ and neutron number $N-1$ or zero. The latter occurs when the orbit of the new proton that would be converted from a neutron by the operator T^- is already occupied. T^+ and T^- do not change A or the total isospin T. These operators only convert states in the same isospin multi-

plet, *i.e.*, states with the same isospin quantum number, T. Such states are known as isobaric analog states (IAS). Additionally, the 3rd component of total isospin, $T_z = (N - Z)/2$, defines the nucleus with mass number A.

The nuclear part of the binding energy is the same for two analog energy states in neighboring nuclei because T commutes with the strong interaction Hamiltonian. The Coulomb part of the binding, however, does not: energy differences between the same IAS in neighboring nuclei are due to isospin non-conserving interactions (particularly the Coulomb interaction). These energy differences are generally known as the Coulomb energy difference (CED)*. The Coulomb displacement energy (CDE), $D(T, T_z, k)$, refers to the total binding energy difference between any two members of an isospin multiplet,

$$D(A, T_z, k) = BE(A, T_z + k) - BE(A, T_z) \tag{1.14}$$

$$= M(A, T_z)c^2 - M(A, T_z + k)c^2 + k\Delta_{\mathrm{nH}}c^2. \tag{1.15}$$

where k is the number of protons exchanged for neutrons, T_z is the projection of the nucleus with the largest Z, and Δ_{nH} is the neutron-Hydrogen atomic mass difference [13]. The binding energy of ^{69}Br can therefore be predicted from the known binding energy for ^{69}Se by calculating

$$BE(^{69}\mathrm{Br}) = BE(69, T_z = -\frac{1}{2}) = BE(69, T_z = \frac{1}{2}) - D(69, T_z = -\frac{1}{2}, 1) \tag{1.16}$$

The atomic mass for ^{69}Br is,

$$M(^{69}\mathrm{Br})c^2 = M(^{69}\mathrm{Se})c^2 + D(69, T_z = -\frac{1}{2}, 1) - \Delta_{\mathrm{nH}}c^2 \tag{1.17}$$

* A thorough review of Coulomb energy differences can be found in [12].

and the proton separation energy for ^{69}Br is,

$$S_p = M(^{68}\mathrm{Se})c^2 - M(^{69}\mathrm{Br})c^2 + M_H c^2 \tag{1.18}$$

$$= D(69, T = -\frac{1}{2}) - \Delta_{nH}c^2. \tag{1.19}$$

As will be discussed in Section 1.4, calculations of the Coulomb displacement energy (CDE) have been used to predict the ^{69}Br mass in many previous studies.

The fundamental importance of CDEs and their application to extracting nuclear structure information has resulted in extensive theoretical studies. Most notably, CDEs for a number of experimentally known isobaric analog states (IAS) were calculated in the review of Nolen and Schiffer [12]. In their calculations Nolen and Schiffer initially included the three most dominant terms to the CDE: the direct, exchange, and electromagnetic spin-orbit terms (the electromagnetic spin-orbit term will be discussed in more detail in Section 4.6). However, these calculations were unable to account for the full Coulomb displacement energies determined from the experimental data. Additional "correction" terms were then calculated which included Coulomb perturbation, spreading width, nuclear rearrangement, isospin impurities in the core, intrashell interactions, and correlation terms; but even then there was still, on the average, a $\sim 7\%$ under-estimate of the CDE [13]. This under-estimate of the CDE, which persists to this day, is know as the *Nolen-Schiffer Anomaly*. In the discussions based on CDEs that follow in this dissertation it should be kept in mind that while there have been improvements in the theoretical calculations, some contributions still remain poorly understood.

1.2 Proton Emission from Nuclei

Moving away from the valley of stability toward more proton-rich nuclei we find that β^+-decay is usually the favored decay mode. However, as one approaches the proton drip-line, the nuclear force is no longer able to bind the last proton. As

the proton becomes more unbound, decay by emission of a proton can compete with β^+-decay. In some nuclei it becomes the dominant mode of decay. The balance between these two decay modes depends sensitively on the Coulomb and centrifugal barriers. Moreover, in certain cases, decay by two-proton emission is also possible [14].

Decay by proton emission, sometimes referred to as proton radioactivity*, was first outlined in a review by Goldanskii [15]. While proton emission from long-lived excited states has been investigated since the 1970s in ^{53m}Co† [16], the first clear experimental evidence for ground state decay, the decay of ^{147}Tm [17], was not found until the early 1980s. Subsequent discoveries of proton emission from ^{151}Lu [18], ^{113}Cs, ^{109}I [19], and eventually other exotic heavy isotopes like ^{117}La [20] and ^{135}Tb [21] have motivated additional measurements. Today, experiments have identified approximately 25 ground state proton emitters [22]. Their properties are mostly well understood theoretically [23, 24] and, since p-decay is similar to α-decay, reasonably accurate estimates of decay lifetimes can often be made [25].

The decay rates for proton emission from proton-rich nuclei near the drip-line is almost completely determined by quantum mechanical tunneling through the Coulomb barrier. Protons, unlike neutrons, even at unbound energies ($E > 0$), are still confined by the Coulomb barrier. Classically, protons with energies less than the height of the Coulomb barrier would not be emitted; the nucleus would therefore only undergo β-decay. However, as illustrated in Figure 1.2, quantum mechanics allows the unbound proton to tunnel through the "classically forbidden" region and be emitted as proton radioactivity. The tunneling penetrability is determined by the width and height of the barrier through which the proton must tunnel. For unbound protons with energies near the barrier momentum the barrier is thin and the tunneling time is short. At much lower proton energies the proton must tunnel

* This is actually a slightly deceptive term as it implies that it is the proton that is undergoing decay.
† The letter "m" denotes that the nucleus was in an excited *isomeric* state.

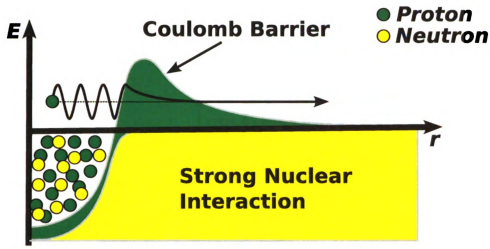

Figure 1.2 – Illustration of quantum tunneling of a proton through the Coulomb barrier. Neutrons, unlike protons, are charge neutral and are only confined by the strong nuclear interaction.

through a thick barrier due to the long $1/r$ tail of the Coulomb interaction. This reduces the penetrability so much that β-decay can be the dominant decay mode even when the nucleus is energetically unbound with respect to proton decay.

1.3 rp-Process

While certain processes, like the r and s process, proceed mainly through neutron captures some processes proceed mainly through proton captures. Nucleosynthesis processes that burn hydrogen synthesize elements only accessible from the proton-rich side of the valley of stability. In particular, the rp-process (rapid proton capture process) has been identified as a possible contributor to the light nuclei abundances as well as elements beyond the iron group. The formal description of the rp-process was initially detailed by Wallace and Woosley [26]. It occurs following the breakout from the hot CNO (HCNO) cycle and is characterized by rapid proton captures on seed nuclei that drive the composition towards the proton dripline interspersed with β-decays that drive the composition toward the valley of β-stability. The nuclear energy generated during the rp-process is thought to power the light curves in explosive hydrogen burning events in sites where the rp-process

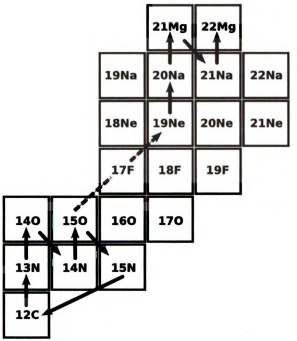

Figure 1.3 – Hot CNO cycle and breakout through $^{15}O(\alpha,\gamma)^{19}Ne$.

is expected to occur, such as Type I X-ray bursts. However, modeling of the rp-process path and the abundances of nuclei, especially those heavier than Fe, are limited by uncertainties in the nuclear physics of the involved nuclei.

In principle, all allowed decay and capture processes between nuclear species can occur during stellar burning. However, the conditions of the system (*i.e.*, temperature, density, composition, etc.) and nuclear properties dictate which processes dominate. In hot hydrogen rich environments where temperatures exceed 8×10^7 K hydrogen burns in the HCNO cycle [27, 28],

$$^{12}C(p,\gamma)^{13}N(p,\gamma)^{14}O(\beta^+)^{14}N(p,\gamma)^{15}O(\beta^+)^{15}N(p,\alpha)^{12}C \qquad (1.20)$$

as shown in Figure 1.3 and can be the major source of energy production. At temperatures exceeding 5×10^8 K the reactions $^{15}O(\alpha,\gamma)^{19}Ne$ and $^{18}Ne(\alpha,p)^{21}Na$ allow "breakout" from the HCNO cycle. Proton capture on ^{19}Ne removes it from the HCNO cycle and allows the production of heavier masses via rapid proton cap-

tures. These captures, however, are limited by the proton drip-line, β^+-decay rates, and the abundance of protons. In addition, as Z increases so does the Coulomb barrier that charged particles must overcome. This reduces the capture rates for higher masses which is especially relevant to any α induced reactions. On nuclei along the rp-process path proton capture can be inhibited by Q-values or Coulomb barriers. If these nuclei have long β-decay half-lifes compared to proton capture rates or β-decay rates of other nuclei in the process, they are called waiting-point nuclei. This is because the capture process has to wait for the relatively slow β-decay, resulting in large abundances of nuclei accumulating at these points.

While a number of rp-process sites have been proposed [29,30] one of the most likely scenarios are Type I X-ray bursts found in low-mass X-ray binary (LMXB) systems. A LMXB is formed in a system with a typically low mass companion in orbit with a compact stellar object such as a neutron star. Matter that becomes gravitationally unbound from the companion star is transferred to the compact object [27]. A persistent flux of X-rays is observed from such systems due to the conversion of gravitational potential energy of the infalling material. The composition of the accreted material is typically rich in both hydrogen and helium, which is the thermonuclear fuel for the burst. Eventually, the accreted fuel accumulates on the neutron star surface where it is compressed and heated to high temperatures ($T \geq 0.5 \times 10^9$ K) and densities ($\rho \gtrsim 10^4\,\mathrm{g\,cm^{-3}}$) [31]. This environment provides the necessary conditions for helium to ignite due to a thin shell instability in which the layer is heated more efficiently than it can cool and the burning becomes extremely temperature sensitive. The resulting release of nuclear energy is observed as a large transient increase in the X-ray luminosity.

These sudden energetic X-ray burst events are capable of generating $\sim 10^{39}$ ergs of energy or more and have been observed with X-ray observatories such as Chandra and XMM-Newton. The observed X-ray flux typically has a short rise time on

the order of 1 s driven by the initial unstable helium burning. As the initial explosive burning ends, the αp and rp-processes, responsible for the extended energy generation in the tail of the burst profile, produce heavy nuclei. The duration of these bursts are found to be typically on the order of $\sim$ 10 s to 100 s. This implies that any nucleosynthesis process must occur on a timescale of this order. Furthermore, if the accretion of material continues, these bursts may occur periodically with recurrence times typically on the order of hours or days. The properties of the burst depend critically on the accretion rate, composition of the accreted material, and the composition of the surface layers of the neutron star. Since these bursts reoccur, incomplete burning will contribute "ashes" from previous bursts to the initial composition of the next burst [32,33].

In regard to rp-process nucleosynthesis, it may be possible to reconcile large observed overabundances of certain $A \sim 80 - 100$ nuclei and account for the solar abundance of a number of nuclei, such as ^{92}Mo and ^{96}Ru [27,34], that cannot be produced in the p-process. The ejection of only $\sim$ 0.3 % of the ashes produced via the rp-process in type I X-ray bursts would be needed to account for the solar abundance patterns* [31]. The possibility of processing material as high as Te has also been proposed [35] although it is uncertain as to how plausible this actually may be [36]. Furthermore, it is thought that no material will escape from the X-ray burst due to the large gravitational potential of the neutron star [26]. If another site for the rp-process is found where the gravitational potential can be overcome this issue could be resolved.

1.3.1 ^{68}Se Waiting Point

Waiting points along the rp-process path significantly control the abundance flow from lighter to heavier masses along the proton drip-line. The ^{64}Ge, ^{68}Se, and ^{72}Kr

* The ejection factor (escape factor) was estimated using assumptions about abundance overproduction factors, total galactic nucleosynthesis time, and the galactic disk mass as well as X-ray burst birth rate, system lifetime, and mass transfer rate [31].

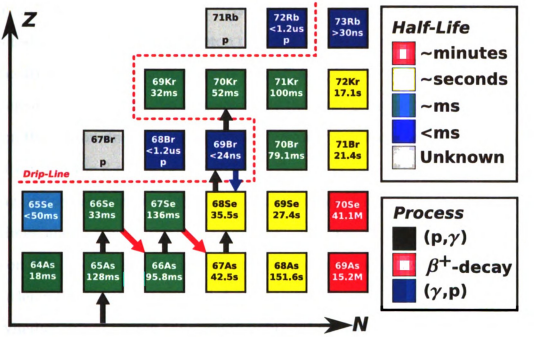

Figure 1.4 – ^{68}Se waiting-point region of the nuclear chart.

waiting points are keys to understanding the amount of material that can be processed through this region and ultimately affect the observed properties of astrophysical events such as X-ray bursts. In particular, the ^{68}Se waiting point has been an intense source of interest, both from astrophysical and nuclear structure points of view. Its long β^+-decay half-life combined with its Q-value inhibited proton capture rates greatly reduces processing isotopes to Kr and above. However, the waiting point may be bypassed through 2p-captures to ^{70}Kr [31], potentially altering the final isotopic abundances significantly. The extent to which this occurs depends exponentially on the ^{68}Se(p, γ)^{69}Br Q-value.

Following the general rp-process flow, under the correct conditions, into the Se region one finds a large fraction of the matter contained in ^{68}Se nuclei. As illustrated in Figure 1.4, proton captures through the ^{64}Ge waiting point (^{64}Ge(p, γ)^{65}As) reach ^{66}Se just below the proton drip-line. Proton captures on ^{66}Se produce ^{67}Br which is believed to be sufficiently proton unbound that it will immediately decay by proton emission. The abundance flow of ^{66}Se will instead proceed through β-

decay to ^{66}As. Proton captures on ^{66}As produce ^{67}Se, which also eventually undergoes β-decay to ^{67}As because proton captures to ^{68}Br are expected to be inhibited by the drip-line. Proton capture reactions on ^{67}As generate ^{68}Se: proton captures on ^{68}Se are again expected to be suppressed by the large Q-value characteristic of nuclei on the proton drip-line. If proton capture on ^{68}Se cannot occur, the rp-process must wait for the β-decay of ^{68}Se to ^{68}As ($T_{1/2} = 35.5$ s) in order to continue capturing protons and processing to higher masses. The ^{68}Se lifetime is comparable to the timescale ($\sim$ 10 s to 100 s) for a typical X-ray burst. So, the rate for proton capture on ^{68}Se, though small, may be a significant factor in allowing the generation of nuclei in the rp-process beyond $A \approx 68$.

Whether or not proton captures to unbound nuclei like ^{69}Br play a role in the rp-process depends closely on details of the locations and excitation energies of the low-lying levels in the unbound ^{69}Br nucleus, and the structure of these states. In principle, the existence of low-lying states in ^{69}Br means that, given sufficient hydrogen, ^{68}Se, and sufficient time a second proton can be sequentially captured on an equilibrium abundance of ^{69}Br to produce ^{70}Kr, which is bound. As the ^{70}Kr β-decay half-life is relatively short ($T_{1/2} = 52$ ms) this opens an additional channel through which the ^{68}Se waiting point can be effectively bypassed, allowing the rp-process to continue to heavier masses without waiting for the β-decay of ^{68}Se.

The role of 2p-capture reactions in X-ray bursts was first thoroughly investigated by Schatz *et al.* [31]. Here, they derived the approximate stellar 2p-capture reaction rate (for $T \lesssim$ 1.5-2.0 GK) in terms of the proton capture Q-value and temperature as,

$$\lambda_{2p} = Y_p^2 \rho^2 N_A^2 \left(\frac{2\pi\hbar^2}{kT}\right)^{3/2} \frac{G_{(Z+1,N)}(T)}{2G_{(Z,N)}(T)} \exp\left(\frac{Q_{(Z,N)}(p,\gamma)}{kT}\right) \langle p,\gamma\rangle_{(Z+1,N)} \quad (1.21)$$

where Y_p is the proton abundance, ρ is the density, $G_{(Z+1,N)}(T)$ and $G_{(Z,N)}(T)$ are the partition functions, N_A is Avogadro's number, and $\langle p,\gamma\rangle_{(Z+1,N)}$ is the reaction rate for the second proton capture. The exponential whose argument is the Q-value, or equivalently the proton separation energy ($Q_p = -S_p$), dominates the dependence of the reaction rate.

The effects on the abundance at the ^{68}Se waiting point can be crudely illustrated by considering its effective half-life. Further processing in the rp-process is directly related to how much ^{68}Se is destroyed. Taking into account the destruction of ^{68}Se through β-decay and proton capture to ^{69}Br the effective destruction rate for ^{68}Se (for $T \lesssim 1.5$-$2.0\,\mathrm{GK}$) in the stellar environment is [31],

$$\lambda_{\mathrm{eff}} = \lambda_\beta + {Y_p}^2 \rho^2 {N_A}^2 \left(\frac{2\pi\hbar^2}{kT}\right)^{3/2} \frac{G_{\mathrm{Br}}(T)}{2G_{\mathrm{Se}}(T)} \exp\left(\frac{S_p}{kT}\right) \langle\sigma v\rangle_{\mathrm{Br}}. \tag{1.22}$$

Here, λ_β is the ^{68}Se β-decay rate, Y_p is the proton abundance, ρ is the density, G_{Br} and G_{Se} are the respective Br and Se statistical factors involving spin, and $\langle\sigma v\rangle_{Br}$ is the reaction rate for proton capture on ^{69}Br. The effective half-life,

$$t_{1/2}^{\mathrm{eff}} = \frac{\ln(2)}{\lambda_{\mathrm{eff}}} \tag{1.23}$$

of ^{68}Se for a density ($\rho = 1 \times 10^6\,\mathrm{gm/cm^3}$) and temperature ($T = 1.5\,\mathrm{GK}$) of a typical X-ray burst, as well as for a variety of possible desities and temperatures, is shown in Figure 1.5. For the most unbound separation energies no ^{69}Br will be produced through proton capture and the effective half-life of ^{68}Se remains at its β-decay value of 35.5 s. As the separation energy becomes more positive the exponential term begins to dominate, very rapidly destroying ^{68}Se below $\sim$500 keV. Clearly, the proton separation energy has a drastic effect on the lifetime of ^{68}Se in the stellar environment of an X-ray burst, quickly varying by orders of magnitude.

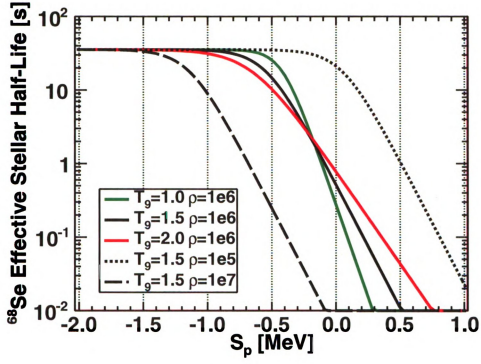

Figure 1.5 – Effective stellar half-life of ^{68}Se as it depends on the ^{69}Br proton separation energy for various relevant temperatures and densities. Here, ^{68}Se is removed from the stellar environment either through β-decay or ^{68}Se$(p,\gamma)^{69}$Br capture reactions. (The temperature is given in units of GK and the density in units of gm/cm^3.)

This illustrates the need for precise measurements with minimum uncertainties of key Q-values along the rp-process path.

1.4 Previous Studies and Observations

Over the past two decades a significant number of studies have been undertaken and a large amount of effort devoted to searches and measurements on ^{69}Br as well as nuclei at the proton drip-line. The first experiments simply attempted to prove the existence of ^{69}Br while at the same time allowing limits to be set on its lifetime. In later experiments predictions for the mass of ^{69}Br and its proton separation energy were determined indirectly through measurements on the masses of ^{68}Se and ^{69}Se. Intimately coupled with these experiments are systematic and theoretical studies that in general attempt to predict properties of nuclei for regions of the nuclear chart where experimental data are lacking. Currently, the most re-

cent and precise predictions for the ^{69}Br mass utilize high precision Penning trap measurements of both ^{68}Se and ^{69}Se together with theoretical calculations for the Coulomb displacement energy (discussed in Equation 1.1.1). This results in estimated uncertainties on the order of 100 keV. Therefore, in light of these previous endeavors, a brief review is in order.

1.4.1 First Attempts

The boundaries of the nuclear landscape are defined by the proton and neutron drip-lines. Interestingly, the lifetimes of certain unbound nuclei can be exceedingly long compared to the orbital period of a nucleon within the nucleus. The additional presence of the Coulomb barrier confines the proton to the nucleus, significantly increasing its lifetime as mentioned in Section 1.2. Thus, such nuclei can be considered to "exist" as a coherent object.

In the past predictions for the location of the proton drip-line and, at the time, recent discoveries of ground state proton emission from ^{109}I, ^{113}Cs [19], ^{147}Tm, ^{150}Lu [37], and ^{151}Lu [18, 38] prompted studies into possible ground state proton emission from ^{69}Br [39]. One of the earliest attempts was carried out by Hourani *et al.* [40]. The experiment, conducted at the Orsay Tandem accelerator, sought to produce ^{69}Br through fusion residues. The residues were then implanted in an ionization chamber which was used to search for protons in an energy range of 250-600 keV. However, they did not observe any protons with the expected energy and were able to exclude a range of 10 μs-100 ms for the ^{69}Br proton decay half-life. Shortly after, Robertson *et al.* [39] reported results from a similar experiment involving the bombardment of ^{28}Si and ^{32}Si on a natural calcium target at the Berkley 88-inch Cyclotron. Fusion residues were implanted on a rotating catcher wheel and protons were measured and identified using a telescope composed of a gas energy loss (ΔE) detector followed by a 300 μm Si E detector. Again, no proton

groups were detected in the expected energy range and a complimentary upper limit for the proton decay half-life of 100 μs was obtained.

Following this, Mohar *et al.* [41] reported the first direct observation of ^{69}Br. They investigated the production of isotopes in the projectile fragmentation of a ^{78}Kr beam using the A1200 magnetic analyzer at the National Superconducting Cyclotron Laboratory (NSCL). In their fragment identification spectra they observed 7 events which they attributed to ^{69}Br. Subsequent measurements by other groups could not confirm this result and it is generally believed to be incorrect.

1.4.2 Recent Predictions by Non-Observation

Following the claim of observation of ^{69}Br and the first searches for proton emission, improved fragmentation experiments were carried out. The first of these was conducted by Blank *et al.* [42] who also investigated the production of proton-rich isotopes in the projectile fragmentation of ^{78}Kr at the SISSI/LISE facility at GANIL. In this case the yields of other produced nuclei in the region surrounding ^{69}Br were significantly higher compared to the results of Mohar *et al.* [41], yet no events were found that could be attributed to ^{69}Br. Consequently, it was concluded that the proton half-life of ^{69}Br is < 100 ns which, given a simple barrier penetration calculation, translates into a proton separation energy of $S_p \leq -450$ keV. However, the GANIL experiment differed significantly from Mohar *et al.* [41] in that the flight path from the production target to the particle detectors was approximately 6 times longer. This means that the results of Mohar *et al.* [41] were not necessarily contradicted since a half-life of 100 ns would allow a small number of ^{69}Br nuclei to reach the detectors in the A1200.

Further investigations into the fragmentation of ^{78}Kr were again conducted at NSCL using the A1200 by Pfaff *et al.* [43]. This experiment aimed to improve upon the measurement of Mohar *et al.* [41]. However, with a similar setup and increased

statistics no ^{69}Br nuclei were observed, in contradiction with the previous result from Mohar *et al.* Assuming the previously measured cross sections of Mohar *et al.* for the produced Br isotopes, 300 counts of ^{69}Br were expected but not observed. This absence of ^{69}Br nuclei and the 14 m flight path of the A1200 separator suggests a half-life upper limit of 24 ns for ^{69}Br. Following Blank *et al.* [42], one can estimate from this value of the half-life combined with a barrier penetration calculation that the ^{69}Br proton separation energy is ≤ -500 keV. Throughout this dissertation the value of $S_p \leq -500$ keV will be taken as a reasonable upper limit on the proton separation energy.

1.4.3 Recent Predictions by Indirect Methods

While the experiments discussed in Subsection 1.4.1 and Subsection 1.4.2 are capable of establishing upper limits on the half-life of ^{69}Br, they provided little else. A precise measurement of the proton separation energy would provide more definitive information about the ^{68}Se waiting-point (see Subsection 1.3.1). As shown by Equation 1.21, the astrophysical reaction rate depends exponentially on the ^{68}Se(p,γ) capture Q-value; relatively small uncertainties in the Q-value lead to large variations in the 2p-capture process. Recent measurements have focused on obtaining and improving mass measurements for ^{68}Se and ^{69}Se [44, 45, 46, 2, 3]. When combined with theoretical calculations these increasingly precise mass measurements have led to predictions for the mass of ^{69}Br (and equivalently the proton separation energy) with significantly reduced uncertainties. These predictions, however, are less reliable than a direct experiment as they fundamentally rely on the accuracy of the calculated mass difference between ^{69}Br and ^{69}Se.

In part, because the rp-process in general depends heavily on many experimentally undetermined properties of nuclei close to the proton drip-line, a large number of studies have provided predictions for masses, binding energies, and

separation energies for nuclei that have not been measured experimentally. For example, the 1995 [47,48] and 2003 [49,10] Atomic Mass Evaluation (AME) systematic studies are often implemented in astrophysical simulations that require the knowledge of unknown masses. In addition, there are other ways to estimate the masses such as the Isobaric Mass Multiplet Equation (IMME), the Finite-Range Drop Model (FRDM) of Möller *et al.* [50,51], and various coulomb displacement calculations [52,1], which use the available experimental data to provide estimates for unknown masses.

Soon after the fragmentation experiments of Mohar *et al.* and Pfaff *et al.*, the first mass measurements of ^{68}Se were reported by both Lalleman *et al.* [44] and Lima *et al.* [45]. These experiments used very different techniques. The experiment of Lalleman *et al.* [44] produced ^{68}Se through fusion-evaporation reactions in the bombardment of a ^{12}C foil with a ^{56}Ni beam accelerated in the first cyclotron (CSS1) at GANIL. The residues of fusion-evaporation were then injected into the second cyclotron (CSS2), which was used as a mass spectrometer. A mass excess of $\Delta M = -52\,347(80)$ keV was reported corresponding, when taken together with AME 2003 and Coulomb displacement [1], to a proton separation energy of $S_p = 1072(190)$ keV. This value implied that ^{69}Br would be bound, but is in disagreement with more recent mass measurements of ^{68}Se.

The experiment of Lima *et al.* [45] utilized the high-resolution energy loss spectrometer SPEG, also located at GANIL, to perform mass measurements of proton-rich isotopes using a time of flight (ToF) method. The ^{68}Se nuclei were produced by fragmenting a ^{78}Kr beam on a ^{nat}Ni target. Masses were obtained for the produced fragments from the relation $M/Z = T_f B\rho/(L\gamma)$ which relates the mass, M, and charge, Z, of the transmitted ion to the magnetic rigidity, $B\rho$ (where B is the magnitude of the magnetic field and ρ is the bending radius of the magnetic system), of the spectrometer, the flight path length, L, and the ToF of the ion, T_f. A mass

excess of $\Delta M = -53\,620(1000)$ keV was determined for ^{68}Se. Furthermore, Lima *et al.* [45] reported a proton separation energy of $S_p = 80(1030)$ keV.

These mass measurements have been recently superseded by high-precision mass measurements using Penning traps. A new mass measurement of ^{68}Se performed by Clark *et al.* [46] using the Canadian Penning Trap (CPT) greatly reduced its uncertainty. They reported a ^{68}Se mass excess of $\Delta M = -54\,232(19)$ keV corresponding to a predicted ^{69}Br proton separation energy of $S_p = -813(129)$ keV when taking the ^{69}Br mass estimated by the Coulomb displacement energy differences of [1] discussed in Equation 1.1.1. Additional measurements of the LEBIT group at NSCL for the mass of ^{69}Se by Schury *et al.* [2] and a remeasurement of ^{68}Se by Savory *et al.* [3] improved the overall accuracy of masses in the region. The measurement of ^{69}Se with a reported mass excess of $\Delta M = -56434.6(1.5)$keV differs by 135 keV from the AME 2003 result, which has a significant effect on the predictions for the ^{69}Br mass previously provided by the AME value. Finally, with the mass excess of ^{68}Se found to be $\Delta M = -54\,189.3(5)$ keV a prediction for the mass of ^{69}Br, using the mass of ^{69}Se and the Coulomb displacement energy calculations of reference [1], yield an estimate of $S_p = -636(100)$ keV for the proton separation energy of ^{69}Br. Until the present data, this was probably the best estimate for the value of this quantity.

1.4.4 Summary

The measurements of the previous section are summarized in Table 1.1. It is clear from the table that these attempts have provided a relatively large spread in predicted ^{69}Br proton separation energies with large varying uncertainties. If one combines the recent LEBIT Penning trap mass measurements of ^{68}Se and ^{69}Se with theoretical Coulomb displacement calculations, as discussed in the preceding section,

S_p [keV]	Error [keV]	Data Type	Comments
<-450	-	Non-Obs. [42]	$T_{1/2} < 100$ ns †
<-500	-	Non-Obs. [43]	$T_{1/2} < 24$ ns
+1072	190	Exp. [44]	CSS2 ^{68}Se mass measurement §
-201	1110	Exp. [45]	SPEG ^{68}Se mass measurement §
-813	129	Exp. [46]	CPT ^{68}Se mass measurement †
-766	350	Exp. [53]	β-endpoint ^{68}Se mass
-679	119	Exp. [2]	LEBIT ^{69}Se mass measurement
-636	105	Exp. [3]	LEBIT ^{68}Se mass measurement †
-451	610	Syst. [47]	AME 1995 †
-450	100	Syst. [10]	AME 2003
+89	-	Theory	FRDM †
-663	305	Theory [52]	CD
-730	320	Theory [1]	CD/Skyrme Hartree-Fock

Table 1.1 – Previous predictions for the ^{69}Br proton separation energy. For consistency and where applicable the separation energy is calculated using data from AME 2003 and Coulomb displacement from [1]. A † denotes those values not explicitly stated in the reference but calculated in this dissertation. A § denotes values that were originally reported but altered for comparison using AME2003 and reference [1].

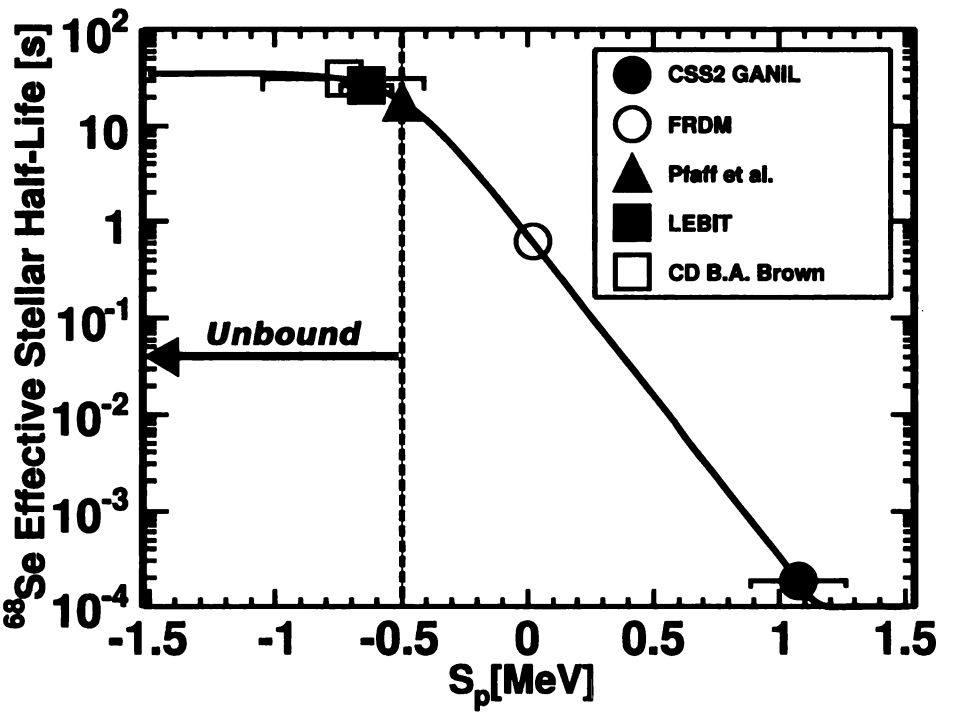

Figure 1.6 – Comparison of the effective ^{68}Se stellar half-life for selected values of the ^{69}Br proton separation energy.

all of the resulting uncertainties in the proton separation energy comes essentially from the uncertainty in the theoretical Coulomb displacement energy calculations.

To illustrate the possible effects on the rp-process the effective half-life of ^{68}Se inside the neutron star crust from Subsection 1.3.1 is shown in Figure 1.6 for a selected set of predicted separation energies. According to these estimates and the uncertainties that exist, even when taking the uncertainties in Coulomb displacement to be correct, it is possible for the effective half-life to vary by a factor of 3. The experiment to directly measure the proton separation energy described in this dissertation attempts to reduce the remaining uncertainties in the ^{69}Br proton separation energy, thereby establishing the validity of ^{68}Se as an rp-process waiting point.

1.5 Dissertation Organization

The remainder of this dissertation is organized as follows. In chapter 2 an overview of the experimental setup and details of technique for measurements of proton unbound nuclei is described. A thorough description of the detectors used in the measurement, including the S800 spectrograph, MCP beam tracking counters, and the HiRA array is also provided. In chapter 3 the analysis of the raw data is described. Key uncertainties of the measurement are discussed as well as the data analysis strategy, data corrections, and detector calibrations. In chapter 4 the physics data and results are discussed. Finally, in chapter 5 a summary of this dissertation is given.

Chapter 2

Experimental Setup

2.1 Overview

The ^{69}Br experiment* was performed at the National Superconducting Cyclotron Laboratory (NSCL) Coupled Cyclotron Facility (CCF) located at Michigan State University in the summer of 2005. This facility is capable of producing a wide array of common radioactive and exotic, or "rare" isotope, beams that would otherwise not exist in nature. A fast in-flight fragmentation technique is employed to produce user requested radioactive beams with the desired energy, purity, and intensity. This will be discussed in more detail in Subsection 2.1.2. An overhead view of the accelerator and experimental areas is shown in Figure 2.1. The beam delivery process begins with an electron cyclotron resonance (ECR) ion source. This device

* proposal advisory committee (PAC) approved experiment number 02023

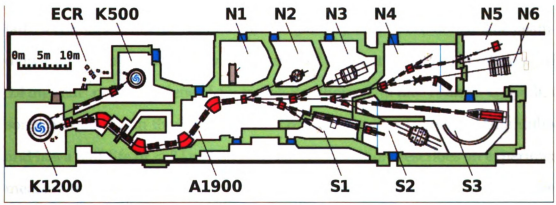

Figure 2.1 – Overhead view of the NSCL Coupled Cyclotron Facility (CCF) as it was configured during the ^{69}Br experiment. The experiment was setup in the S3 vault.

provides beams of stable* positive ions for injection directly into the central region of the K500 cyclotron where they are accelerated to $\sim$ 14 MeV/u. The advantage of the CCF is that the K500 provides the first stage of acceleration. In this mode, ions injected into the K500 are not required to be in a high charge state, resulting in higher output intensities from the ECR source and a higher intensity final primary beam. However, since higher charge states allow for higher final beam energies, the ions extracted from the K500 are injected radially into the K1200 and stripped of their electrons by a carbon foil located inside the first dee electrode [54]. Typically, fully stripped ions are accelerated to an energy of $\sim$ 140 MeV/u in the K1200 and extracted using a high voltage deflector to form a primary beam. The extracted primary beam is directed onto a production target, typically composed of beryllium, located just outside the extraction line. Collisions with target nuclei result in the stochastic production of isotopes via fragmentation. The desired radioactive nuclei are selected from the distribution of produced isotopes using the A1900 projectile fragment separator [55] and delivered via a magnetic switchyard as a "secondary" beam to any of the various experimental areas for study.

For this dissertation a primary beam of ^{78}Kr at 140 MeV/u was used in conjunction with a 775 mg/cm^2 beryllium production target to produce a mixed or "cocktail" secondary beam of ^{71}Br (9.4 %), ^{70}Se (66.7 %), and ^{69}As (23.9 %). The beam was delivered to the S3 vault shown in Figure 2.1 where it underwent collisions with a 5.4 mg/cm^2 polypropylene H_6C_3 target. Reactions with the ^{1}H and ^{12}C result, with some probability, in the formation of ^{69}Br. This nucleus is energetically unbound and has a half-life of $<$ 24 ns [42] [43]. This dissertation describes an experiment to measure the relative energies of the decay products from ^{69}Br$\rightarrow$ p+^{68}Se. The observed relative energies of protons corresponding to decays from the ground state as well as any excited states provide direct information on the relevant two-body

* Stable in this context typically means the lifetime of the atoms are sufficiently long to be a high intensity source. Examples of unstable atoms available as primary beam include ^{48}Ca and ^{238}U.

decay Q-values. Since this is a two-body decay the Q-value for the ground state in addition to the mass of ^{68}Se provides a direct measurement of the ^{69}Br mass. The following sections will describe in more detail the basic technique, the detectors that were used, and their principles of operation.

2.1.1 Experimental Technique

Nuclei at the drip-lines can be extremely difficult to study. By definition they are unbound and therefore can have exceedingly short lifetimes. This feature has two general consequences: First, any kind of direct measurement must be performed immediately after the nucleus is formed. Second, producing a sufficient number of these drip-line isotopes required for an experiment becomes a challenge, especially for higher mass isotopes which generally lie farther from the line of stability. Due to the inaccessibility of these nuclei experiments are typically limited in their resolution and specificity.

For this work the method of decay spectroscopy for reconstructing decay events of unbound nuclei was extended to heavy masses. To measure states in ^{69}Br the outgoing momentum vectors of the proton and ^{68}Se must be completely determined. This requires three main detector systems:

1. The S800 spectrograph.
2. Two MicroChannel Plates (MCP) tracking detectors.
3. HiRA: An array of 16 ΔE-E telescopes composed of silicon strip detectors backed by CsI(Tl) detectors.

A schematic view of the experimental setup and the general measurement technique is shown in Figure 2.2. Protons from the decay of ^{69}Br are detected and identified using HiRA while the heavy, forward focused, ^{68}Se residue is measured in the S800 spectrograph. Both HiRA and the S800 provide information on a parti-

cle's energy and its scattering angle. Two micro-channel plate (MCP) detectors are used for tracking beam particles to the target. Knowledge of the interaction point on target allows one to accurately determine the angle of emission for particles measured in HiRA. In addition, the MCPs provide a time dependent monitor of the beam optics.

Originally, the experiment was planned to produce ^{69}Br by the reaction,

$$^{71}\text{Br} + \text{target} \rightarrow {}^{69}\text{Br} + 2\text{n} \rightarrow {}^{68}\text{Se} + \text{p} \tag{2.1}$$

Specifically, we envisioned a prompt fragmentation of ^{71}Br in the target during which two neutrons are emitted leading to the formation of ^{69}Br. The prompt particles generated in this process, such as the two projectile neutrons, are not detected. This is not important however, because the decay of ^{69}Br is still determined by the complete measurement of the kinematics of the ^{68}Se+p decay products. To our surprise, other production mechanisms are also present. Indeed, the ^{70}Se secondary beam actually provides better results than does the originally planned ^{71}Br secondary beam. Details of the beam composition and its properties will be discussed in Subsection 3.5.5 and the formation process in Section 4.1.

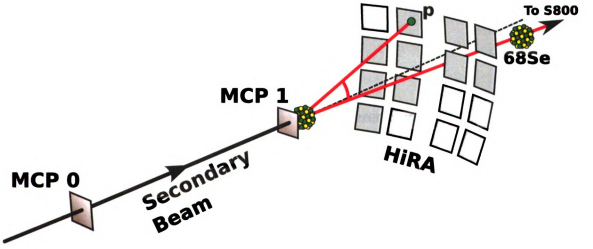

Figure 2.2 – Cartoon of the ^{69}Br breakup reaction.

With the identification and measurement of the particle final states the relative energy can be calculated. For a two-body decay in the center of momentum (COM) frame this is just the total kinetic energy of the decay products and is given by,

$$E_{\text{relative}} = -(m_{\text{p}} + m_{\text{Se}})c^2 + \frac{1}{2}\sqrt{4(m_{\text{p}} + m_{\text{Se}})^2c^4 + 8(m_{\text{Se}}c^2T_{\text{p}} + m_{\text{p}}c^2T_{\text{Se}} + T_{\text{p}}T_{\text{Se}} - \vec{p}_{\text{p}} \cdot \vec{p}_{\text{Se}}c^2)} \quad (2.2)$$

where m_{p}, m_{Se}, T_{p}, T_{Se}, $\vec{p}_{\text{p}}$, and $\vec{p}_{\text{Se}}$ are the masses, kinetic energies, and outgoing momentum vectors of the decay proton and ^{68}Se residue respectively.

Quantum mechanically the proton may only occupy a discrete set of nuclear energy levels. Consequently, in the rest frame of the ^{69}Br nucleus the decay products will emerge with discrete values of the kinetic energy corresponding to those quantum levels due to conservation of energy. At low energies where the level width is narrow and the density of states is low, the spectra of relative energies will exhibit peaks corresponding to these quantum states.

In terms of the astrophysics calculations discussed in chapter 1 knowledge of the ground state Q-value for the ^{68}Se(p, γ)^{69}Br reaction or equivalently the proton ground state separation energy, S_{p}, is needed. The relative energy of the ground state is related to the separation energy by,

$$E_{\text{relative}}(\text{g.s.}) = -S_{\text{p}} \quad (2.3)$$

The Q-value as mentioned in Section 1.3 is the difference in final and initial kinetic energies. In the rest frame of the decay this is just,

$$Q = \Delta T = T_f - 0 = E_{\text{relative}}(\text{g.s.}) = -S_{\text{p}} \quad (2.4)$$

Utilizing Equation 1.9 the mass of ^{69}Br is given by,

$$M(^{69}\mathrm{Br})c^2 = M(^{68}\mathrm{Se})c^2 + M_\mathrm{H}c^2 + Q_\mathrm{p} \tag{2.5}$$

The proton mass is known to an astounding accuracy* of $\pm 1.3 \times 10^{-10}$ u. And, as discussed in Section 1.4 there are a number of measurements of the mass of ^{68}Se with an uncertainty of 5 keV. The uncertainty in $M(^{69}\mathrm{Br})$ is therefore currently dominated by the uncertainty in the Q-value.

This technique therefore provides a measurement of the Q-values for reaction rate calculations as well as the direct measurement of the ^{69}Br mass via the ground state decay Q-value.

2.1.2 Secondary Beam Production

There are a number of methods used to produce usable amounts of rare isotopes for study. These methods include spallation, Isotope Separator On-Line (ISOL) methods, and in-flight fast fragmentation. It is the latter technique that is currently used at NSCL.

At NSCL the heavy primary beam nuclei breakup or are fragmented when they collide with a production target just before the A1900, producing a beam of stable and unstable nuclei with velocities somewhat less than that of the beam [4]. Figure 2.3 shows the position of the production target as well as a layout of the accelerator and the A1900 projectile fragment separator. The production target, frequently composed of beryllium, is usually chosen to maximize the production rate, the acceptance, and minimize the background rate for a particular fragment at the required energy. The separator is constructed of large magnets; 24 superconducting quadrupole and four 45° superconducting dipole. The quadrupole magnets reside in eight cryostat modules, containing three quadrupole elements; sixteen

* The mass is known more accurately in atomic mass units than in MeV/c^2 due to a relatively large error in the conversion.

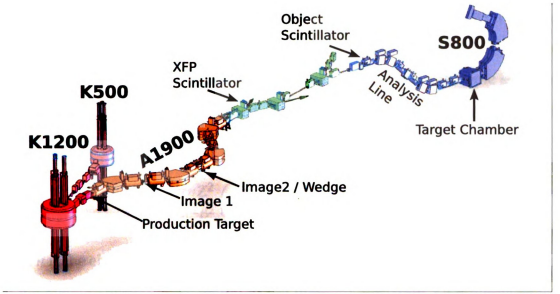

Figure 2.3 – Schematic rendering of the coupled cyclotrons, A1900 fragment separator, and beamline to the S800. HiRA and the MCP tracking system are located inside the target chamber.

out of 24 of the quadrupole triplet elements also contain hextupole and octupole coils [56]. In general, the quadrupoles act as magnetic lens to focus the beam while the dipoles bend the beam to provide an A/Z dispersion described by the equation for the motion of a charged particle in a magnetic field,

$$B\rho = \frac{M}{eZ}\beta\gamma c \approx \frac{A}{Z}\frac{m_u c}{e}\beta\gamma. \tag{2.6}$$

Here, B is the magnitude of the magnetic field, ρ is the bending radius of the dipole, e is the elementary charge, M and Z are the mass and charge number of the particle, and $\beta = v/c$ and $\gamma = (1-\beta^2)^{-1/2}$ are the relativistic factors. The role of the fragment separator is to select out the desired nuclei of interest and filter away the unwanted primary beam and fragments.

Filtering and selection of isotopic fragments is carried out in stages along the separator. The first two dispersive dipole elements select only fragments with a given magnetic rigidity, or $B\rho$. At image 1 and 2 positions, shown in Figure 2.3,

the beam is dispersed and a slit system blocks any fragments not matching the set rigidity. However, this only selects fragments with a certain A/Z ratio. To pick out a fragment with a particular atomic number, and thus obtain isotopic selection, an energy degrading "wedge" is used at image 2 after the slits. Charged particles passing through matter lose energy according to the Bethe formula,

$$-\frac{dE}{dx} = \frac{4\pi n Z^2}{m_e c^2 \beta^2}\left(\frac{e^2}{4\pi\epsilon_0}\right)^2\left[\ln\left(\frac{2m_e c^2\beta^2}{I(1-\beta^2)}\right) - \beta^2\right], \tag{2.7}$$

where n is the electron density, Z is the charge number of the particle, $\beta = v/c$, and I is the average excitation potential of the material. Equation 2.7 governs energy loss in the wedge and also all of the detector systems described in this thesis. For a given velocity of fragments, $dE/dx \sim Z^2$. Fragments then emerge from the wedge with differing momentum, depending on their charge Z; a second dispersive stage then removes more of the unwanted fragments from the beam. The shape and thickness of the wedge are chosen so that the image at the focal plane of the A1900 is achromatic, *i.e.*, independent of the momentum to first order.

Secondary beams produced by the in-flight method are characterized by a number of features. First, the fragmentation process results in fragments with a distribution of momentum and angles. Thus, the emittance, or phase space, of the secondary beam (typically given in units of mm/mrad), produced in the A1900, is relatively large compared to those of stable beams. While the emittance can be improved by cutting the beam with secondary slits, the experimentalist must typically balance momentum acceptance and purity with intensity.

The secondary beam used for this work was produced by the fragmentation of a 140.00 MeV/A $^{78}Kr^{34+}$ primary beam with a beam intensity of $\sim$ 800 enA. A 376 mg/cm^2 Be production target was used in conjunction with a 240 mg/cm^2 Al wedge to achieve a secondary beam intensity of $\sim 2.0 \times 10^6$ pps. Typically, most of

the data was obtained with a momentum acceptance defined by slits (at the image 1 position) of 1 %.

2.2 The S800 Spectrograph

It is a general feature that secondary beams produced by in-flight fragmentation often have large emittances reflecting a trade off between beam intensity and the beam phase space. High resolution experiments can still be done if one can track the incoming and outgoing particles and determine their momentum on an event-by-event basis. The S800 is a large acceptance magnetic spectrometer designed to identify and analyze beam-like reaction products event-by-event. In the following sections, details of the principle operation of the S800 and its various detectors are described.

The S800 system is composed of two sections: an analysis line and the spectrograph, which are shown in Figure 2.4 (the analysis line is composed of the beamline and magnets before the target position). The S800 system is a magnetic optical system with an object plane located at the entrance of the analysis line, an intermediate image plane, and a focal plane at the end of the spectrograph. The analysis line is composed of 4 superconducting magnetic dipoles (shown in blue) and 5 superconducting magnetic quadrupole triplets (shown in green). The S800 spectrograph is composed of a large bore magnetic quadrupole doublet followed by two large magnetic dipoles (D1 and D2). The large acceptances of the S800 in both solid angle and momentum, coupled with a high resolution focal plane detection system [57] allow for particle spectroscopy and identification of nuclear reaction products generated with secondary beams. A reaction target is generally positioned at the pivot point of the S800, which lies in front of the entrance of a large bore quadrupole doublet. In this dissertation the target was placed upstream of this position by 0.68 m. It should be noted that this distance was obtained from the mechanical drawings of the S800 scattering chamber and its location with re-

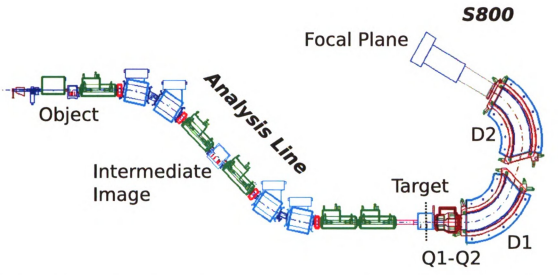

Figure 2.4 – S800 analysis line and spectrograph.

spect to the pivot point. The consequences of this will be discussed in more detail in Section 3.6 and Section 3.5.

2.2.1 Principle of Operation

There are two possible optical modes of operation for the S800 (dispersion matched and focused mode) each with its own advantages and limitations [58, 59]. In dispersion matched mode the beam is tuned to an achromatic focus on the focal plane of the S800 spectrograph. This means that all beam particles that originate from a focused beam spot at the object end up at a focused beam spot in the focal plane. To achieve this the beam must be dispersed in momentum at the target with high momenta particles striking higher on the target. To achieve a dispersion matching, however, this displacement must be 10 cm/% of the momentum difference from the central momentum of the beam. While all beam particles are focused on this beam spot regardless of initial momentum, momenta altering reactions at the target will move the reaction products to a different spot on the focal plane. Assuming an achromatic beam spot at the focal plane of 0.5 cm, this corresponds to

a change in the momentum of less than 0.05 %. Thus, if a reaction at the target changes the momentum by more than 0.05 % it can be resolved from the beam, for example. In principle this allows one to measure reactions with small rigidity differences between the beam and the produced fragment. With the large momentum spreads typical of secondary beams of the CCF, however, the 10 cm/% dispersion of the S800 results in a very large beam spot at the target position. The large beam spot for the dispersive mode makes it a problem for many secondary beam experiments that require large momentum acceptances for the beam to achieve the required beam intensity. In focused mode the image at the target is achromatic. This mode provides a worse ultimate momentum resolution at the focal plane, but the achromatic target spot size allows one to use a wider momentum spread in the beam and thus a large overall beam intensity. For the ^{69}Br experiment the system was configured for focused mode.

A key idea in any beam optics system is that of the central-ray or reference trajectory. This is the path taken by a particle with a rigidity that perfectly matches that of the magnetic system. For the S800 this is the central trajectory taken by the particles that compose the secondary beam that have not undergone any reactions. It is the *deviation* from this central-ray together with the particle identification of the reaction product that contains the information required to reconstruct the reaction that occurred in the target and achieve the required energy and angular resolution. Some of the information about the direction is provided by the focal plane detectors and some is provided by the MCP beam tracking system.

The focal plane box as shown in Figure 2.5 is composed of several detectors that allow for the reconstruction of a particle's momentum vector at the reaction target, measurement of total energy, its particle identification, and a partial measurement of the interaction point on the target. An analytic method is employed to calculate these properties of beam particles at the target from the quantities measured

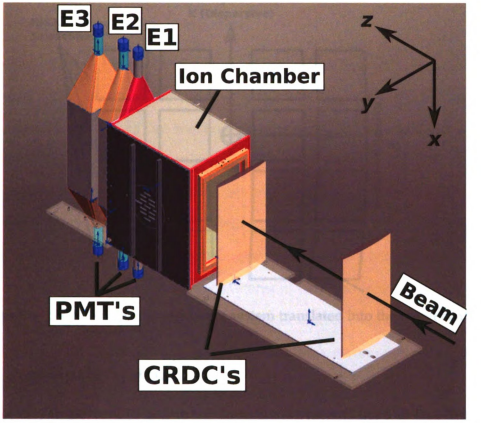

Figure 2.5 – S800 focal plane box.

with the focal plane detectors (see Subsection 2.2.3). Information from two position sensitive cathode readout drift chambers (CRDCs) are used in this reconstruction and measure the trajectory of the particle entering the focal plane (see Subsection 2.2.4). Particle identification is carried out using the ΔE-ToF technique where the energy loss for particles entering the focal plane is measured using a segmented ion chamber (see Subsection 2.2.5). Lastly, the successively thicker scintillators labeled E1, E2, and E3 at the end of the focal plane box provide measurements of energy loss/total energy with E1 also supplying timing and trigger information (see Subsection 2.2.6).

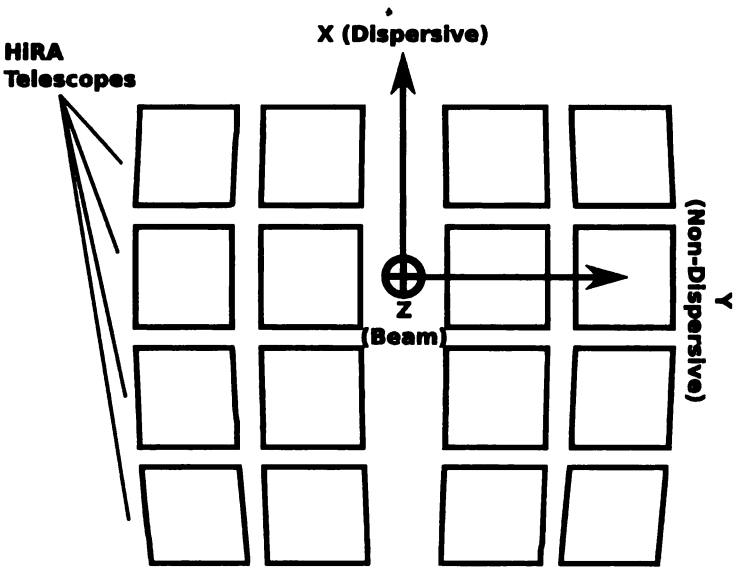

Figure 2.6 – S800 focal plane coordinate system translated into the target chamber.

2.2.2 Coordinate System

It is especially important to define the coordinate systems used in this thesis since three devices, each with their own internal coordinates, are used and must be combined into a unique laboratory frame of reference. The S800 coordinate system is labeled as shown in Figure 2.5. The z-axis points along the direction of the beam with x and y oriented so as to be a right-handed system. The x-axis is vertical (down) and defined to be in the dispersive direction while the y-axis lies in the non-dispersive direction. This is the coordinate system as it would look for someone standing next to the focal plane box at the top of the spectrograph. Standing in the target chamber and looking downstream along the beam axis this coordinate system (after translating it along the beamline down to the target chamber) appears as shown in Figure 2.6. Here, positive x points to beam-up and positive y points to beam-right. This can be a little confusing as one typically expects y to denote a vertical axis and x to denote a horizontal axis. However, this choice of the x-axis as the dispersive axis is standard in beam optics. Vectors in this system are usually defined in terms of dispersive and non-dispersive angles, a and b, respectively.

2.2.3 Inverse Map Reconstruction

An important feature of the S800 is the ability to reconstruct event information at the target using magnetic field maps combined with an analytically calculated transfer map. The details of this method are described in reference [60]. In smaller acceptance spectrometers, correction of higher order field effects and aberrations is often done with additional coils. To achieve high acceptances the S800 accomplishes this through precise magnetic field maps [61] which are used with the ion-optical code COSY Infinity to generate a matrix known as a transfer map. A transfer map expresses a particle's final coordinates at the focal plane detector in terms of its initial coordinates at the target. The transfer map is then inverted and the resulting inverse map expresses the initial coordinates in terms of the final measured coordinates taken from the S800 focal plane.

Following reference [60] the transfer map, denoted as S, can be expressed with the assumption that initial x positions are zero as,

$$\begin{pmatrix} x_f \\ a_f \\ y_f \\ b_f \end{pmatrix} = \mathcal{S} \begin{pmatrix} a_r \\ y_i \\ b_r \\ d_r \end{pmatrix} \tag{2.8}$$

where (x, a) and (y, b) are the dispersive (position,angle) and the non-dispersive (position,angle) as denoted in Subsection 2.2.2 and $d = \delta E/E$ is the relative energy deviation. The subscripts f, i, and r stand for final, initial, and reaction dependent and label the coordinates as depending on their location. Since the reconstruction assumes that $x_i = 0$ any finite X-position along the target folded directly into the final energy resolution of the spectrometer.

To first order this transfer map can be expressed as,

$$\begin{pmatrix} x_f \\ a_f \\ y_f \\ b_f \end{pmatrix} = \begin{pmatrix} 0 & 0 & 0 & s_{03} \\ s_{10} & 0 & 0 & s_{13} \\ 0 & s_{21} & s_{22} & 0 \\ 0 & s_{31} & s_{32} & 0 \end{pmatrix} \begin{pmatrix} a_r \\ y_i \\ b_r \\ d_r \end{pmatrix} \tag{2.9}$$

Although higher order terms can have significant contribution for particular initial coordinates the main dependencies can be understood through Equation 2.9. In words, the dispersive position in the focal plane is proportional to the relative energy deviation at the reaction target. The dispersive angle in the focal plane is proportional to a linear combination of the dispersive angle and relative energy difference. The non-dispersive position in the focal plane is proportional to a linear combination of the initial non-dispersive position and non-dispersive angle at the reaction target. Finally, the non-dispersive angle in the focal plane is also proportional to a different linear combination of the initial non-dispersive position and the non-dispersive angle at the reaction target. Dispersive and non-dispersive coordinates are only mixed in the higher order terms. In will be useful to keep this 1st order relationship in mind when the beam optics are discussed in Section 3.6.

This full transfer map can then be inverted to arbitrary order to give,

$$\begin{pmatrix} a_r \\ y_i \\ b_r \\ d_r \end{pmatrix} = \mathcal{S}^{-1} \begin{pmatrix} x_f \\ a_f \\ y_f \\ b_f \end{pmatrix} \tag{2.10}$$

where $\mathcal{S}^{-1}$ denotes the inverse map. For use with the S800 this map is only calculated to fifth order as this has been determined to be the highest significant order. To summarize, as shown in Equation 2.10 the inverse map relates the measured coordinates in the focal plane (x, a, y, b) to the desired coordinates of the reaction (a, y, b, d).

2.2.4 Cathode Readout Drift Chambers (CRDC)

The two CRDC detectors at the beginning of the focal plane of the S800 provide the XY-position information needed as input for the inverse map reconstruction discussed in Subsection 2.2.3. The CRDCs are shown in Figure 2.5 and are separated by $\sim$ 1.073 m. They each have an active area of 30 cm $\times$ 59 cm. Each detector functions similarly to a single wire drift counter. A mixture of 80 % CF_4 (freon 14) and 20% C_4H_{10} (isobutane) at a pressure of $\sim$ 50 Torr is used as the drift gas.

In the x-z plane (dispersive) the X-position is given by analyzing the distribution of charge induced on electrode pads that run vertically along one side of the detector. There are 224 pads that have a pitch of 2.54 mm. The induced signals on the pads are individually amplified and shaped using front end electronics (FEE) chips developed by the STAR collaboration [62] for their Time Projection Chamber (TPC). Two 16 channel chips are mounted on a FEE card with a total of seven cards needed for readout of each CRDC. The position can be obtained from a Gaussian fit to the pad charge distribution or by finding the center of gravity of the induced charge distribution. In this dissertation the center of gravity method was used exclusively.

In the y-z plane (non-dispersive) the Y-position is derived from the drift time of ionized gas molecules to the anode wire, relative to the trigger generated from the E1 scintillator. Also, to produce a more uniform drift field metallic strips are evaporated onto the surface of the CRDC to create field shaping electrodes. These electrodes produce an electric field that runs perpendicular to the x-z plane (dispersive) of the detector.

Additionally, it is important to note that the gas ions drift in opposite relative directions in each CRDC. This is a consequence of the construction of the focal plane. CRDC 2 is positioned at the front of the ion chamber. As a result, the FEE cards which are mounted vertically to CRDC 2, must protrude into the region be-

tween the CRDCs. On the other hand, CRDC 1 is mounted in the opposite direction with the FEE cards facing inward. This means that for CRDC 1 the ions drift from y-max to y-min while for CRDC 2 they drift from y-min to y-max. The consequences of this will be discussed in Subsection 3.5.3.

2.2.5 Ionization Chamber

The S800 ionization chamber provides a measure of the energy loss (ΔE) of particles that reach the focal plane. When combined with a measurement of a particle's time of flight (ToF) particles can be identified based on their Z and A. The ion chamber is divided into sixteen 1 inch segments that are filled with a $\sim$ 300 Torr of 90 % Ar and 10 % CH_4 (methane), a mixture commonly known as P10 gas. As a particle traverses the chamber it loses energy by ionizing the gas. The gas ions then drift toward the anodes of the chamber and their signals are summed to provide the ΔE signal for the particle identification (PID).

2.2.6 Focal Plane Scintillators

At the end of the focal plane are 3 scintillators that provide timing information as well as a measurement of a particle's energy loss (ΔE) and total energy. As shown in Figure 2.5 the scintillators are labeled E1, E2, and E3. They are relatively large, covering the active area of the CRDCs and have thicknesses of 3 mm, 5 cm, and 10 cm respectively. The light that is produced through scintillation by the traversing particle is collected by photomultiplier tubes (PMTs) located at each end of the scintillator. Both of these PMTs are then used to generate energy and time signals.

The E1 scintillator is particularly important in this dissertation and is the only one used in the analysis since most of the particles of interest are stopped in this scintillator. This scintillator serves as the trigger for the S800 as well as providing a start timing signal for all of the time of flight (ToF) measurements. In addition, the drift time of the gas in the CRDC, which provide the non-dispersive position

information (see Subsection 2.2.4), are taken relative to the E1 trigger. To minimize energy straggling this scintillator also forms the exit window for the ionization chamber.

2.3 Secondary Beam Tracking

To track the beam to the reaction target, we used two detector systems during the experiment. At the intermediate image plane of the analysis line there are two parallel plate avalanche counters (PPACs), which provide information via a transfer map about the beam angle and momentum at the target. In addition, we had two position sensitive MCP detectors in the reaction chamber, which provide information about the position, angle, and arrival time of the beam at the target. Finally, we have tracking information provided by the S800 focal plane discussed in Subsection 2.2.4.

2.3.1 Parallel Plate Avalanche Counters (PPAC)

Two PPACs were installed in the intermediate image box of the S800 analysis line, where they are separated by 0.7 m. Each PPAC contains an entrance foil, center foil, and exit foil. The entrance and exit foils have aluminum strips with a pitch of 1.25 mm evaporated onto their surfaces. At the entrance the strips run in the dispersive direction while the strips at the exit run in the non-dispersive direction. The detector volume is filled with isobutane. Ions produced from traversing charged particles are collected on the strips. The voltage across a resistor chain connecting the strips can then be readout to give x-y position information. With two PPAC detectors angular information is also obtained.

The PPAC detectors were included in the experimental system as a backup to the MCP tracking detectors. After the experiment was performed, we evaluated the performance of the tracking detectors and determined that the PPACs would

not improve the resolution of the experiment, so we do not discuss them further in this dissertation.

2.3.2 Micro-Channel Plate Detectors (MCP)

MCPs evolved from the invention of the single channel electron multiplier [63]. In general, these channels are constructed of a glass tube coated with a semiconducting layer on their interior. The end surfaces of these channels have an electrode plating that allows a bias to be applied across the channel. Secondary radiation such as electrons, X-rays, photons, etc. enter the channel and strike the interior semiconducting surface producing electron multiplication. The performance of such a channel is governed by the ratio of its length and diameter typically denoted as $\alpha = l/d$ [64]. Consequently, one is able to scale down this technology to produce channels with small diameters and short lengths. These channels can be manufactured through a fiber drawing technique and then bundled, cut, and plated to form a MCP wafer. Typical wafers can range in thickness from 0.4-3.0 mm with $\sim$ 10-100 μm diameter channels spaced 5-15 μm apart. Depending on the channel design, gain factors up to 10^9 or more may be reached [63]. This makes such a device a clear choice for applications of single electron counting. Furthermore, these detectors can be tailored for specific applications where properties such as timing [65] are of high importance. When coupled with a stage that can localize the cascade of electrons to specific channels in the plate, position sensitivity is obtained. This concept has been implemented in a number of nuclear physics experiments with heavy ions [66,67,68,69].

In this dissertation two MCP detectors were used for position and timing measurements. The MCP setup was similar to that described in references [68] and [69]. Each detector consisted of a stack of two MCP wafers as shown in Figure 2.7. The MCPs are stacked in a chevron design with each plate cut to produce a bias angle

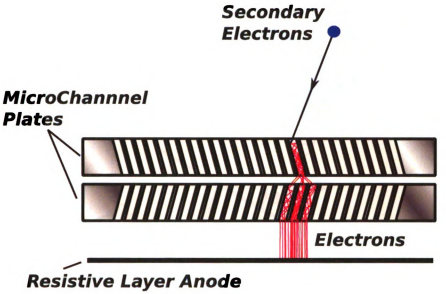

Figure 2.7 – MCP amplification process due to secondary electron emission.

of 8°. Stacking the plates serves two purposes. The first is to increase and saturate the gain of the system due to the multiplicity of firing channels. The second is to reduce positive ion feedback by requiring any ions that are generated at the output of the plate from flowing back toward the input thereby producing after pulses. By forcing the ions to undergo a significant change in direction these effects can be mitigated [64]. Each plate is 0.46 mm thick and contains 10 μm diameter channels with a spacing of 12 μm which make up a total active diameter of 40 mm. The full diameter of each plate is 50.05 mm. A vacuum of $< 5 \times 10^{-6}$ Torr is required for operation of these detectors which required the use of multiple high vacuum pumping stages on our chamber.

A resistive anode layer was employed to obtain position information using resistive readout. As a technical note, the resistive layer is not a square but instead has a "pincushion" shape which reduces the warping effects of the readout. An electrode is connected to each corner of the anode and the charge produced during the electron multiplication process is collected. These signals are sent into a set of fast amplifiers and then digitized with a Caen V792N QDC. Comparing the rela-

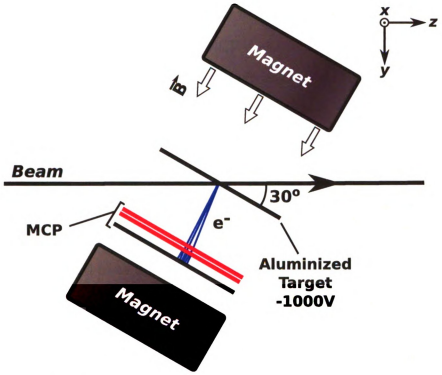

Figure 2.8 – Top down schematic of an MCP beam tracking detector.

tive amplitudes of the digitized corner signals provides XY-position information. Additionally, a timing signal is taken directly from the anode and sent to a TDC. The timing signal was not used in this work.

Position signals for the MCP tracking detector originate from electrons scattered by the beam from a foil that intersects it. The MCP setup is shown in Figure 2.8. A bias voltage of -1000 V is applied to the foil and accelerates the ejected electrons toward the MCP. Two permanent magnets provide a magnetic field that tightly confine the electron trajectories to a helical path. The entire device and target is rotated by 60° with respect to the beam so that the detectors do not block the incoming particles. As a result of this rotation the Y-position (non-dispersive) resolution is improved because the beam is spread over a larger dimension on the foil and on the channels. (For a square beam relative to box resolution of width L the x-dimension of the beam on the foil is L while the y-dimension is $L/\cos(\theta)$). The electrons entering the micro-channel are then multiplied and the resulting charge

is deposited on the anode side behind the MCPs. In a sense the interaction position is projected and imaged onto the MCP detector. One signal from the channel plates can produce a time signal and signals from the four corners of the anode are averaged by charge division to obtain the beam position.

The detector configuration shown in Figure 2.8 will be referred to as a MCP tracking detector. Two MCP tracking detectors are positioned 505 mm apart as shown in Figure 2.2 and thereby track the beam by measuring the trajectory of each particle at two points. The combination of these two MCP tracking detectors will hereby be referred to as the MCP tracking system.

2.3.3 Coordinate System

For this dissertation the common frame of reference is the S800 coordinate system described in Subsection 2.2.2. In this system x labels the dispersive axis while y labels the non-dispersive axis. Trajectories of incoming particles are defined by the same two angles as described in Subsection 2.2.2. The dispersive angle is labeled a while the non-dispersive is labeled b.

2.4 HiRA

The High Resolution Array (HiRA) is a set of 20 ΔE-E telescopes that cover a large solid angle, are highly granular, and are used to identify and analyze charged particles [70] [71]. This dissertation constitutes the first time HiRA, along with our MCP tracking system, was implemented in an experiment. Moreover, for the first time the S800 was coupled with HiRA and our new ASIC readout electronics [72]. Each fully mounted telescope, as shown in Figure 2.9, is composed of a thin Si (65 μm) single-sided strip detector (SSSD), a thick Si (1.5 mm) double-sided strip detector (DSSD), and backed by four 4 cm CsI(Tl) crystals*. The thin SSSD is denoted as "ΔE" while the thick DSSD is denoted as "E". In should be noted that this

* Due to polishing and other processing the actual thickness of the crystals may vary. On average they are closer to 3.9 cm thick.

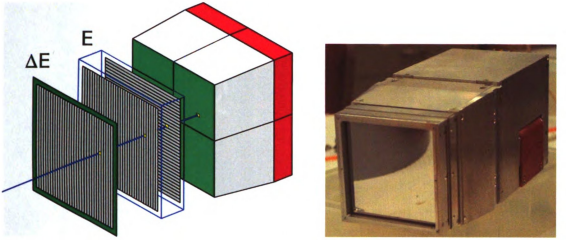

(a) Internal telescope schematic. **(b)** Actual assembled telescope.

Figure 2.9 – A HiRA telescope.

is just a naming convention since particles with a high enough energy will only deposit some of their energy in the E detector and thus function as an energy loss or "ΔE" detector.

For this dissertation 16 HiRA telescopes were configured only with the DSSD and CsI(Tl) in order to detect protons from the decay of ^{69}Br. In the laboratory frame the protons will be traveling with roughly the velocity of the beam or $\sim 0.4c$. All protons of interest will not be stopped by the thick DSSD. The array was arranged as shown in Figure 2.10 with all the detectors positioned at a radius of ~ 50 cm from the target. A thin mylar foil attached to an aluminum frame is placed over the front of the detector cans and serves as a Faraday cage. Four telescopes are stacked vertically to form what will be denoted as a tower and there are four such towers. The towers are labeled from left to right as tower 0, 1, 2, and 3. Each telescope has an unique ID tag that identifies each detector can. More clearly, the position of each telescope and it's ID tag are shown in Figure 2.11.

2.4.1 Silicon Detectors

Semiconductor detectors serve an important role in nuclear physics. In general, they have been available since the early 1960s [73]. They have a number of advan-

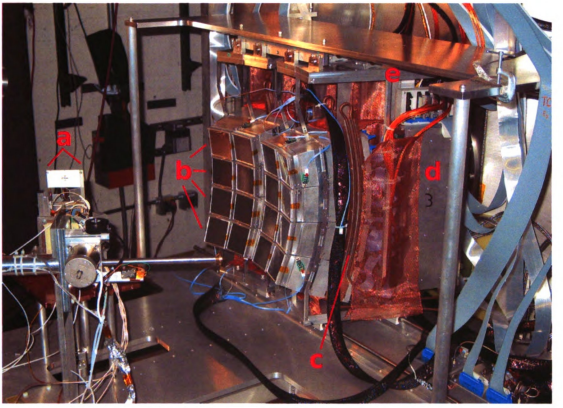

Figure 2.10 – HiRA configuration for experiment 02023. The secondary beam enters from the left of the photo and exits the scattering chamber in the gap between towers 1 and 2. (a) Two targets are viewable in the photo. The upper target is a viewer used for beam tuning. Just below is a Au target used for CsI elastic scattering calibration. (b) HiRA configured with 4 towers of 4 telescopes each. (c) Copper bars and lines used to cool the CsI preamplifiers. (d) Asic electronic box for tower 3. (e) CsI pulser distribution box.

tages including high energy resolution, compact designs, and good timing characteristics. Wafers can be produced with a wide variety of thicknesses in order to have the stopping power required for a given experiment. The High Resolution Array (HiRA) detectors are a good example of such a variety. One of the unique aspects of these Si detectors is their large relative thicknesses. In terms of Si strip detectors the 1.5 mm is very thick and is capable of stopping protons with energies up to 15.534 MeV.

Detectors made of semiconducting material use as information carriers the electron-hole pairs created by particles that traverse the detector. The electronic

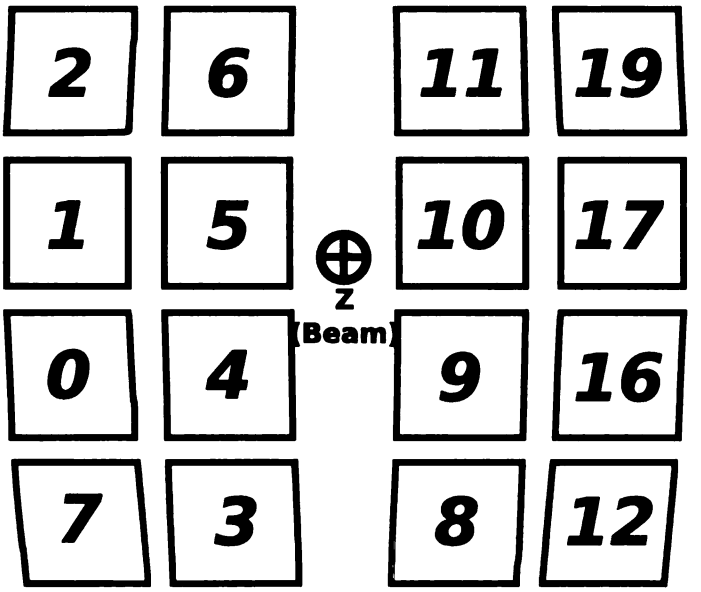

Figure 2.11 – HiRA telescope positions and their ID labels.

structure of a semiconductor can be viewed in terms of energy bands that characterize the allowed and forbidden electron energies. In general, a semiconductor can be understood in terms of a valence band and conduction band. The valence band corresponds to the lowest energy electrons that are bound to specific lattice sites. The conduction band corresponds to a higher set of allowed electron energies in which electrons are free to migrate throughout the lattice. In a semiconductor like silicon the forbidden region, or band gap, between these two bands is small (1.11 eV at $T = 300$ K) compared to an insulator. Particles that pass through such a material excite electrons into the conduction band and leave holes in the valence band. If these electron-hole pairs are collected through the use of an electric field a charge signal is produced that is proportional to the energy deposited by the traversing particle.

For the HiRA Si strip detectors shown in Figure 2.12 the charge carriers are collected and detectors biased via a flexible 32-pin cable. This cable is coupled to the Si through wire bonds that are ultrasonically bonded to both the strip surface

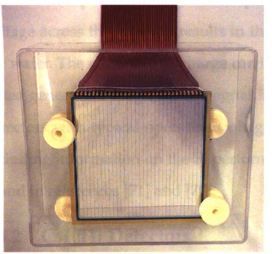

(a) Photograph of an unmounted HiRA ΔE detector.

(b) Photograph of an unmounted HiRA E detector.

Figure 2.12

on the wafer and electrode pads connected to the cable. For the DSSD used in this work both sides are metalized with 3000 Å of aluminum that provides an ohmic electric contact. The wafer itself is epoxied into a custom designed G-10 frame the details of which are described in [71]. When mounted in the telescope can the signal cables run at a 90° angle to a printed circuit board (PCB) at the back plane of the can which maps each of them to a 32-pin output connector.

Characteristics of semiconductors can be precisely controlled and the performance tailored through the use of impurity doping. Impurity doping is generally defined as being n-type or p-type. N-type impurities are sources of excess electrons which are more easily promoted to the conduction band than those electrons associated with the valence band lattice sites. P-type impurities are sources of excess holes. The HiRA Si strip detectors function as a p-n junction. The bulk silicon wafer is n-type material while the strip surfaces on the front (junction side) are p-type which have been created using a p+ ion implantation method. This forms the basis for the junction. Space charge generated at the interface of the p-n junction induces an electric field near the junction known as the depletion region [73]. Here, any

electron-hole pairs that are created quickly migrate apart. Placing a reverse bias voltage across the junction results in the extension of the depletion region across the wafer. The result is that charge carriers migrate rapidly and are efficiently collected generating a high quality signal. The HiRA Si are operated as fully depleted detectors with typical operating voltages of $\sim$ 350 V. More detailed information including information on the Si performance, design, and testing methods can be found in references [71] and [70].

2.4.2 CsI(Tl) Detectors

Protons with energies $\gtrsim$ 15.5 MeV will not be stopped by the HiRA Si detectors. To obtain ΔE-E particle identification the Si are followed by four quadrants of CsI crystals as shown in Figure 2.9a that are capable of stopping protons up to energies of $\sim$ 116 MeV and provide a total E signal.

In general, CsI are classified as inorganic scintillators. Both ^{55}Cs (an alkali) and ^{53}I (a halogen) with their relatively large atomic numbers provide considerable stopping power and together form an alkali halide ionic compound. They rely on the emission of light through the excitation of electron-hole pairs within the band structure of the crystal. Electrons that are promoted to the conduction band can eventually recombine with holes in the valence band through the emission of photons. This process is inefficient, however, and does not typically yield light with usable wavelengths [73]. To enhance the de-excitation process and shift the photon frequencies to a desirable range impurities are added. For HiRA the crystals are doped with thallium (CsI(Tl)). These impurities result in what are known as recombination sites which allow electrons in the conduction band to quickly de-excite through, previously unavailable forbidden, states in the band gap.

Light produced in this way has a characteristic wavelength of 540 nm. Light guides 1.3cm thick couple each HiRA crystal to a Si photodiode which is sensi-

tive to this range of wavelengths and has an active area of $18 \times 18\,mm^2$. Non-uniformities in the light output ultimately limit the final resolution of the crystals and were investigated in reference [74]. The diodes are connected to preamps that are located in the back of end of the telescope can. A 16-pin connector on the back plane of the can connects to a set of high-vacuum coaxial cables. These cables run to a pulser distribution box shown in Figure 2.10e. There is one such box for each tower.

The CsI distribution box serves a couple of purposes. It distributes the common $+12\,V$ preamp power and individual diode biases. In addition, CsI output signals from each box are routed to two 32-pin ribbon cables that run to a flange at the top of the scattering chamber. Finally, an internal pulser circuit which is driven by an external DAC supplies individual test pulses to all the CsI preamps.

Digitizing the CsI signals is accomplished through a more classical set of electronics instead of the application specific integrated circuits (ASICs). Output signals carried out of the distribution box are sent to computer controlled PICO system CAMAC modules which shape and discriminate the pulses. The shaped signals are then digitized by a CEAN V785 peak sensing VME analog-to-digital converter (ADC) module.

2.4.3 Coordinate System

The final coordinates of each HiRA pixel is given in terms of the common S800 coordinate system described in Subsection 2.2.2. Figure 2.6 shows the position of each HiRA telescope and tower in relation to the S800 coordinate system.

2.4.4 ASIC (Application Specific Integrated Circuit) Electronics

Recently there has been a growing demand in nuclear science and in other fields for high density electronics for analog signal processing. As the number of channels that must be digitized grows so does the cost of their associated electron-

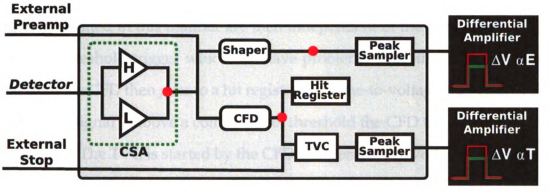

Figure 2.13 – Block diagram of a single channel of the HINP16C ASIC chip.

ics. The highly granular nature of the HiRA Si directly translates into a need for such electronics. If one considers that a fully configured HiRA telescope contains $32 + 2 \times (32) = 96$ channels, and a typical setup contains approximately 20 telescopes, then a total of 1920 channels need to be digitized. In collaboration with Washington University in St. Louis, a set of ASIC chips were developed [72]. Each chip is specifically designed to handle the high capacitance and large dynamic range required for HiRA. This was the first experiment to utilize these new electronics.

Each HINP16C ASIC contains most of the components onboard to process the Si signals. Figure 2.13 shows a schematic drawing of a single channel of the ASIC. An individual chip contains 16 such channels. Signals generated by the detector are first amplified by a charge sensitive amplifier (CSA) that has two computer selectable gains (High and Low). The CSA can also be bypassed and an external preamplifier can be used instead. This mode of operation has been used for HiRA experiments where the ΔE is installed. After amplification the signal is then sent to a shaper and pseudo-constant fraction discriminator (CFD). The shaper takes the long decay-time pulses from the CSA and shapes them into a Gaussian-like signal which has beneficial signal-to-noise ratio (SNR) characteristics. The CFD discrimi-

nates signals that are a constant fraction of the peak height and generates a trigger. Triggers generated in this manner are then independent of the peak height as opposed to a threshold trigger which can have problems with time walk. The logic signal from the CFD then goes to a hit register and time-to-voltage converter (TVC) circuit. If the signal is above a computer set threshold the CFD triggers and the hit register is set. The TVC is started by the CFD and generates a voltage signal which is proportional to the time between the start and an external stop. The resulting two signals from the shaper and CFD circuits are sent to peak sampling circuits which are designed to track and hold the maximum value of the input signal. Finally, both the E and T signals are sent to an off-chip differential amplifier. It generates two analog levels whose difference in height is proportional to either the E or T signals.

Two chips are mounted to a chipboard (CB) and provide the necessary 32 channels to process a single side of the HiRA silicon. A CB is shown Figure 2.14a with a comparison to a quarter for scale. A 32-pin ribbon cable connects the detector to the connector on the left side of the CB in Figure 2.14a. The signals are then processed by the two ASICs and multiplexed off the board. The CBs connect to a mainboard as shown in Figure 2.14b through the 64-pin high density connector located on the top of the board in Figure 2.14a. In the center of the mainboard is a field-programable gate array (FPGA). One key advantage of the ASIC is that the analog E and T signals along with address information referring to the chip and channel that generated the signal can be multiplexed out of the system on only three cables. Otherwise, every channel would have its own signal cable and be routed into its own digitizer. With the ASICs, each mainboard multiplexes all E and T signals onto only two double (differential) lemo cables. Addressing information is carried out simultaneously on a 64-pin high density ribbon cable.

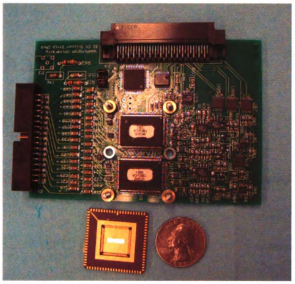

(a) Photograph of the HINP16C ASIC chipboard. The quarter is shown for scale. Also shown in the bottom left is a 8 channel prototype.

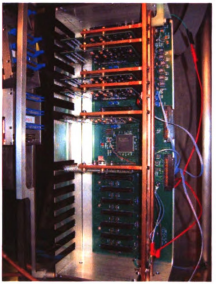

(b) Photograph of an ASIC mainboard configured with 6 chipboards.

Figure 2.14 – HiRA ASIC electronics setup.

The signals for E and T are sent into pipeline or "flash" ADC to be digitized while the addresses are sent to an universal logic module (XLM). Another FPGA onboard the XLM controls I/O flow, logic, and clocks in the streaming data. For this dissertation 1024 channels need to be digitized. Using the electronic setup just described only one SiS flash ADC and two XLMs were used. This greatly reduces the number of cables needed, freeing up space, and reducing the number and complexity of flanges in the setup.

Chapter 3

Data Analysis

> Ahhh, what an awful dream. Ones and zeroes everywhere... and, I thought I saw a two.
>
> BENDER

In general, data produced and recorded during an experiment must undergo further detailed and rigorous analysis. Experiments in nuclear physics rely on the electrical signals generated by sensitive detectors which are digitized and acquired through an electronic data acquisition (DAQ) system. Typically, raw data collected during a running experiment is encoded and written to a computer file for future processing. For complex experiments with many detector channels the data files can be very large, making them difficult to efficiently manipulate and search. Transforming the basic raw information into a manageable and physically meaningful data set is one of the main goals in the data analysis process.

The data analyzed in this dissertation is generated by detectors in three main systems that all must be calibrated and their performance understood in order to properly process the basic signals into a form from which the physics of interest may be extracted. The processing, calibration, correction, and analysis of data collected during the experiment (see chapter 2), including obtaining spectral information for ^{69}Br proton emission, is the subject of this chapter.

3.1 Monte Carlo Methods

To probe the sensitivities to various experimental and theoretical uncertainties a Monte Carlo code was developed to simulate the setup and ^{69}Br proton decay. The code was written in C++ and takes advantage of the class libraries available in the ROOT* analysis framework. It is designed to simulate the two-body decay of a nucleus for selected Q-values and then propagate the decay products into the user defined HiRA detector geometry. A user sets the input values of the simulation and runs an event generator. The code produces as output a ROOT file containing a TTree object which holds all the data of the simulation on an event-by-event basis as well as any histograms generated during the simulation.

A significant number of effects are taken into account in the simulation. These include,

1. **Realistic beam properties:** An incoming simulated beam can be defined by its coordinates at the target. It may be point-like, rectangular, or elliptical in terms of the beam spot at the target plane. The most realistic beam in the simulation is defined within a 4-dimensional beam phase space ellipsoid. These are typical coordinates used in the beam transport community. The coordinates are (x, a, y, b) and represent the dispersive position, dispersive angle, non-dispersive position, and non-dispersive angle respectively.

2. **Detector geometry:** An input file defines the positions of HiRA pixels relative to the target plane.

3. **Detector resolution:** Actual detector resolutions can be defined for the individual HiRA detector elements. For the S800 the resolutions are defined in terms of energy, momentum, and angular resolutions. For the MCPs the XY-position resolutions are also defined and accounted for in the simulation.

* root.cern.ch/

4. **Finite HiRA pixel size:** Finite surface areas and angles of the HiRA pixels are taken into account.

5. **Bad HiRA detector elements:** The simulation allows for cuts to be applied that tag data associated with malfunctioning detector elements.

6. **MCP position corrections:** Uncorrected and corrected data based on the interaction position on target is outputted during the simulation for later analysis and comparison.

7. **Single particle lifetimes:** Since the lifetime of a state and its width are related by $\tau \propto 1/\Gamma$, narrow states with lifetimes $\tau \gtrsim 10^{-11}$ s can decay between the target and HiRA detectors (instead of at the target location). This will be the discussion of Section 4.3. Consequently, peaks in the the relative energy can have tails at lower relative energies and must be properly taken into account for a correct interpretation.

Data generated from the developed Monte Carlo code will be used in a number of the following sections. In Section 4.3 it is used to illustrate how the finite lifetime of a state can influence the interpretation of the relative energy. In Section 4.5 simulated data is used in a fitting method to determine the proton separation energy, S_p, of ^{69}Br.

3.2 Data Reduction Techniques

A key aspect of data analysis in nuclear and particle physics is the reduction of raw data to a form that is easier to process and manipulate. For this dissertation a number of software libraries for data processing were created using the ROOT analysis framework. All the detector components are described by C++ classes. The classes contain structures for holding data as well as functions for basic processing.

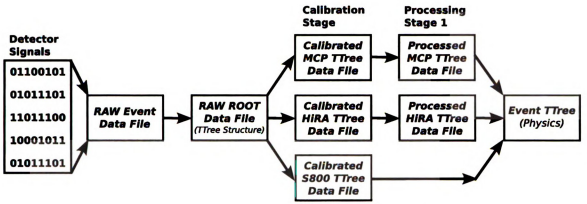

Figure 3.1 – Block diagram for the general data reduction procedure.

Data processing is conducted in stages. A basic schematic is shown in Figure 3.1. First, the raw event data files are unpacked and converted into raw ROOT event files. Next, calibration parameters are determined, defined, and then applied to produce a new set of calibrated ROOT event files for each device in the experiment. An additional processing stage for HiRA and the MCPs is applied which is useful for more advanced analysis of the data. Finally, a "physics event class" is used to recombine the data into a single file containing the physical quantities of interest in the experiment. Partial contents of the data produced with the physics event class include,

1. **Event-by-event PID:** Each event is characterized by the initial and final particles involved in the reaction. The incoming beam particles and detected outgoing reaction products are identified on an event-by-event basis.

2. **Measured particle properties:** The final corrected energies, angles, and etc. are generated and stored event-by-event.

3. **Transformation to a common frame of reference.**

4. **Calculated relative energy.**

Data presented in this dissertation is generated from $\sim$ 20 Gb of raw data spread over 50 files. At the end of the processing sequence a single file of $\sim$ 1 Gb is left con-

taining all the interesting physics information. The advantage here is that looping over and searching through this compact file as well as the modularization of data processing is considerably more efficient. There also exists the possibility of modifying the code for future experiments as well as adding additional modularized processing stages before the creation of the physics event tree.

3.3 HiRA Calibration and Analysis

Decay protons, as well as other light charged particles, are detected and identified with HiRA telescopes. An accurate and precise measurement of the total kinetic energy of each particle requires both the DSSD and CsI(Tl) to be properly calibrated. The calibration has three main parts: A pulser calibration that tests the linearity and determines the energy offset of the CsI(Tl) and DSSD electronics is discussed in Subsection 3.3.1, the energy calibration of the DSSD with α-source data is discussed in Subsection 3.3.2, and the CsI(Tl) energy calibration from elastic scattering of light nuclei is discussed in Subsection 3.3.4. In Subsection 3.3.5 the calibrated particle identification (PID) obtained with HiRA is discussed.Finally, the geometric efficiency of HiRA and its consequences are described in Subsection 3.3.6.

3.3.1 Pulser Calibrations

The linearity of the CsI electronics, specifically the amplifier and the ADC, was verified with the pulser system described in Subsection 2.4.2. A single pulser drives a pulser circuit in the distribution boxes connected to the test input of the CsI(Tl) preamps. A ramp is done over the full ADC range as shown for a single crystal in Figure 3.2. The resulting linear fit is shown in Figure 3.3 where the pulser amplitude has been converted to the equivalent input signal that would be produced as light output of the crystal. Since the combination of amplifier and ADC module begins to show known non-linearities above channel 3500 the fitting is restricted to this range. All CsI(Tl) channels were pulsed in the same manner and all dis-

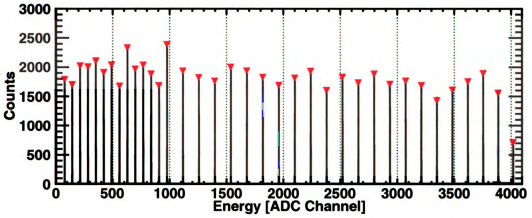

Figure 3.2 – Telescope 5 CsI 0 pulser ramp.

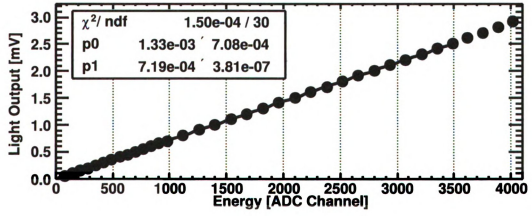

Figure 3.3 – Linear Fit of the telescope 5 CsI 0 pulser ramp.

play similar linearities to that shown in Figure 3.3. However, the x-offset from the pulser data did not provide a correct measure of the true channel corresponding to zero energy. Instead the offset is extracted from an extrapolation of low energy CsI(Tl) events as described in Subsection 3.3.4.

A similar pulser ramp was done for the HiRA DSSD using a precision BNC PB-5 pulser. All channels were tested and found not to have any significant non-linearities. Additionally, the pulser ramp was to be used to determine the energy offset of the DSSD calibration that will be discussed in Subsection 3.3.2. However, the pulser led to inconsistent results for the energy offset as compared to that of the α-source calibration. Therefore, we chose to use the energy offset obtained from the α-source calibration.

3.3.2 α-Source Calibrations

The HiRA DSSD energy calibration is carried out using a ^{228}Th source. In the decay chain of ^{228}Th there are five main α-lines that are separated by at least 200 keV, making this an ideal calibration source. In addition, there is an α-decay from ^{212}Po$\rightarrow$^{208}Pb with an energy of 8.784 86 MeV that provides a higher energy point not available in other common sources. For this dissertation $\sim$ 51 hours of α-source data were taken. Most of this data was recorded during the actual experiment with the source placed in the upper corner of the scattering chamber. However, this was not an optimum setup as a small number of strips were not illuminated and instead these runs were used mostly for tracking the stability of the calibration. The final calibration was performed at the beginning and at the end of the experiment with the source placed at the target location so as to expose all strips to the source.

A number of factors regarding sources of energy loss are taken into account for the calibration. The ^{228}Th source has an activity of $\sim$ 1.2 μC and is sealed with

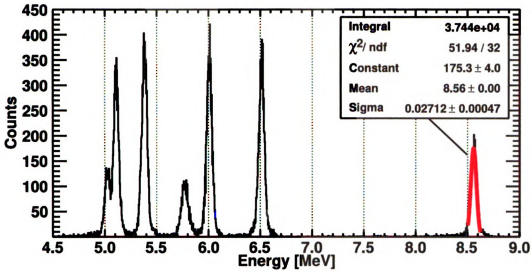

Figure 3.4 – Telescope 9 ^{228}Th α-source calibration for all front strips of the DSSD.

a thin Au (gold) window that is 50 $\mu g/cm^2$ thick. Thin 1.9 μm thick aluminized mylar foils cover the entrance of each HiRA telescope and present an additional source of energy loss. Finally, a thin layer at the surface of the DSSD, known as the dead layer, is not an active part of the detector volume. This was estimated to have a thickness of $\sim$ 0.6 μm from previous tests. The total energy loss through all of these layer for each α energy is calculated with the fragment separator and spectrometer simulation code LISE++*. Stopping powers in LISE++ were set to be consistent with those listed in [75].

The resulting calibration of telescope 9 for all front strips of the DSSD is shown in Figure 3.4. Similar calibration spectra were obtained for all other telescopes. Table 3.1 lists the resolution of the 8.784 86 MeV peak for all combined front strips for each telescope. It is clear from the table that a reasonable energy resolution was obtained over the entire array with an average energy resolution of 77.0 keV FWHM.

* www.nscl.msu.edu/lise

Telescope ID	Sigma [keV]	FWHM [keV]
0	27.9	65.7
1	29.1	68.5
2	42.9	101.0
3	27.7	65.2
4	41.3	97.3
5	31.6	74.4
6	31.4	73.9
7	26.5	62.4
8	29.7	69.9
9	29.8	70.2
10	34.1	80.3
11	30.0	70.6
12	33.5	78.9
16	35.7	84.1
17	35.1	82.7
19	36.6	86.2

Table 3.1 – Resolutions for the 8.784 86 MeV α-source peak for front strips for each telescope.

3.3.3 ASIC Readout Order Correction

This dissertation constituted the first experiment in which the newly designed HiRA ASIC electronics were implemented. It was quickly realized that there were a number of issues regarding the ASICs, chipboards (CBs), and mainboard that needed to be debugged. The most prominent issue for this analysis involved the influence of the channel readout sequence on the amplitude of the energy signal. This will be referred to as the ***readout order problem***.

When an event triggers the ASIC system the electronic channels are readout and digitized according to a specific sequence. First, during the readout process each mainboard is processed independently. There are two modes of readout; sparse mode (only channels that triggered the discriminator are readout) or forced mode (all channels are readout). For this dissertation sparse readout mode is utilized. Second, CB slots, as shown in Figure 2.14b, are processed from the bottom to the

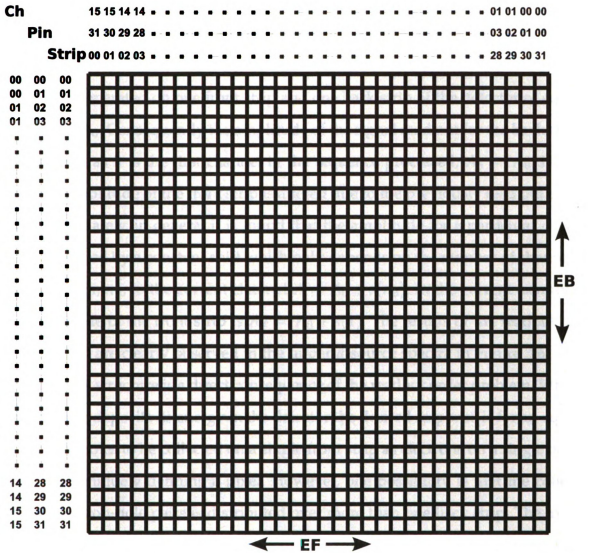

Figure 3.5 – Diagram of the chip/channel/strip mapping for the HiRA DSSD.

top slot. This is significant, since each telescope in this experiment requires two CBs, one for the back side and one for the front side of the DSSD. The CB for the back is always in a lower slot than the front (since the DSSD output connector for the back is below the front connector on the rear of the telescope can) and so will always be processed first. Third, each CB contains two ASIC chips, labeled 0 (even strips) and 1 (odd strips) as shown in Figure 3.5. During the readout process chip 0 (even strips) is processed first followed by chip 1 (odd strips).

During the initial data recording it was found that for a given channel the number and sequence of channels read previous to that channel affected the value of its energy. For example, let's suppose that a particle passes through the DSSD and a signal is generated on one front strip and one back strip of the detector of equal amplitude A_0. Consequently the amplitude of the signal read out for the back strip is unaltered as it is the first channel in the sequence processed, $A_b = A_0$. However, the amplitude of the front strip is altered due to the previously read out back strip. Fortunately, in general it is found that the amplitude for a particular channel is modified by a constant shift which only depends on the number of channels readout prior, n_p, to the current channel $A = A_0 + s(n_p)$. In the current example, the amplitude of the front strip is $A_f = A_0 + s(1)$. The results of the readout order problem are clearly observed in the upper α-source spectra in Figure 3.6. The double-peak structure is a direct consequence of the readout order problem. When an α particle deposits its energy in the detector the desired response is for an equal number of holes to be collected on a single front strip as electrons on a single back strip thus uniquely defining a pixel. However, one possibility is that the collection of electron-hole pairs is distributed over more than one back strip. The most probable situation after a two strip event (one front and one back) is a three strip event where one front strip fires along with two back strips. Since the back strips are processed first there are now two channels read out prior to the front strip as opposed to just one. This results in a shift in the amplitude of the energy signal from the front strip and is observed as a shadow peak at higher energies in the upper spectra in Figure 3.6.

For this dissertation the key events of interest are only those where a single proton from the decay of ^{69}Br is detected in HiRA. As this is ultimately a low statistics experiment, as many of these events as possible need to be corrected. Shown in Figure 3.7 are the number of channels being readout from tower 1 for

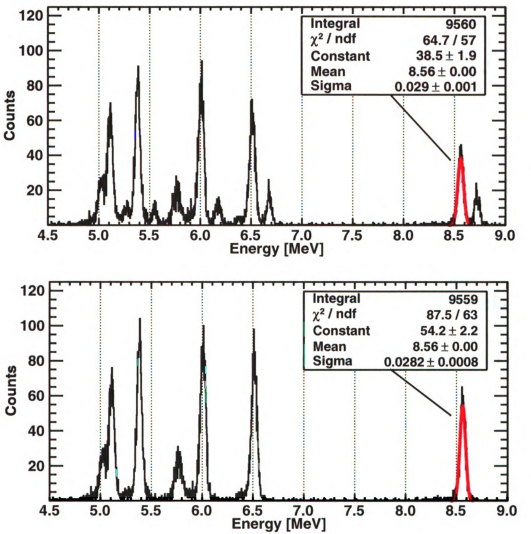

Figure 3.6 – ASIC readout order correction of the α-source calibration for Telescope 5. The upper figure is the α-source spectrum for the front strips before the correction while the lower figure is the spectrum after the correction.

a subset of the experimental data gated on protons. One channel events are of no interest as they do not provide any pixel information and are ignored. Two channel events compose most, 57.0 %, of the data in a tower and correspond mostly to one front and one back strip firing. Three channel events compose 4.7 % of the data in a tower and correspond to one front and two back strips firing. Four channel events compose 20.6 % of the data in a tower and correspond to mostly two proton events in the same tower as well as four strip firing events. Events with more than four

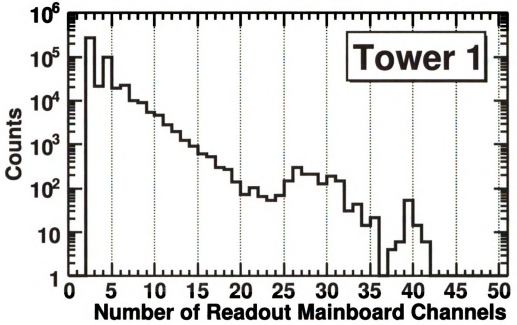

Figure 3.7 – Distribution of channels per event that are readout from HiRA Tower 1. Events where 2, 3, or 4 strips are readout compose most, but not all, of the data. Events with less than 2 channels are suppressed in the plot.

readout channels in a tower make up the remaining 17.7 % of the data in a tower and correspond to multi-particle and noise events and are not of interest in this analysis.

To correct the readout order problem the α-source calibration data was used to obtain the shifts, $s(n_p)$ just described. The peak position of the 8.784 86 MeV α for two channel events is compared to the peak position of three channel events. Shifts are obtained for each chip since the shifts do not depend significantly on individual channels for this dissertation. Four channel events and higher could not be corrected since the α events did not provide enough statistics for this type of event to make a correction. The lower spectra in Figure 3.6 shows the result of the correction as applied to the α-source data for telescope 5. The resolution of the 8.784 86 MeV peak remains practically unchanged after the calibration at $\sigma \sim 29$ keV. For this dissertation, the final analysis only contains data where a single proton is detected and where either two or three DSSD strips are triggered.

3.3.4 Light Nuclei Elastic Scattering

By definition, the total kinetic energy of elastically scattered particles is conserved. Only a change in the particle trajectories and in the sharing of this energy between scattered particles results. As long as one scatters from target nuclei that are much more massive than the projectile, any recoil of the target nuclei becomes negligible and the incoming and outgoing kinetic energies of the lighter projectile are nearly equal. For a stationary heavy target in the laboratory the kinetic energy of a light elastically scattered projectile nucleus varies only slightly as a function of its laboratory scattering angle. This makes elastic scattering a useful method of calibration since the projectile nuclei can be scattered into the range of angles where detectors are located. So long as one knows the identity of the scattered particle and its incoming energy, the precisely defined elastic scattering energy provide points of calibration.

For this dissertation the energy calibrations of the CsI(Tl) detectors were done via elastic scattering of light nuclei on a 19.5 $\mu g/cm^2$ gold (^{197}Au) target. The Au target was mounted perpendicular to the beam direction as opposed to the 60° rotation of the MCP/reaction target. A special frame, just visible in Figure 2.10 (a), held the Au target to the ladder. The A1900 fragment separator was tuned to a $B\rho = 1.371\,60\,Tm^*$ to allow the passage of p, d, t, ^{3}He, and ^{4}He nuclei produced in the fragmentation of the primary ^{78}Kr beam. Slits inserted at image 1 and image 2, shown in Figure 2.3, reduced the momentum acceptance of the secondary beam to $\sim$ 0.4 % thereby providing nuclei with sharply defined kinetic energies. Using Equation 2.6 and the given A1900 $B\rho$ the kinetic energies for each isotope in the secondary beam are calculated and listed in Table 3.2. The PPACs, extended focal plane (XFP) scintillator, object plane (OBJ) scintillator, and MCP 0 target foil were removed during the calibration to reduce the energy straggling of the beams.

* The units of magnetic rigidity are given in Tesla-meters.

Isotope	Kinetic Energy [MeV/u]
^{1}H	85.4363
^{2}H	22.1106
^{3}H	9.92435
^{3}He	39.0892
^{4}He	22.391

Table 3.2 – Elastically scattered nuclei used in the CsI(Tl) energy calibration and their kinetic energies.

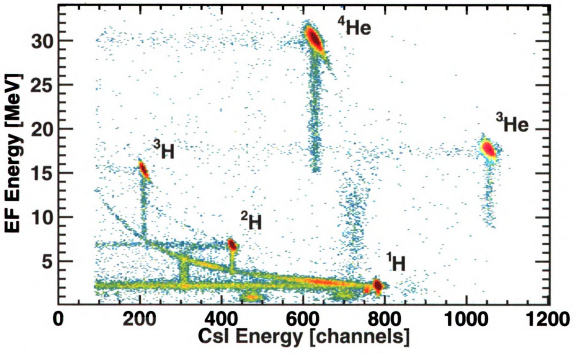

Figure 3.8 – Light nuclei elastic scattering peaks for uncalibrated telescope 5 CsI 3.

Elastic scattering peaks can be easily identified in either a 1D CsI(Tl) energy spectrum or, since HiRA is a ΔE-E telescope, in a 2D PID spectrum. An example of the 2D spectrum for elastically scattered particles into telescope 5 is shown in Figure 3.8. All other working detectors show similar peaks.

While the energy of the elastically scattered light nuclei is given by the $B\rho$ of the A1900 there are energy losses that must be accounted for in order to determine

the energy the particle actually deposited into the CsI(Tl). Energy loss corrections are made for,

1. The angle dependent energy loss in the target.
2. Energy losses in the aluminized mylar cover on the front of each HiRA telescope.
3. Energy losses in the dead layer of the DSSDs.
4. Energy losses in the individual DSSD detector thicknesses.
5. Energy losses in the mylar wrapping of the CsI(Tl) crystal segments.

The actual energy of the elastic scattering peak is given by these energy losses subtracted from the energy determined from the $B\rho$. All of the energy losses just listed were taken from tables generated with LISE++.

While most of the energy losses and material thicknesses are known, the actual DSSD thickness can be uncertain by a few percent. Fabricating silicon wafers with a thickness of 1.5 mm and of the quality required for use as a HiRA detector is difficult. Additionally, it is a challenge to accurately determine the actual thickness of each silicon wafer. For this dissertation, the actual thickness of each detector is inferred from the energy loss of the elastically scattered deuteron which loses ~ 7 MeV of energy in the DSSD. For a thin absorber the energy loss, ΔE, is related to the thickness, t, of the absorber by,

$$\Delta E = -\left(\frac{dE}{dx}\right)_{\text{avg}} t \tag{3.1}$$

where $-(dE/dx)_{\text{avg}}$ is the linear stopping power given in Equation 2.7 averaged over the particle's energy while in the absorber. Values of linear stopping power are abundantly tabulated for many different particles and commonly used mate-

Telescope	Manufacturer Thickness (μm)	Inferred Thickness (μm)	Δ (μm)
0	1496	1442.09	53.91
1	1503	1452.71	50.29
2	1490	1453.91	36.10
3	1488	1411.99	76.01
4	1489	1444.93	44.07
5	1499	1447.25	51.75
6	1471	1435.47	35.53
7	1499	1442.38	56.62
8	1460	1420.80	39.20
9	1491	1454.68	36.33
10	1511	1462.66	48.34
11	1491	1457.57	33.44
12	1452	1410.90	41.11
16	1513	1475.43	37.57
17	1496	1333.35	162.65
19	1541	1512.16	28.84

Table 3.3 – Si detector manufacturer thicknesses and their inferred thicknesses from deuteron elastic scattering.

rials. A thick absorber, such as the DSSD, can be viewed as a series of thin absorbers and Equation 3.1 can be calculated recursively until a desired value of ΔE is reached thus yielding the thickness of the absorber. LISE++ which implements a method similar to that just described is used to calculate the DSSD thickness given the energy loss of the deuteron for each detector. The inferred detector thicknesses from this method are listed in Table 3.3. These are the values used in all calculations in this analysis. With the exception of telescope 17, the values agree to better than 4% of that given by the manufacturer. It should also be noted that the deuteron energy loss is in a relatively well calibrated region of the DSSD detector, since the energies of the α-source calibration cover this range, and provide an accurate indirect measure of the detector thickness.

It was found after the experiment that the pulser system did not function as expected. The pulser system is driven by a voltage level set by a digital-to-analog

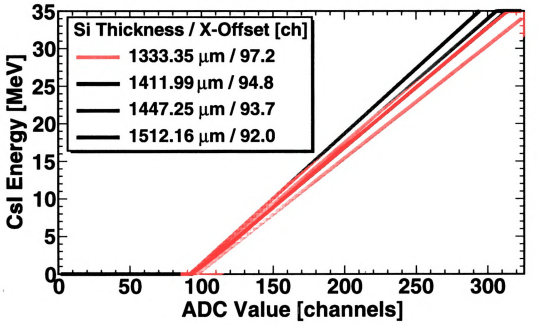

Figure 3.9 – CsI(Tl) x-offset dependence on Si thickness.

converter (DAC). However, the grounding of the electronic racks and the detector systems inside the scattering chamber was not optimal and it is suspected that this resulted in an offset shift for the pulser signals. Since we are unable to determine the zero energy offset from the pulser ramp discussed in Subsection 3.3.1, the zero energy offset is instead found by extrapolating from the energy loss in the DSSD, a process which will be discussed in the following paragraphs. Therefore it is important to understand how changes in thickness may effect the zero offset. The effects of adjusted silicon thicknesses on the zero energy offset of the calibration are shown in Figure 3.9. While conclusions about the gain is sensitive to changes in thickness the offset is not.

The response of the CsI(Tl) depends somewhat on the isotope and therefore, each isotope requires its own calibration. For this dissertation we are concerned with properly calibrating the response of the CsI(Tl) for protons. Consequently, the elastic scatting peak provides the only necessary point for the calibration. Ad-

dit

DS

A

ste

(S

wh

du

his

his

co

ure

to

imp

* Fo

tion

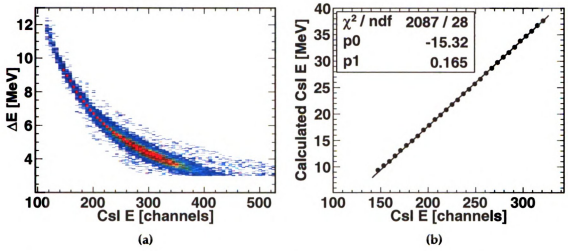

Figure 3.10 – Calibration points taken from ΔE. (a) The proton PID band used to obtain calibration points. The profile histogram is overlaid on the rebinned histogram. (b) Linear fit relating the calculated CsI(Tl) energy as a function of the CsI(Tl) ADC channel.

ditional lower CsI(Tl) energy points are obtained based on the energy loss in the DSSD. These energy loss points are then used to extract the zero energy offset. A systematic method is used to extract these points and consists of three main steps. First, histograms of ΔE-E were constructed with a fine binning of the y-axis (Si ΔE) and a coarse binning of the x-axis (CsI E). Second, a profile histogram*, which displays the mean value of one axis for each bin in the other axis, was produced, and an example is shown in Figure 3.10a where the red points of the profile histogram are overlaid with the proton PID band. Finally, points from the profile histogram are selected over a range of ΔE energies (from $\sim$ 4 MeV-9 MeV) and a corresponding CsI(Tl) energy calculated using data generated from LISE++. Figure 3.10b shows the resulting calibration that maps the raw CsI(Tl) ADC channels to a CsI(Tl) energy calculated via the energy loss in the DSSD. This method was implemented for all detectors by interpolating energy loss tables generated with

* For a more detailed description of this histogram object consult ROOT online class documentation under TProfile. `http://root.cern.ch/root/html/TProfile.html`

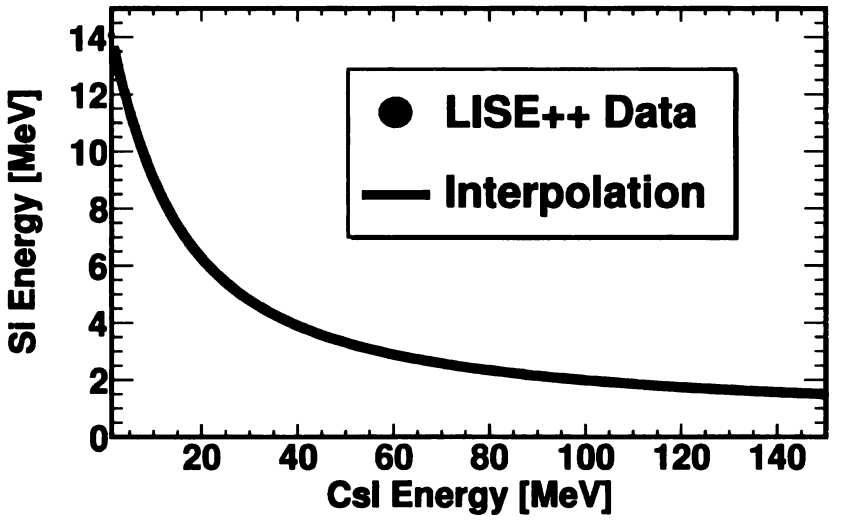

Figure 3.11 – Natural 3rd-order cubic spline interpolation of LISE++ calculation. This provides an accurate conversion from energy loss in the DSSD to calculated energy in the CsI(Tl).

LISE++. Natural 3rd-order cubic splines were created for each combination of detector angle, energy losses, and elastic scattering energy. For a given incoming particle energy and angle, in steps of 250 keV, the energy loss in each detector layer was calculated* and accounted for in the calibration. The interpolations, such as those shown in Figure 3.11, were used to translate the DSSD ΔE energies into a corresponding CsI energy as shown in Figure 3.10b for each detector.

The proton elastic scattering point and the points obtained from the energy loss in the DSSD are enough to constrain the CsI(Tl) energy calibration. However, these points do not lie on a single line. This could be a consequence of not having the correct detector thickness. For this dissertation, the decay protons of interest lie in the lower ΔE region of the PID band and therefore deposit most of their energy in the CsI(Tl). Furthermore the decay protons will have an energy approximately that of the beam, or $\sim$ 72 MeV. It is therefore important to properly calibrate in the energy range around the beam energy. The proton elastic scattering point is within this region and is used as a fixed point to constrain the calibration. It is, however,

* The [H-base] J.F. Ziegler energy loss and the ATIMA 1.2 (LS-theory) options were used for the calculations.

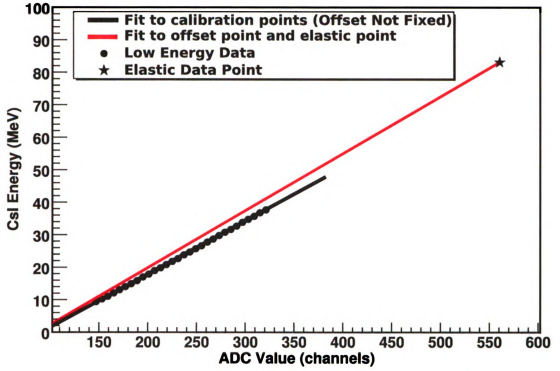

Figure 3.12 – Telescope 5 CsI 2 calibration. Two points are used in the fit; the proton elastic scattering point and an zero energy x-offset point determined from a linear fit of the DSSD energy loss points.

sensitive to the $B\rho$ calibration of the A1900 fragment separator. This complication is discussed in Subsection 3.7.2. A second point is still required as we found that the CsI(Tl) pulser system produced unreliable zero offset information due to its sensitivity to the DC level difference between the towers and the electronic racks. Proton calibrations of CsI(Tl) detectors are known to be linear. A linear fit of the DSSD ΔE points is used to obtain the zero energy offset and is used as the second point. Figure 3.9 shows how this derived offset is largely independent of the assumed detector thickness. Thus the ΔE points fix the energy offset and the elastic scattering point fixes the gain as shown in Figure 3.12 This procedure is repeated for all HiRA CsI(Tl) crystals and is of sufficient accuracy for the calculations in this dissertation.

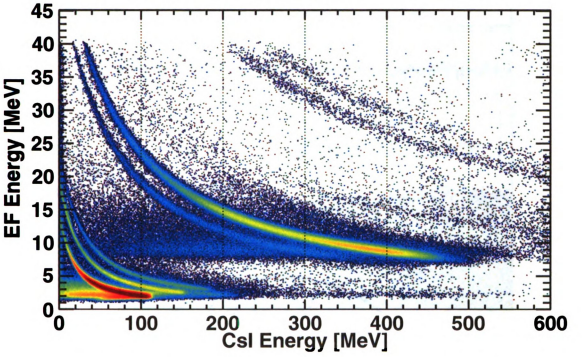

Figure 3.13 – Spectra showing cleanly resolvable HiRA PID bands for p, d, t, ^{3}He, and ^{4}He.

3.3.5 Particle Identification Results and Discussion

With both the DSSD and the CsI(Tl) calibrated we obtain PID spectra as shown in Figure 3.13. Light charged particles up to ^{4}He are cleanly resolved. However, there are a number of conditions put on the data. First, the middle strips of the DSSD are always excluded. This is done because they overlap with the gaps between CsI(Tl) crystals as shown in the schematic in Figure 2.9a. Particles entering this region can deposit energy in more than one crystal making these events difficult to properly analyze. Second, (as mentioned in Subsection 3.3.3) only events where two or three strips are involved are analyzed. Third, even though the energy is taken from the front strips, it is required that the front and back energy signals differ by no more than 500 keV. Finally, a number of DSSD strips, ASIC channels, and CsI(Tl) detectors did not function properly or at all. These signals are excluded from the analysis of this dissertation.

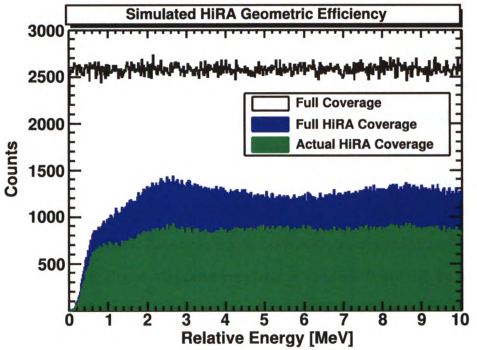

Figure 3.14 – HiRA geometric efficiency as a function of the relative energy.

3.3.6 Detector Efficiency

Previous measurements, as discussed in Section 1.4, have set a limit on the lifetime of ^{69}Br. The non-observation measurement of [43] set a limit on $S_p < -500\,\text{keV}$ which implies the Q-value for the proton decay is $Q_p > +500\,\text{keV}$. The geometric efficiency for HiRA was simulated with the Monte Carlo simulation from Section 3.1. Random Q-value decay events generated for ^{69}Br proton decay have an efficiency shown in Figure 3.14. The black histogram is the random Q-value decays that would be detected assuming HiRA had complete 4π coverage. The blue histogram is the events that would be detected for the current HiRA setup. The green histogram is the events that are actually detected after accounting for non-working and malfunctioning detectors. Above 500 keV the geometric efficiency is relatively constant indicating that if ^{69}Br is unbound by at least 500 keV the proton decays from the ground state should be observed.

3.4 MCP Calibration and Analysis

This dissertation constitutes the first implementation of the complete MCP tracking system in an actual experiment. Each MCP provides position information at two points along the beam, thereby providing the incoming angle and interaction position on the target. The raw position information is taken from the four corners of the MCP anode as described in Subsection 2.3.2 and sent to a charge-to-digital converter (QDC). Calibration of the raw charge signals into position is carried out with a target mask. Mask data was taken both with an α-source and the actual secondary beam. Finally, a mapping function is applied followed by a position correction involving the total sum of the corner signal amplitudes.

3.4.1 MCP Mask Calibrations

A brass target mask 0.155 mm thick containing a matrix of holes is used to map the raw corner signals to physical Cartesian coordinates. Figure 3.15 shows a rear (downstream) view of the target mask used for MCP 1. The mask is mounted to an L-shaped G-10 (an insulating fiberglass composite) target ladder so that it can be biased up to -1000 V, providing the electric field necessary to accelerate the secondary electrons ejected from the target foils. The smaller holes have a diameter of 1 mm while an "L" pattern, used for orientation of the mask pattern, is composed of six larger holes, each with a diameter of 2 mm. All holes are separated by a distance of 5 mm.

Particles that pass through the holes in the target mask are measured in coincidence with a secondary detector to obtain the mask calibration pattern. The calibration involving the α-source is carried out in coincidence with a plastic scintillator as shown in Figure 3.16. The photograph shows the MCP 0 (upstream) tracking detector. A target drive holds a ladder with two target foils; an aluminized target foil at the end of the drive and the target mask located nearest to the drive shaft. A

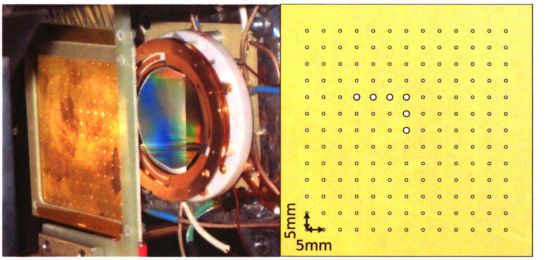

Figure 3.15 – (a) Photograph of a rear view of the inserted MCP 1 calibration mask and MCP 1 detector. The beam enters from the right of photograph. (b) Schematic drawing of the MCP mask. All holes are separated by 5 mm. The diameter of the smaller holes is 1 mm while the larger holes that make up the L pattern are 2 mm.

green PCB board that carries the corner signals, timing signal, and high voltage is shown mounted behind the MCP detector and one of the permanent magnets. The α-source is located upstream (left of the photograph). Particles that are not stopped in the brass mask and pass through the holes reach the scintillator. Events where a signal is generated in both the MCP and the scintillator produce a mask pattern as shown in Figure 3.17.

A calibration was also carried out with the secondary beam. The last quadrupole at the end of the last triplet in the S800 analysis line, shown in green just before the target in Figure 2.4, was turned off. Consequently, the beam is defocused at the target. Moreover, the incoming secondary beam particles arrive at the target with nearly parallel trajectories, *i.e.*, the incoming angle is $\sim 0°$. This optical configuration turned out to be extremely convenient for comparing information provided by the MCP tracking system and the S800 and is discussed in more detail in Section 3.6. The S800 focal plane is the secondary coincident detector for this calibration instead of the scintillator that was used in the α-source mask calibra-

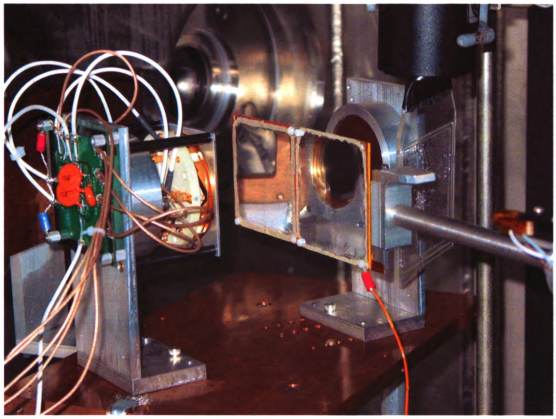

Figure 3.16 – Photograph of the MCP0 tracking detector during an α-source calibration. The beam enters the chamber from the left side of the photograph. Also shown is the upstream beam blocker in the background(left) as well as a scintillator(right) used for detecting α coincidences. The target drive enters at 60° supporting an aluminized mylar foil and calibration mask. The bias cable attached to the target ladder is also visible.

tion. While the α particles are stopped by the brass mask, higher energy secondary beam particles mostly pass through both the holes and the mask. However, beam particles passing through the brass lose enough of their energy that they are deflected from the spectrometer focal plane due to their reduced magnetic rigidity*. Uncalibrated mask patterns for both MCPs 0 and 1 are shown in Figure 3.18 for α particles and secondary beam particles.

* A ^{70}Se beam at 72 MeV/u passing though 0.5 mm of brass will emerge with an energy of 12 MeV/u.

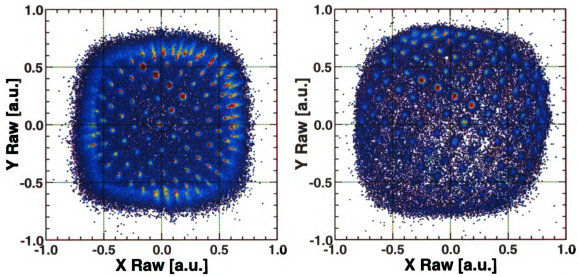

Figure 3.17 – MCP α-source uncalibrated mask pattern for (a) MCP 0 and (b) MCP 1.

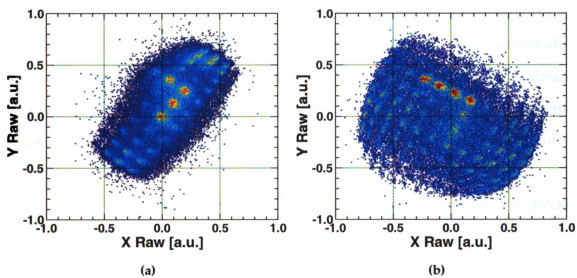

Figure 3.18 – MCP secondary beam uncalibrated mask pattern for (a) MCP 0 and (b) MCP 1.

3.4.2 Calibration and Fitting Procedure

Transforming the uncalibrated position spectra into calibrated physical Cartesian positions consists of the following steps,

1. Pedestals, or channels corresponding to signals with zero amplitude, are subtracted from the raw data and are initially taken from non-coincident data.

2. Pedestals are finely adjusted to maximize the uniformity of the mask pattern.

3. Position stability of the pedestals is checked as a function of the total sum of the corner signals (sum signal). This is done by comparing how stable the centroid positions of the mask holes for different ranges of the sum signal.

4. A 2D polynomial, $M(X, Y)$, is fitted to the mask pattern and maps the uncalibrated positions to physical positions on the target.

In step 1, a pedestal subtraction is done to set the QDC channel corresponding to zero signal amplitude. Data was taken on random triggers of the data acquisition and provide a best estimate for the pedestal value for each corner of the MCPs. In step 2, the optimum pedestal values are determined by incrementing and decrementing the estimated values and finding the pattern that maximizes the uniformity as shown in Figure 3.19. The pedestal settings will affect the center of the pattern the most severely since this is the region where the smallest corner signals are generated.

Once an optimum set of pedestal values is obtained, position stability is checked in step 3 as a function of the total sum of corner signals. Gates are placed on different holes of the mask pattern as shown in Figure 3.20a and the centroids of the hole positions calculated. The stability of the X and Y positions is checked by gating over different ranges of the sum signal. For each sum signal gate the centroid of the hole position is calculated and compared to the original hole position

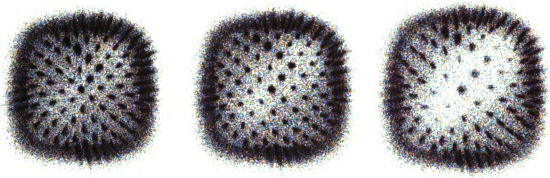

(a) (b) (c)

Figure 3.19 – MCP 1 mask pattern for (a) pedestal values -10 channels, (b) pedestal values 0 channels, and (c) pedestal values $+10$ channels.

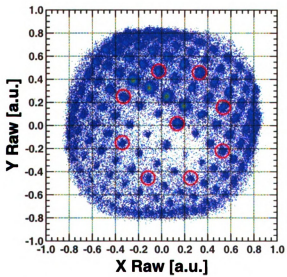

(a) Gates used to determine the centroid position of holes for testing pedestal stability.

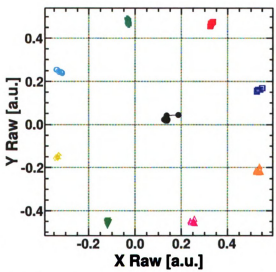

(b) Illustration of centroid stability for various mask holes gated on different sum signal ranges.

Figure 3.20

without a sum gate as shown in Figure 3.20b. This process is iterated over a set of pedestal values until the process converges to a pedestal setting where the shift of the centroid with the gate on the sum signal is minimized.

In step 4, a 2D polynomial up to 3rd-order maps the raw position information to the calibrated mask pattern. Each calibrated position, X and Y, is mapped by the function,

$$\begin{aligned} M_n(x_0, x_1) &= a_{n0} + a_{n1}x_0 + a_{n2}x_1 + a_{n3}x_0^2 + a_{n4}x_1^2 + a_{n5}x_0^3 \\ &\quad + a_{n6}x_1^3 + a_{n7}x_0x_1 + a_{n8}x_0^2x_1 + a_{n9}x_0x_1^2 \end{aligned} \tag{3.2}$$

where n=0 or 1 ($M_0 = X$ and $M_1 = Y$) and M_n depends on the two raw coordinates (x_0,x_1). This function takes into account some of the non-linear effects that are observed in Figure 3.18.

After calibration a correction to the XY-positions is made based on the sum signal. Figure 3.21 shows the Y-position dependence on the sum signal for MCP 1. Each vertical band corresponds to a column of holes on the target mask. Larger total summed signals are observed to be compressed compared to those with a smaller sum. After the sum correction an additional mapping function was applied for MCP 1.

3.4.3 Results and Discussion

The results of the calibrations are shown in Figure 3.22. The position resolution of the MCPs is clearly much better for the α-source calibration than for the secondary beam. Also, the background is larger for the secondary beam calibration. There are a number of factors that cause the beam and α-source resolutions to differ. First, the α-particles (^{4}He) have $Z = 2$ while the secondary beam nuclei have $Z \sim 34$. This should make the resolution of the beam better because the number of secondary electrons ejected from the foil is larger for the beam as compared to that of the α-

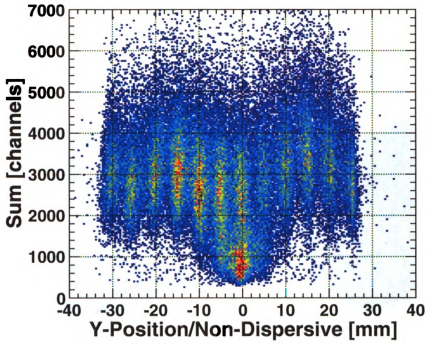

Figure 3.21 – MCP 1 corrected Y-position dependence on the sum signal.

particles due to the larger interaction with the Coulomb field. And, it is true that this results in large amplitude detector signals. The number of electrons is related to the specific energy loss given in Equation 2.7 which goes as $\sim Z^2/(E/A)$, corresponding to a factor of ~ 4 more electrons for the secondary beam in this dissertation. The angular distribution, however, of the ejected electrons should be greater than that of the few electrons ejected as a result of an α-particle. Investigations carried out in reference [69] show that this effect is real but it is not significant for the particle energies used by Shapira *et al.* More important is the increase in the width of the momentum distribution of the ejected secondary electrons from the higher incident energy beam. This results in an initial spot on the first micro-channel plate that is more broadly distributed in position than that of the α-particle due to the increased radius of the helical orbits of the secondary electrons in the magnetic field. The electron avalanche that follows is then spread over a broader distribution of positions. One solution to this problem is to increase the magnetic field so that the


X-Position/Diagonale [mm]
X-Position/Diagonale [mm]

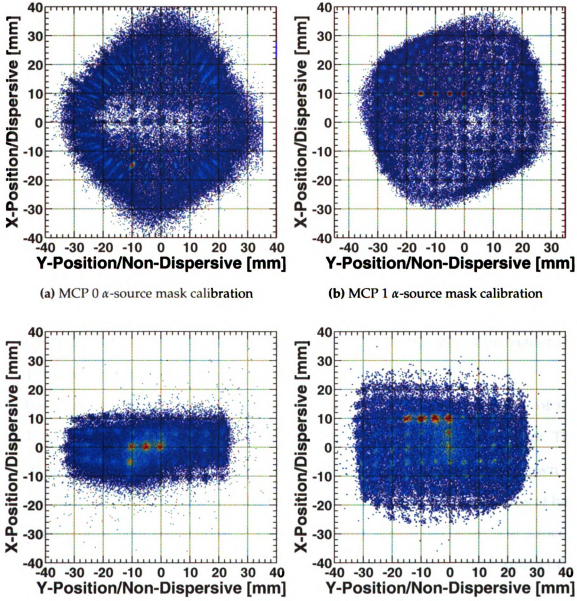

(a) MCP 0 α-source mask calibration

(b) MCP 1 α-source mask calibration

(c) MCP 0 beam mask calibration

(d) MCP 1 beam mask calibration

Figure 3.22 – Final MCP mask calibration spectra.

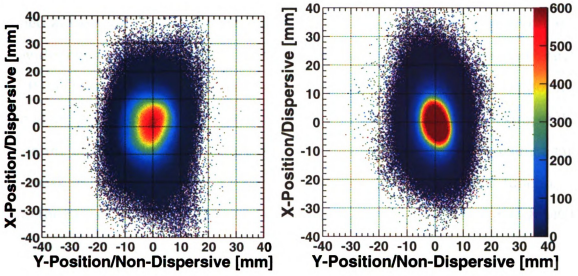

Figure 3.23 – Beam spots at (a) MCP 0 and (b) MCP 1.

trajectories of the secondary electrons take a more tightly confined flight path to the MCP. Indeed, this has been done in recent HiRA transfer reaction experiments that are currently under analysis and has resulted in a noticeable improvement in the position resolution.

For this dissertation it is not a requirement that the entire active area of the MCPs is accurately calibrated, only the area that overlaps with the beam spot. The beam spots take on the shape of an ellipse at both MCP positions as shown in Figure 3.23. At MCP 0 (upstream) the largest axes of the ellipse has a radius at half maximum of $\sim$ 1 cm while at MCP 1 (downstream), where the beam is at a focus, the radius at half maximum is $\sim$ 0.7 cm. Comparing the beam spot area to the calibrated regions in Figure 3.23 one can verify that the majority of beam particles are in a calibrated active region of the MCP detectors. This is important because the large size of the beam spot at MCP 1 requires that an event-by-event interaction correction for the position on the target to achieve the resolution needed for this experiment.

To summarize, the MCP tracking system consists of two MCP detectors positioned at two points along the beam. MCP 1 is located at the target position and provides event-by-event tracking of the interaction position on the reaction target. MCP 0 is located upstream of the target position and provides position information at an additional point along the beam thereby allowing for the tracking of the incoming beam angle. Calibration of the detectors is accomplished by using a target mask in coincidence with a secondary detector. A 2D polynomial function is fit to the raw mask pattern to obtain a calibrated position spectrum for each MCP that gives the physical position of the interaction.

Calibrations were performed using both an α-source and the secondary beam. However, there was a small difference in the calibration obtained for the α particles and the secondary beam. Therefore, we used the beam calibration for the final analysis of for MCP 1. For MCP 0 the beam did not cover enough of the active area, so the alpha source calibration was used and adjusted to match the mask pattern from the beam. By this procedure we obtain calibrations over the entire active area that overlaps with the size of the beam spot.

3.5 S800 Calibration and Analysis

The heavy ^{68}Se decay product of ^{69}Br is identified and analyzed in the S800 spectrograph. Additionally, the coordinates of the ^{68}Se nucleus at the target are determined through an inverse transfer mapping of coordinates measured in the S800 focal plane as described in Section 2.2. These measurements rely on the accurate calibrations and/or corrections of the detectors in the focal plane. A description of the corrections and importance of the E1 scintillator is given in Subsection 3.5.1. This is followed by corrections to the pad readout of the CRDCs in Subsection 3.5.2. The calibration of the non-dispersive direction of the CRDCs is explained in Subsection 3.5.3. Identification and analysis of the secondary beam is discussed in Sub-

section 3.5.4. Finally, the steps required to resolve the PID spectrum are described in Subsection 3.5.5.

3.5.1 E1 Scintillator Corrections

For this dissertation the E1 scintillator generates the S800 trigger and timing stop signal that is a reference for all other timing in the experiment. Typically, because the scintillator is so large, the timing signal is taken as the mean of combined signals of the upper, t_{up}, and lower, t_{down}, PMTs (shown in Figure 2.5 and is calculated as follows,

$$t = \frac{t_{\text{up}} + t_{\text{down}}}{2}. \tag{3.3}$$

The lower PMT did not function properly, however, and the time was instead calculated just from the upper PMT signal,

$$t = t_{\text{up}} \tag{3.4}$$

The signal from the upper PMT is split. One signal is sent to generate a logic trigger pulse which is sent into the S800 time-to-digital converter (TDC) and is used as the ultimate timing reference. The other signal is sent directly into the TDC and is the timing signal for the E1 scintillator. In other words, these two signals are generated from the same source and produce a "self-trigger". So, the timing signal for the E1 scintillator should be a sharply peaked Gaussian whose width reflects the intrinsic timing resolution of the E1 scintillator. The actual timing signal shown in Figure 3.24 reflects a different structure however; a doubled peak distribution is observed. The underlying cause of this problem is, as of yet, unknown but is suspected to be a problem associated with the S800 trigger electronics. This is a problem for the resolution of the PID spectrum that will detailed in Subsection 3.5.5. Particles in the focal plane are identified by plotting the ΔE signal from

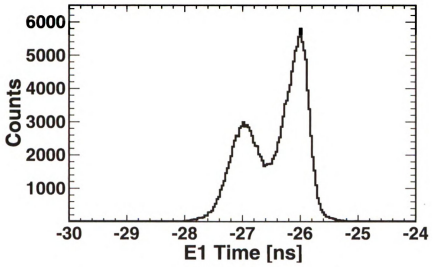

Figure 3.24 – Timing signal for the E1 scintillator.

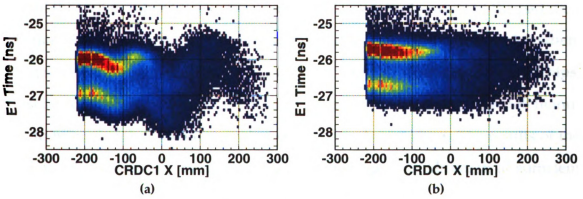

Figure 3.25 – The (a) uncorrected and (b) corrected E1 scintillator timing signal as a function of the dispersive position in the focal plane.

the ionization chamber against the particle's ToF. The wide and doubled peaked distribution shown in Figure 3.24 smears out the timing resolution and reduces the ability to resolve the reaction products. Furthermore, the E1 timing signal also depends on the dispersive position in the focal plane as shown in Figure 3.25a. The timing signal is improved by empirically correcting the average behavior as a function of the dispersive position at CRDC 2. The result of the correction is shown in Figure 3.25b.

3.5.2 CRDC Pad Calibration and Corrections

The CRDC pads run vertically along the sides of each CRDC as described in Subsection 2.2.4 and determine a particle's dispersive position in the focal plane through the induced charge on a distribution of pads. Their position is fixed with a pad pitch of 2.54 mm. Pedestal values for each channel are typically measured prior to the experiment with a pulser and are subtracted from the raw channel value.

CRDC pads are readout using the STAR FEE cards discussed in Subsection 2.2.4. Each chip processes 16 pads. While the gains within a chip are roughly the same, the gains between chips used in this dissertation were not well matched. Figure 3.26a shows the total induced charge, summed over a subset of data, as a function of the pad number (dispersive position). The center of gravity of the pad distribution is discontinuous at those positions that cross the chip boundaries where the gains change significantly. Therefore the channels, especially between chips, must be adequately gain matched. Each channel was individually adjusted manually to minimize the discontinuity between channels and chips. The results of the gain matching shown in Figure 3.26b are less than perfect, although of sufficient accuracy for this dissertation.

For this dissertation, it was only possible to set the global offset for the pad electronics as opposed to setting the individual offsets for each channel. Because the hardware gains between chips is poorly matched, this had the unfortunate consequence that some of the chips saturate while others have gains that are too low. This effect is visible in Figure 3.26a but is more clearly observed in Figure 3.27 where the amplitude for a single pad, when it is the pad with the maximum amplitude, is plotted against the ΔE signal from the ionization chamber. When calculating the center-of-gravity to obtain the dispersive position the saturated pads flatten the peaks and/or skew the distribution of pad amplitudes when the saturation values of all contributing pads are not the same. To correct for this effect a

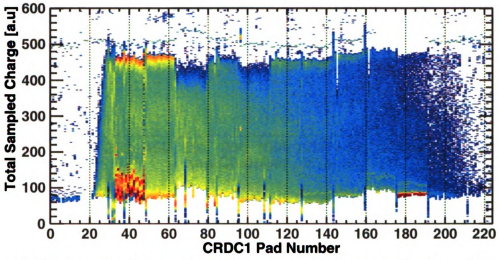

(a) CRDC 1 summed induced charge signal as a function of pad number without gain matching or set thresholds.

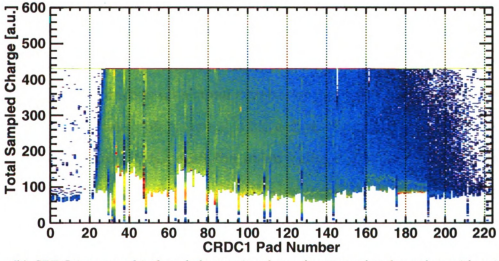

(b) CRDC 1 summed induced charge signal as a function of pad number with gain matching and set thresholds.

Figure 3.26

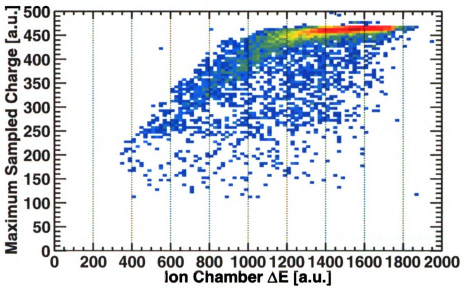

Figure 3.27 – Saturation of CRDC 2 pad 52.

maximum threshold value was introduced that limits the amplitude of all channels so that the saturation effect is minimized.

The center-of-gravity calculation is augmented by algorithms to eliminate the effects of events containing pads that are exterior to the main distribution as well as pads that are not functioning properly. Ions produced in the CRDC induce a Gaussian-like distribution on a small number of pads. For noisy events a pad outside of this main distribution may also have data. If this is included in the center-of-gravity calculation it can shift the mean value of the position. An algorithm removes these pads from the calculation when needed. In addition, a number of pads for this dissertation were not functioning as expected. The amplitude values for these pads are set to zero, which means that pad distributions in the neighborhood of such bad pads will be missing information. To correct for this effect an interpolation is done to estimate the amplitude of these pads before the center-of-gravity calculation.

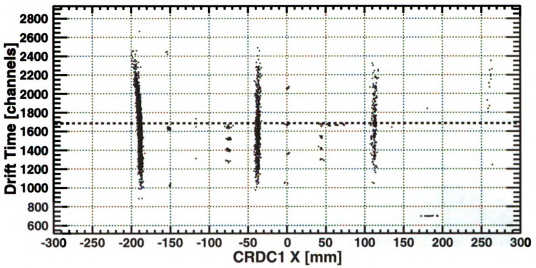

Figure 3.28 – CRDC 1 uncalibrated non-dispersive mask calibration spectrum.

3.5.3 CRDC Mask Calibration and Corrections

While the dispersive calibration is fixed by the pad pitch as discussed in Subsection 3.5.2, the non-dispersive, or Y-position, is determined by the drift time of the electrons in the ionized fill gas. A mask containing a hole pattern and a number of slits is inserted 8 cm in front of either CRDC 1 or CRDC 2. Only those particles passing through the apertures in the mask are detected and result in a position spectrum as shown in Figure 3.28. Each hole has a precise position and lies on a rectangular grid. However, the mask pattern in Figure 3.28 shows an apparent non-linearity in the y-direction which is clear if one considers the holes along $y = 0$. This is directly related either to the physical drift time, the timing of the drift, or both. The non-linearity depends on the dispersive position in the focal plane as is shown in Figure 3.29a. The timing signal is corrected by subtracting off the average dependence on x and the result is shown in Figure 3.29b. While one may initially think that the non-linear time dependence is very similar to that discussed in Subsection 3.5.1, it should be noted that these times, in principle, are not correlated.

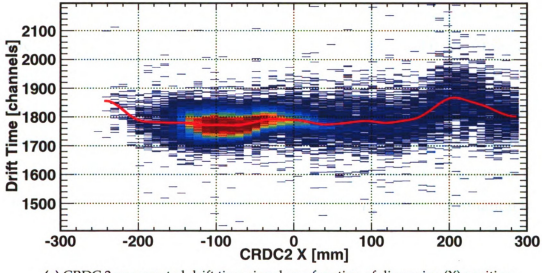

(a) CRDC 2 uncorrected drift time signal as a function of dispersive (X) position.

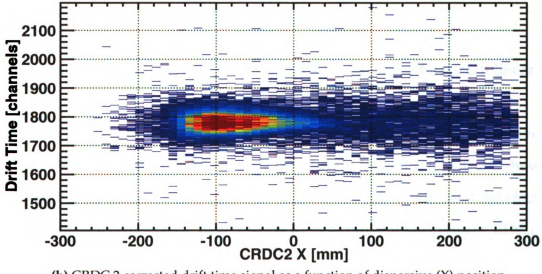

(b) CRDC 2 corrected drift time signal as a function of dispersive (X) position.

Figure 3.29

The E1 scintillator timing signal is fast, on the order of 10^{-9} s, while the drift time of in the CRDC is a factor of 1000 slower.

A linear fit to the center hole centroid positions is used to convert the raw time signal from channels to mm. For longer drift times the timing signal has an additional non-linear dependence which will be discussed in the following paragraphs. Therefore, only the holes located at short drift times were used in the fitting as their calibration is linear. Each mask is located 8 cm upstream from its CRDC: the calibration using each mask should take that distance into account. This means that the angle, or equivalently the position from the opposite CRDC, should be taken into account. A linear fit to the initial CRDC mask pattern is done to obtain the 1st order calibrations for both CRDCs. Next, the 1st order position information is used to correct for the angle of incidence on the focal plane. The Y-position is given by the following equation which takes into account the 1st and 2nd order mask position effect,

$$Y = b_1 + a_2 b_1 + a_1 a_2 t_{\text{drift}} \tag{3.5}$$

where b_i and a_i are the 1st and 2nd order offsets and slopes from each linear calibration.

A non-linear dependence also exists for long drift times. This is observed in Figure 3.28 and is clearly visible in a plot of CRDC 1 Y against CRDC 2 Y shown in Figure 3.30a for reacted beam data. As described in Subsection 2.2.4 the electrons drift in opposite directions; CRDC 1 drifts from y-min to y-max while CRDC drifts from y-max to y-min. Therefore, the non-linear drift time affects position tracking on both the left and right sides of the beam. Consequently, a correction is applied to y-min for CRDC 1 and y-max for CRDC 2. The correction forces $y1 = y2$ on the average and the result is shown in Figure 3.30b.

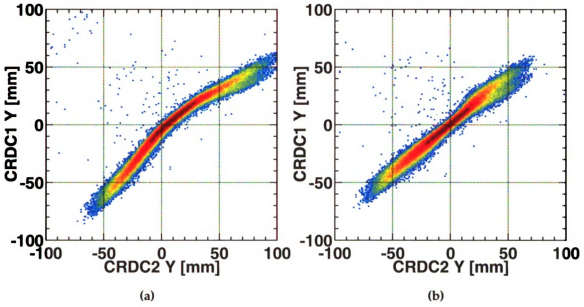

Figure 3.30 – CRDC Y1/Y2 (a) uncorrected and (b) corrected non-linear timing signal correction.

3.5.4 Secondary Beam Identification

The secondary beam is identified via a ToF-ToF method involving the timing scintillator at the XFP position of the A1900 and the OBJ position at the beginning of the S800 analysis line. In the non-relativistic limit of Equation 2.6,

$$B\rho \propto \frac{A}{Z} v \tag{3.6}$$

where v is the velocity of the beam particle. When filtering neutron deficient beams the A1900 selects a narrow range of isotones within the chosen momentum acceptance and beam optics uncertainties. Typically contaminants in the beam will have similar numbers of neutrons. The most likely fragment will differ by at most one neutron. At fixed $B\rho$ a decrease or increase in the A/Z ratio requires an increase or decrease in the fragment velocity respectively. Therefore a unique identification of the beam components can be made by comparing the ToF between well sepa-

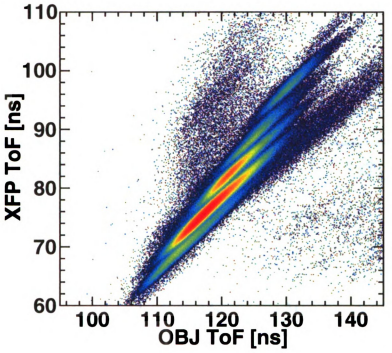

Figure 3.31 – Secondary beam PID based on the XFP and OBJ ToF signals.

rated plastic scintillators. This is done in Figure 3.31 where the ToF from the XFP to the E1 scintillator and the OBJ to the E1 scintillator are compared. For the reacted beam the problem with this method is that the ToF of the unreacted beam particles is folded with the distribution of ToFs of the reaction products, which have large variations in energy and therefore velocity, traveling from the reaction target to the focal plane.

An improved identification can be obtained if one removes the folding of the different fragment flight times from the target to the E1 scintillator. Let the distances and ToFs be defined according to Figure 3.32. Then, we can find the ToF from the XFP to the target, Δt_{target}, and from the target to the focal plane, the frag-

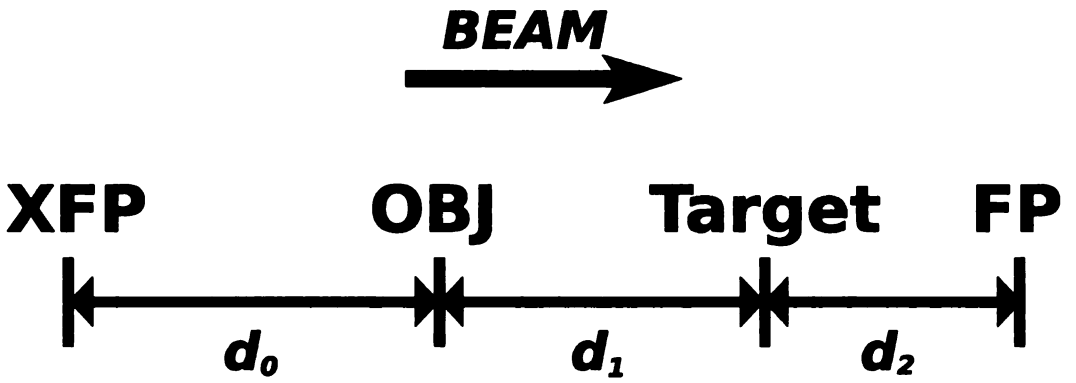

Figure 3.32 – Parameters for the ToF derivation.

ment velocity, $\Delta t_{\text{fragment}}$ in terms of the original timing signals,

$$\Delta t_{\text{obj}} = t_{\text{fp}} - t_{\text{obj}} = \frac{d_1}{v_{\text{beam}}} + \frac{d_2}{v_{\text{fragment}}} = d_1 \frac{\Delta t_{\text{target}}}{d_0 + d_1} + \Delta t_{\text{fragment}} \tag{3.7}$$

$$\Delta t_{\text{xfp}} = t_{\text{fp}} - t_{\text{xfp}} = \frac{d_0 + d_1}{v_{\text{beam}}} + \frac{d_2}{v_{\text{fragment}}} = \Delta t_{\text{target}} + \Delta t_{\text{fragment}}. \tag{3.8}$$

Subtracting Equation 3.8 from Equation 3.7,

$$\Rightarrow \Delta t_{\text{xfp}} - \Delta t_{\text{obj}} = \Delta t_{\text{target}} - \frac{d_1}{d_0 + d_1} \Delta t_{\text{target}} \tag{3.9}$$

$$\Delta t_{\text{target}} = \frac{1}{1 - \frac{d_1}{d_0 + d_1}} \left(\Delta t_{\text{xfp}} - \Delta t_{\text{obj}} \right) \tag{3.10}$$

$$= \frac{d_0 + d_1}{d_0} \left(\Delta t_{\text{xfp}} - \Delta t_{\text{obj}} \right). \tag{3.11}$$

Upon substitution of the above equations,

$$\Rightarrow \Delta t_{\text{fragment}} = \Delta t_{\text{xfp}} - \Delta t_{\text{target}} = \frac{-d_1}{d_0} \Delta t_{\text{xfp}} + \frac{d_0 + d_1}{d_0} \Delta t_{\text{obj}}. \tag{3.12}$$

This decouples the fragment velocities from the ToF. The incoming beam is identified as shown in Figure 3.33. The vertical bands represent each isotope in the beam. The x-axis is ToF from the XFP to the target and is purely the ToF of the unreacted beam. These particles are further resolved in the y-axis which is purely the ToF of

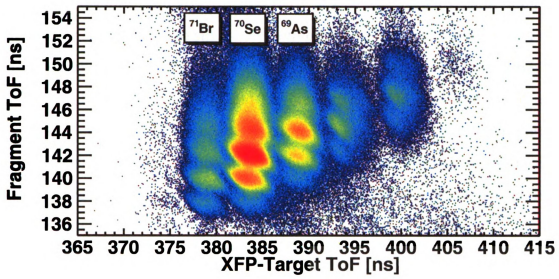

Figure 3.33 – Components of the secondary beam.

the reacted beam fragments, *i.e.*, the reaction products. Within the secondary beam there are three main components. They are identified as ^{71}Br (9.4 %), ^{70}Se (66.7 %), and ^{69}As (23.9 %).

3.5.5 Particle Identification

Particles that reach the S800 focal plane are identified with a ΔE-ToF method with the ΔE signal from the ionization chamber and the reaction product particle ToF given by $\Delta t_{\text{fragment}}$ derived in Subsection 3.5.4. In the previous sections corrections to the raw detector signals were described. In this section corrections for both the ΔE signal of the ionization chamber and the ToF that depend on the trajectory of the measured particles will be described as well as corrections due to time drifts of the detector signals. These corrections are required in order to uniquely identify and resolve particles based on their charge, Z and mass, A.

For example, a particle with a fixed Z, A, and total momentum, entering the focal plane at an angle of 0° has a shorter flight path through the focal plane detectors and therefore suffers less energy loss than the same particle with a more

divergent trajectory. Similarly, the first particle will also have a shorter ToF compared to the second particle since they both had the same velocity but travel over different path lengths through the spectrograph. To obtain the PID using the ΔE-ToF method both the energy loss and ToF for particles with a given Z and A must be corrected to remove these effects to allow PID gates that do not depend on the trajectories of the particles. Consequently, both the ΔE and ToF signals used for the PID have linear corrections that depend on the dispersive angle in the focal (AFP) plane and the X and Y positions in both CRDC 1 and 2.

Calibration parameters are obtained by eliminating the dependence of either the ΔE or ToF signal on the AFP and the CRDC X/Y positions. Since AFP is coupled to the X and Y positions this procedure is carried out iteratively until the dependencies are minimized. Moreover, once a coarse calibration is obtained a gate is applied to select a single intense isotope in the PID near the reaction products of interest in order to maximize the resolving effects of the correction for the reaction products in that region. The procedure is again repeated until the best correction parameters are found. Figure 3.34 shows the uncorrected and corrected dependencies of the ToF signal on the CRDC 1 X and Y positions (the ion chamber ΔE corrections are obtained in the same manner). Similar corrections are obtained for the dependencies on CRDC 2 and AFP.

The ToF signal depends directly on timing information from both the XFP and OBJ scintillators. Over the course of the experiment their efficiency decreases due to localized radiation damage caused by the bombardment of the beam. In addition to reducing the detection efficiency this damage also degrades the timing signals. To counter these effects the scintillators were periodically adjusted so that an undamaged region of the scintillator was used or, if an undamaged region did not exist, the scintillator was replaced. Throughout the experiment these changes in the scintillators result in unstable shifts which tend to smear out the timing

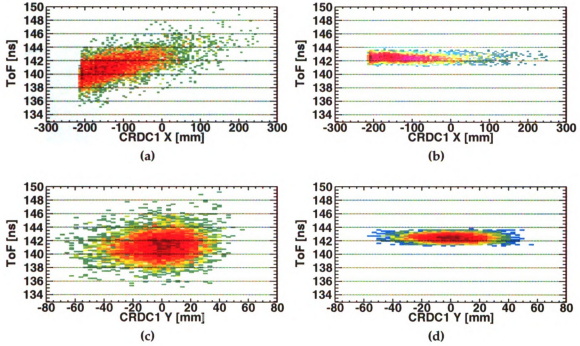

Figure 3.34 – Uncorrected ToF signal as it depends on CRDC1 (a) X and (c) Y compared to the corrected dependence on CRDC1 (b) X and (d) Y (gated on ^{69}Se). Similar corrections are done for ion chamber ΔE as well as the dependencies on CRDC2 X/Y and AFP.

signals. To minimized these effects the average shift in the reaction product ToF signals was determined on a run-by-run basis. The shifts are subtracted from a fixed reference ToF resulting in an improvement in the PID resolution as shown in Figure 3.35.

The final corrected S800 PID is shown in Figure 3.36. The loci of points in the PID plot represent the different nuclei produced in nuclear reactions with the target. From calculations using LISE++ as well as the position of the unreacted beams in this plot we determine the locus of points corresponding to ^{68}Se, the heavy product in the decay of ^{69}Br. Additional, the diagonal lines in Figure 3.36 correspond to isotopes of constant Z. The nearly vertical line on the left of the figure represents isotopes with $N = Z$.

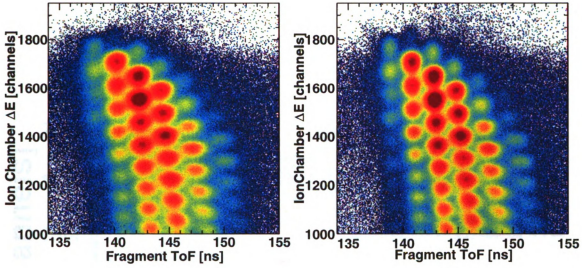

Figure 3.35 – PID of reaction products in the S800 focal plane for (a) uncorrected and (b) corrected ToF stabilization.

3.6 MCP & S800 Optics

The MCP tracking system and the S800 provide, to some extent, redundant information about the beam and its optical characteristics. The MCP tracking system provides a measurement of the $x - y - z$ interaction position on the target as well as the dispersive (ATA) and non-dispersive (BTA) angles of the *incoming unreacted beam*. Reconstructed events from the S800 provide a measurement of the Y-position (YTA) on target as well as the dispersive (ATA) and non-dispersive (BTA) angles for *particles detected at the focal plane*. Crosschecks of the calibrations between the MCP tracking system and the S800 are done by comparing the Y-position and angles. Consequently, it is found that inconsistencies in the tracking exist and result in the need for the manual construction of an inverse transfer map instead of using the S800 inverse map described in Subsection 2.2.3.

The beam tuning used during the MCP mask calibration described in Subsection 3.4.1 resulted in an extremely useful optical configuration for investigating the

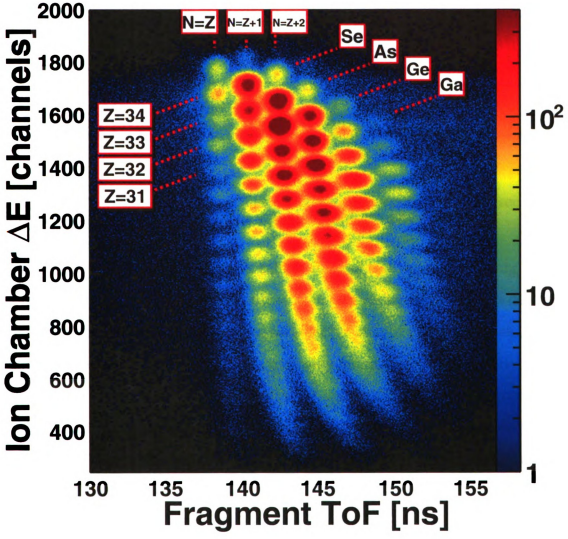

Figure 3.36 – S800 particle identification (PID).

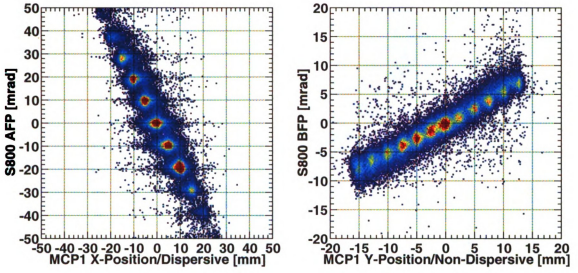

(a) (b)

Figure 3.37 – MCP 1 mask image illustrating the unique correlation between (a) the X-position and S800 ATA and (b) the Y-position and S800 BTA (b).

particle tracking. During the mask calibration the last superconducting quadrupole before the target chamber was turned off. As a result, the beam was defocused at the target allowing the beam to cover a larger area of the MCP mask. In addition it is found that the angles of the incoming beam particles are nearly parallel. This has the fortunate consequence that the X and Y positions on target correspond to unique dispersive and non-dispersive angles in the focal plane respectively as shown in Figure 3.37. One then has the ability to select events corresponding to individual mask holes independently of the MCP detector.

Let's first examine the correlation between the Y-position given by the MCP and that of the S800. Figure 3.38 shows the Y-position at the target as given by the S800 (YTA) as a function of the MCP Y-position for a MCP mask calibration using the secondary beam. The correlation is linear and the two devices are in good agreement with respect to the Y-position at the reaction target. However, the Y resolution of the MCP is slightly better than that of the S800. The MCP Y-position resolution is on the average $\sim$ 1.1 mm full width at half maximum (FWHM) ob-

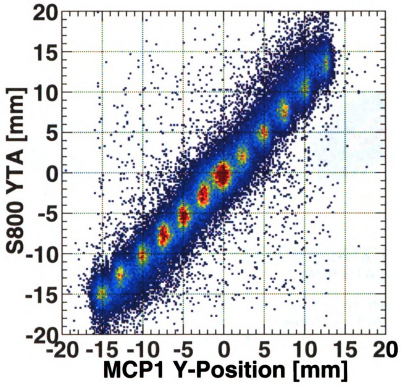

Figure 3.38 – Correlation of the Y-position at the target (YTA) for MCP 1 and the S800.

tained by a Gaussian fit of mask holes resulting from gates placed on positions in Figure 3.37* whereas the S800 YTA position resolution is $\sim$ 2.3 mm FWHM.

Next the dispersive and non-dispersive angles are compared in Figure 3.39 using unreacted beam data. While the non-dispersive angles are well correlated there exits a discrepancy with the dispersive angles. The distribution of dispersive angles given by the MCP tracking system is wider than that of the S800 and the correlation is not one-to-one. The good agreement between the non-dispersive angles indicates that the problem should lie with the angle given by the S800 since there is no difference in the way the MCP tracking system determines the angles. The validity of the angles measured by the MCP can be verified with the mask calibration data. Since the apertures in the mask are defined, so too is the angle

* Since the apertures in the mask have a finite radius this method of determining the resolution is only approximately correct since the distribution is not necessarily a perfect Gaussian.

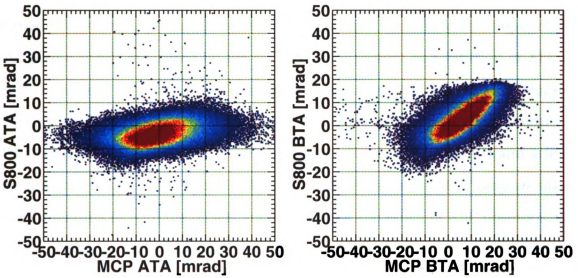

(a) Correlation between the S800 and MCP dispersive angles (ATA) at the target location.

(b) Correlation between the S800 and MCP non-dispersive angles (BTA) at the target location.

Figure 3.39

for a particle passing through any two given holes. Particular dispersive angles are picked out by gating on their corresponding holes and then compared to the angles calculated with the inverse map of the S800. Therefore, an inverse transfer map for ATA was manually generated using position/angle mapping information contained in the MCP mask calibration runs. Positions and angles in the S800 focal plane are mapped to the ATA at the target. The BTA, YTA, and kinetic energy deviation (DTA) are still calculated using the original S800 inverse map.

To first order the ATA is a linear function of the AFP as shown in Equation 3.13. This dependence is expressed in Equation 3.13 where a_r and a_f denote the ATA of the reaction product and the AFP,

$$a_r = A_0 + A_1 a_f = A_0(x_f) + A_1(x_f) a_f \tag{3.13}$$

$$= [B_0 + B_1 x_f] + [C_0 + C_1 x_f] a_f \tag{3.14}$$

In principle the coefficients also depend on XFP to higher order. The coefficients in Equation 3.14 are determined from the dependence of the offsets and slopes of the dispersive angles measured by the MCP tracking system as a function of XFP. A narrow range of XFP positions is selected and the corresponding offset and slope of the correlation between the MCP dispersive angles and the S800 AFP is produced. This is illustrated for one of the XFP range selections in Figure 3.40a and a fit of the centroid positions in Figure 3.40b. The coefficients for the MCP map are taken from linear fits of both the offsets and slopes over the range of XFP positions and are shown in Figure 3.40c and Figure 3.40d. From Equation 3.14 B_0 and B_1 are equal to the fit parameters in Figure 3.40c while C_0 and C_1 are given by the parameters in Figure 3.40d. Applying the MCP inverse transfer map removes the discrepancy in the dispersive angles as shown in Figure 3.41.

3.7 ^{69}Br Proton Emission

In the previous sections the methods of calibrating and correcting data collected by the MCP tracking system, HiRA, and the S800 spectrograph was described. Now, in this section, the collected data is processed and physical nuclear structure information is extracted. Gates are applied to the PID that select events, protons and ^{68}Se in the case of ^{69}Br decay, of a specific reaction as well as gates that exclude invalid events. Additionally, corrections related to an uncertainty in the total beam energy and its effects are described. Finally, an initial interpretation of the relative energy spectrum (proton capture Q-Value) for p+^{68}Se events is discussed.

3.7.1 Relative Energy Spectrum Construction

To properly construct a valid proton emission relative energy spectrum with minimum background contamination a number of gates are applied to the data. The relative energy is calculated using Equation 2.2. Consequently, this equation depends on the masses, kinetic energies, and relative momenta of the decay prod-

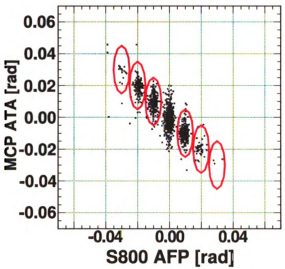

(a) Dependence of MCP dispersive angle at the target (ATA) on the S800 dispersive angle in the focal plane shown for a one of eight 12.5 mm wide gates on XFP.

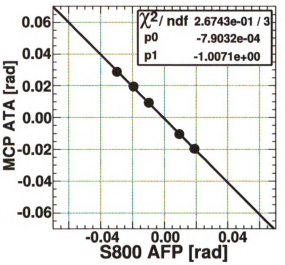

(b) Linear fit of the centroid positions of the mask holes in (a). Again, there are eight such plots, one for each gate on XFP.

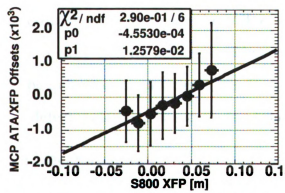

(c) Linear fit to the offsets of the eight linear fits illustrated in (b). The coefficients of the fit are used as parameters in the MCP inverse transfer map.

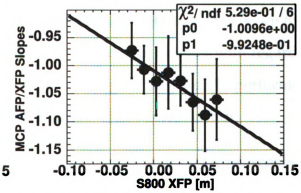

(d) Linear fit to the slopes of the eight linear fits illustrated in (b). The coefficients of the fit are used as parameters in the MCP inverse transfer map.

Figure 3.40

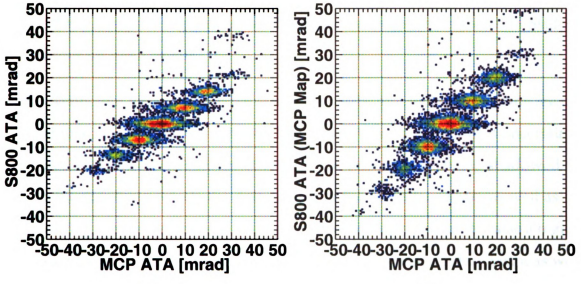

Figure 3.41 – Correlation between the S800 and MCP dispersive angles (ATA), from MCP mask calibration data, using the (a) S800 inverse transfer map and using the (b) manually created MCP inverse transfer map.

ucts. These quantities need to be determined properly as any misidentification or incorrect assignments will lead to an increased background in the relative energy spectrum thereby reducing the SNR of our signals. Certain detectors are known to have regions that do not respond in a predictable or accurate manner with regard to the detection of particles. Therefore, events occurring in these poorly performing detector elements are excluded from the analysis. These gates include,

1. The E-front (EF) and E-back (EB) energy signals from the HiRA telescopes must match to within 500 keV.

2. All malfunctioning strips or CsI(Tl) crystals in HiRA are excluded.

3. Events occurring in the middle DSSD strips (strips 15 and 16) are excluded since particles in these events may scatter into more than one CsI(Tl) crystal or miss the crystals completely.

4. Only events where a single particle is detected in HiRA with no more than 3 DSSD strips firing are included. This accounts for the correctable readout order problem events.

5. Events that have a dispersive position < -150 mm in the focal plane are excluded. This is a region in the CRDCs where there is a significant uncertainty in the calibrations. Additionally, this is the region that is being shadowed by a blocker that protects the detectors from the secondary beam as well as reducing the number of uninteresting unreacted beam events. It is also a region that is still intensely bombarded by a fraction of the secondary beam as well as scattered beam that tends to degrade the detector performance.

The relative energy spectrum is constructed using information from the MCP tracking system, HiRA, and the S800. Figure 3.23b shows the position information of the reacted beam used for correcting the angle of particles detected in HiRA as discussed in Subsection 2.3.2. In Figure 3.42a the S800 proton coincident yield is shown. In Figure 3.42b the ^{68}Se coincident particle yield is shown. We find there are $\sim$ 25 364 events involving ^{68}Se (with the gates described above applied). There are $\sim$ 12 865 single proton events that are detected in coincidence with ^{68}Se.

3.7.2 Beam Energy and CsI(Tl) Calibration Correction

Before constructing the final relative energy spectrum a correction involving the total beam energy is needed. In principle, the energy of the secondary beam can be determined from Equation 2.6 and the magnet settings of the A1900. While the magnitude of the magnetic field, B, is well known the effective radius, ρ, is not. Consequently, it is found that the energy calculated for the secondary beam using the A1900 magnetic rigidity is higher than that obtained by measurements with the S800 focal plane.

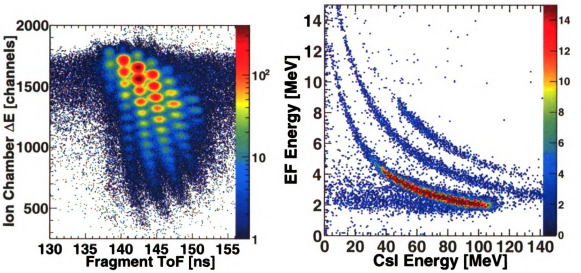

(a) Reaction products identified in the S800 coincident with a single proton in HiRA.

(b) Single protons in HiRA coincident with ^{68}Se in the S800.

Figure 3.42

This discrepancy has a direct effect on the measured HiRA particle energies since the magnetic rigidity of the A1900 is used in Subsection 3.3.4 to determine the energy of the elastically scattered protons in the CsI(Tl) calibration while the S800 rigidity is used to determine the recoil energy. However, if the calibrations are different the decay peak will become unacceptably broad. The discrepancy in the elastic scattering calibration point means that the calibration was defined to have a higher energy than it would have been assigned using the S800. However, by analyzing the relative energy for events where protons are emitted at forward and backward angles in the COM frame we can correct the CsI(Tl) energy calibration to make it consistent with the S800. In other words, decay protons emitted in the forward direction along the beam shall have the same relative energy as those emitted in the backward direction in the COM. If the CsI(Tl) calibration is incorrect then any observed decay peaks will have a mean value that depends on the proton angle of emission in the COM frame. Figure 3.43 demonstrates this effect. In Figure 3.43a a simulated proton emission from ^{69}Br with a Q-value of 810 keV shows

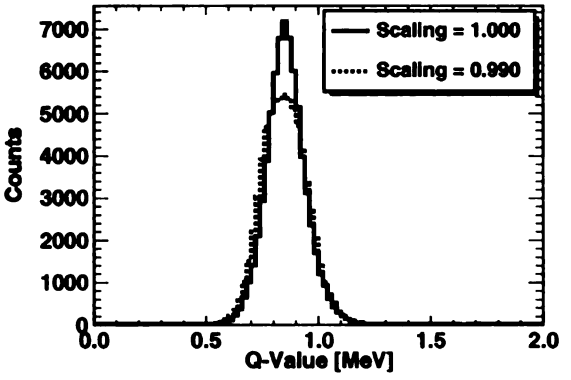

(a) Simulation of proton emission from a state in ^{69}Br with Q = 810 keV for unscaled (solid) and scaled (dashed) proton energies.

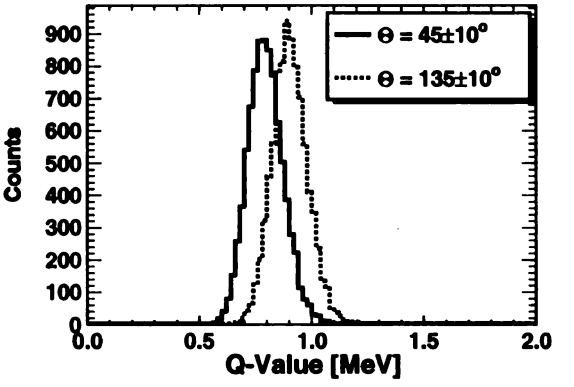

(b) Simulated peak gated on forward (solid) and backward (dashed) proton emission angles in the COM frame.

Figure 3.43

the change in resolution of the observed relative energy peak when the total proton kinetic energy is reduced by 1 % of its actual value. However, in Figure 3.43b we can clearly see the underlying cause of the broader peak. We observe that events at forward proton emission angles are shifted to lower relative energies while those at backward angles are shifted to high relative energies.

To account for the known beam energy discrepancy the total proton kinetic energy is scaled until the best overlap of the low relative energy peak for forward and backward angles is found. The difference in peak values as a function of the energy scaling factor is shown in Figure 3.44. A transition crossing through zero peak difference is observed when the proton energy is reduced by $\sim$ 0.8 %. This value for the difference in A1900 and S800 $B\rho$ calibrations is in agreement with other experiments performed at NSCL where kinematic information was used to find the scale factor. Consequently, the total energy of particles detected in HiRA is reduced by $\sim$ 0.8 % for all further analysis of the relative decay energy.

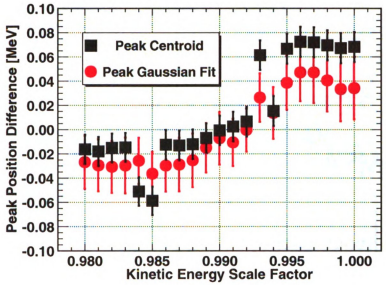

Figure 3.44 – Difference between the peak position for forward and backward proton emission angles (in the COM frame) for the low p+^{68}Se relative energy peak as a function of scaled total proton kinetic energy. The forward and backward peaks overlap when the energy is reduced by $\sim 0.8\,\%$.

3.7.3 Interpretation and Discussion

The final corrected relative energy spectrum for ^{69}Br proton emission is shown in Figure 3.45. Only events corresponding to the ^{70}Se incoming beam are gated to produce the spectrum. There are two main features contained in the spectrum: A continuous distribution of proton emission events at high ($E_{\mathrm{rel}} \gtrsim 1.4\,\mathrm{MeV}$) relative energies and a peak at low relative energies. These are all decays from quasistationary states formed mostly by the combined Coulomb and centrifugal barrier potentials discussed in Section 1.2.

Events at higher relative energies result from decays of many overlapping and unresolvable resonances. The production of ^{69}Br in its ground state is not a direct process in our experimental method. We rely on a highly energetic and/or multistep process through reactions of the secondary ^{70}Se beam and the target nuclei. In the simplest picture, we must pickup a proton and remove two neutrons in order

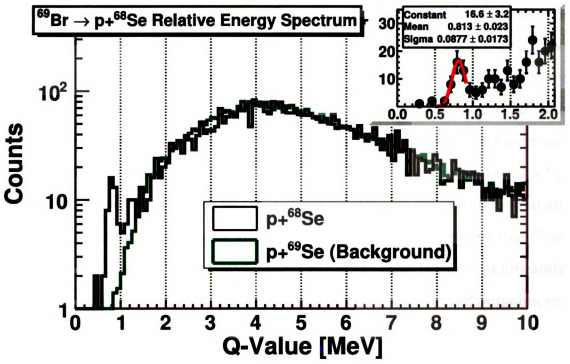

Figure 3.45 – Relative energy (Q-Value) spectrum for coincident p+^{68}Se events.

to reach ^{69}Br. As a result the ^{69}Br nuclei are left in excited configurations which undergo particle decay. However, the density of states ($\rho(E_x) \propto e^{b\sqrt{E_x}}$ in the Fermi gas model) is increasing for states with excitation energies, E_x, sufficiently above the ground state. Additionally, the width of the individual resonances, given by $\Gamma = \hbar/\tau$, is also increasing due to the rapidly decreasing lifetime, τ, that results from the larger Coulomb penetrabilities at larger excitation energies. Due to the increasing density of states and the increasing resonance widths it is not possible to resolve and identify contributions from individual states. The continuum of relative energies in Figure 3.45 is thus understood to be highly energetic (hot), short lived decays from a statistical distribution of resonances. The distribution rapidly falls to zero for the lowest relative energies. Here, the density of states is lower and proton emission rate is reduced due to the greater width of the barrier.

In these regards, the ^{69}Br nucleus is unusual due to its strong affinity for proton decay from all levels. One finds that, for all energy levels in ^{69}Br, the penetrabilities

are large due to the narrowing width of the Coulomb barrier with increasingly unbound energies. The γ-ray widths are not as large in neighboring particle stable nuclei because these nuclei have much lower ground state energies and the γ-decay rate increases strongly with the γ-ray energy, which increases as the ground state energy decreases. The high unbound ground state energy of ^{69}Br allows the proton decay branch to compete, and indeed dominate the γ-decay branch since $\Gamma_p > \Gamma_\gamma$. This is not the case, however, for less proton rich nuclei with ground states that are either bound or have proton separation energies that are more positive than ^{69}Br. For the low-lying levels in these nuclei the γ-ray decay rates increase significantly while the penetrabilities and proton decay rates of a proton with fixed outgoing energy (*i.e.* Q-value) remain the same. In these cases proton emission from the lowest excited states is greatly inhibited, since $\Gamma_p(E_x) < \Gamma_\gamma(E_x)$.

At the lowest relative energies, proton emission from individual states may be resolved. Here the density of states is low and proton emission from the ground state as well as low-lying excited states can be isolated. These states have significantly longer life-times compared to those in the continuous relative energy region due to the increased width of the barrier which is sensitive to the excitation energy as well as the l-value of the state. Furthermore, as just discussed, proton emission will dominate over all other decay modes, particularly γ-decay. Again, this is where ^{69}Br is unique. Proton emission from the ground state is the fastest decay mode as there are no lower energy states to γ-decay into nor is β-decay fast enough to compete. The peak at 812 keV in Figure 3.45 is in the energy domain dominated by these relatively long-lived decays. The peak lineshape and position is, we believe, likely the result of emission from the ground state and possibly nearby low-lying excited state(s) as modified by their lifetimes (see Section 4.3 and by the detector resolutions. The question as to the contributions of various states in terms of the observed peak line-shape is addressed in chapter 4.

In addition, one expects background events at low relative energies to be minimized. An advantage of our experimental method is that our background is restricted to charged particle events, specifically, proton emission. However, in principle, there can be background at low relative energies coming from proton decays to excited states in the daughter nucleus ^{68}Se. If some high-lying state decays to an excited ^{68}Se the excited state decay rate will be lowered by barrier penetration with respect to decay from the same original state to the ground state of ^{68}Se. But such decays to excited states will have low penetrabilities when compared to corresponding decays to the ground state. If the proton spectroscopic factors of higher lying states in ^{69}Br to the ground state of ^{68}Se are comparable to the decay to the excited state most of these nuclei will decay directly to the ground state, creating a large peak at larger relative energies in the spectrum. Such peaks are not observed. This will be discussed again in Section 4.6.

Strong evidence supporting the above discussion of proton and γ-decay branching ratios can be found in the comparison of the ^{69}Br proton emission spectrum to those for nuclei with bound states. In Figure 3.46 the p+^{68}Se events are compared to p+X events where X are other selected heavy reaction products detected in the S800 focal plane. At higher relative energies proton emission can compete with γ-decay due to the reduced barrier width through which the proton must tunnel. As the relative emission energy is reduced, the barrier width rapidly increases until γ-decay becomes the dominant process for nuclei with bound states. All other nuclei other than ^{69}Br will continue to γ-decay into bound states and, eventually, undergo β^+-decay. However, ^{69}Br is unbound and decay by proton emission is the exclusive decay mode since β^+-decay occurs on a 10^6 longer timescale and there are no low-lying bound states to γ-decay into. Consequently, we observe a low-lying decay peak in Figure 3.46 only for decays from ^{69}Br where the ground state is proton unbound.

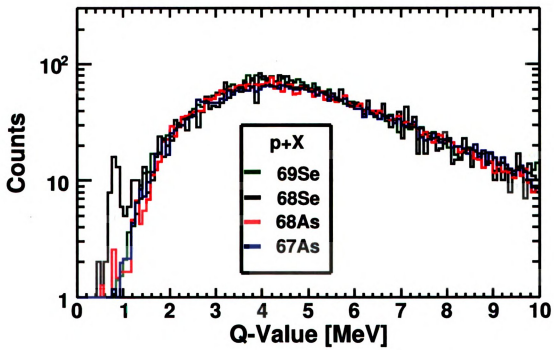

Figure 3.46 – Relative energy (Q-Value) spectrum for proton emission from ^{69}Se, ^{68}Se, ^{68}As, and ^{67}As normalized to the p+^{68}Se spectrum from $[6, 10]$ MeV as compared to the ^{69}Br decay.

Chapter 4

^{69}Br Proton Separation Energy and Consequences for the rp-Process

While chapter 3 discussed the process for producing the relative energy spectrum, this chapter details the methods to extract the ^{69}Br proton separation energy from the low relative energy proton emission peak and its consequences. A discussion concerning the possible formation pathways of ^{69}Br and a brief analysis of the momentum distributions of ^{68}Se is given in Section 4.1. Nuclear structure, including known information about the mirror nucleus ^{69}Se, that affects the interpretation of the low relative energy ^{69}Br decay peak is detailed in Section 4.2. In Section 4.3 particle emission from states that have a finite* lifetime is considered and the effect on the peak lineshape is analyzed. Section 4.4 expands upon Section 4.3, outlining the Wentzel-Kramers-Brillouin (WKB) approximation method used to calculate penetration through the barrier in order to obtain estimates for single particle lifetimes. In Section 4.5 the lifetimes calculated via methods in Section 4.4 are used in conjunction with a Monte Carlo simulation to extract the ^{69}Br proton separation energy. Possible uncertainties related to additional detailed nuclear level structure, deficiencies of the experimental setup, and a general lack of knowledge about the $N = Z \sim 34$ region will be addressed in Section 4.6. Finally, using the measured separation energy, results from a one-zone X-ray burst model and the consequences for the rp-process are explored in Section 4.7.

* In this context finite means long enough that the nucleus travels a significant distance past the target before decaying.

4.1 Formation Process

Disentangling the sequence of steps involved in the production of ^{69}Br is a challenge. Since reactions of the secondary beam with the target must eventually remove two neutrons in the case of ^{71}Br or remove two neutrons and add one proton in the case of ^{70}Se, the process is more complicated than a single neutron knockout mechanism. While it is not necessary for this dissertation to understand completely the formation mechanisms nor is there enough information to uniquely identify them, it is still interesting to make some comparisons of the data to simple production mechanisms. Analyzing the momentum distribution of the outgoing ^{68}Se reaction products can provide insight into possible formation processes.

In Figure 4.1 the ^{68}Se momentum distributions are shown for p+^{68}Se events which are the result of reactions of the ^{71}Br and ^{70}Se secondary beams with the target. Figure 4.2 shows the momentum distributions for the region around the low relative energy proton emission peak, again for both beams. To give some insight into the formation process, we compare the observed momentum distributions to three simple limits.

1. Projectile fragmentation of the secondary beam.

2. Complete fusion of a proton with the secondary beam.

3. Transfer reactions of the secondary beam on carbon nuclei in the target.

The results of these models are also shown in Figure 4.1 and Figure 4.2, and will be explained below.

Projectile fragmentation is the dominant mode for the production of rare isotopes at NSCL. It proceeds by rapid violent excitation of the projectile followed, in many cases, by a slower secondary decay characterized by the emission of neutrons, protons, and light particles. This violent excitation is sometimes modeled

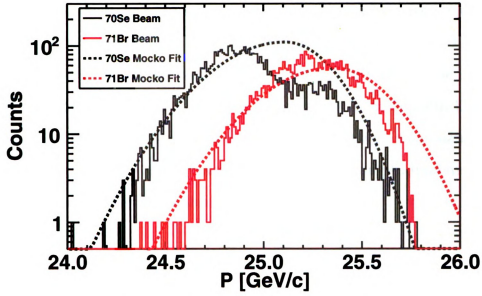

Figure 4.1 – ^{68}Se momentum distributions associated with the ^{71}Br and ^{70}Se secondary beams. The peaks are fit using the methods in the fragmentation study of Mocko *et al.* [4]. High momentum events for reactions involving the ^{71}Br beam are clearly missing due to the acceptance of the S800 spectrograph.

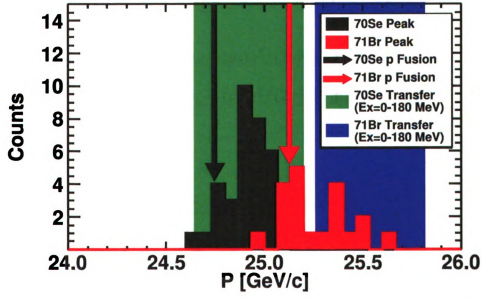

Figure 4.2 – ^{68}Se momentum distributions corresponding to the proton emission peak compared to the momentum expected from the simple proton fusion and transfer models described in the text.

by the "sudden" approximation in which a few nucleons are knocked out of the projectile leaving the remaining fragments intact with a momentum equal to the value it had in the beam nucleus in its ground state. Goldhaber modeled the initial nucleus by a Fermi gas, and derived an expression for the width of the longitudinal momentum (along the beam axis) distribution about its mean value [76]. In his original paper, he assumed the remaining fragment to have a Gaussian momentum distribution, $\exp(\vec{p}^2/(2\sigma^2))$, where the width of the longitudinal momentum distribution in the sudden approximation is given by

$$\sigma^2 = \sigma_0^2 A_F(A - A_F)/(A - 1), \tag{4.1}$$

where A is the mass of the projectile, A_F is the mass of the fragment, and $\sigma_0 \approx 90\,\mathrm{MeV/c}$. In practice, this expression only works well for light nuclei. For heavy beams, it under predicts the widths of the momentum distributions considerably. To describe these larger widths, Mocko *et al.* [4] fit a considerable number of fragmentation momentum distributions, $d\sigma/dp_z$, by the expression,

$$\frac{d\sigma}{dp_z} = \begin{cases} S \cdot \exp[-(p_z - \langle p_z \rangle)^2/(2\sigma_L^2)] & \text{for } p_z \leq \langle p_z \rangle, \\ S \cdot \exp[-(p_z - \langle p_z \rangle)^2/(2\sigma_R^2)] & \text{for } p_z > \langle p_z \rangle \end{cases} \tag{4.2}$$

where,

$$\begin{cases} \sigma_L^2 &= \sigma_{0L}^2 A_F(A - A_F)/(A - 1), \\ \sigma_R^2 &= \sigma_{0R}^2 A_F(A - A_F)/(A - 1). \end{cases} \tag{4.3}$$

Using this function, curves for the momentum distributions of ^{68}Se from the fragmentation of the ^{71}Br and ^{70}Se secondary beams are shown in Figure 4.1, where the widths are estimated from the data of Mocko *et al.* [4]. The peak momentum

distributions shown in Figure 4.2 clearly fall within the estimated fragmentation momentum distributions.

Complete fusion of a proton with the secondary beam is the second model we consider. The expected ^{68}Se recoil momenta for fusion involving the ^{71}Br (red arrow) and ^{70}Se (black arrow) beams are denoted in Figure 4.2. This model yields a value that is within the envelope of the observed momentum distribution, both for arbitrary proton energies and for the low Q-value gate. However, it is significantly lower than the peak values, *i.e.*, the momentum of a ^{68}Se recoil produced through fusion is lower than the center of the decay peak momentum distribution.

As a third model, we also consider the transfer of nucleons between the secondary beam and the carbon nuclei in the target for carbon excitation energies of 0 and 180 MeV. The range of excitation energy for both the ^{71}Br (blue) and ^{70}Se (green) secondary beams is shown in Figure 4.2. This simple transfer model gives a range of ^{68}Se momenta that, as with the fragmentation model, overlaps well with the observed momentum distribution. However, a somewhat higher excitation energy would be required to cover the range of the momenta produced in reactions with the ^{71}Br secondary beam.

For these comparisons we conclude that fragmentation, proton fusion, and transfer can contribute to the ^{69}Br production in this dissertation. However, fragmentation and transfer both predict the contribution from the ^{71}Br beam to extend past $P = 25.5\,\mathrm{GeV/c}$. This part of the focal plane was blocked by an absorber that was inserted to block the unreacted secondary beam. So, a significant part of the $^{71}\mathrm{Br}\rightarrow{}^{69}\mathrm{Br}$ reaction was probably lost due to the blocker.

Additionally, Figure 4.1 also highlights a number of analysis issues. In addition to the beam blocker, cuts were required in the dispersive position of the S800 to remove data from poorly performing regions in the CRDCs. This caused a reduced efficiency at the high momentum region of the momentum distribution for ^{68}Se

reaction products associated with the ^{71}Br secondary beam. For both reasons the relative energy spectrum is probably incomplete at high momentum due to a lack of acceptance for the ^{71}Br events.

Finally, there are concerns with ^{71}Br events that compose the decay peak as is observed by the distributions that are gated around the Q-value of the low relative energy peak. The distribution for ^{70}Se events are relatively narrow and well defined: the peak is at relatively low excitation in the transfer model. In comparison, the ^{71}Br decay distribution is much broader and mainly composed of contributions that would correspond to higher excitation in the transfer process. The lower excitation regions are behind the blocker. Thus, we may have excluded the correct excitation energy for decay from the low-lying levels in ^{69}Br. This, together with the overall lower yield for the ^{71}Br reactions, caused us to focus exclusively on reactions with the ^{70}Se beam.

4.2 Local Structure and the ^{69}Se Mirror Nucleus

In nuclear physics, the principles of charge symmetry and charge independence play a fundamental role in our understanding and formal treatment of the nucleus. Charge symmetry expresses the equality of the n-n and p-p nuclear interaction while charge independence expresses the equality of the n-p interaction and reveals that the attractive nuclear force is independent of charge. Charge symmetry is best illustrated in so called mirror pairs, or nuclei where the number of protons in one nucleus is equal to the number of neutrons in the other for a fixed A. More formally, for $N = Z$ the mirror partner of a nucleus with $(N, Z + X)$ is given by $(N + X, Z)$. The level structure of a given nucleus to the right of the $N = Z$ line, shown in Figure 1.1, is reflected in its mirror partner on the left side of the $N = Z$ line. A perfect symmetry would, qualitatively, yield a nuclear landscape where level structure, drip-lines, masses, etc. were perfectly reflected across the $N = Z$ line. Consequently, single particle states in one member of the mirror pair

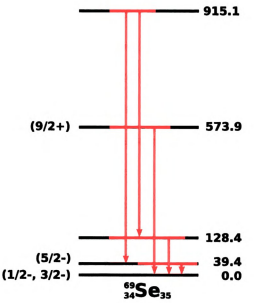

Figure 4.3 – Level diagram for the low-lying states in the ^{69}Se mirror nucleus.

would be identical to the levels in the other member. Surprisingly to a large extent the level structure in mirror nuclei are remarkably similar. Charge independence has led to the neutron and proton being treated as projections of a single spin-like object, the nucleon, and is expressed within the isospin (isotopic spin) formalism. However, this symmetry is broken by the Coulomb interaction as well as by small additional charge symmetry breaking residual interactions. Many of these effects manifest themselves in the richly complex nuclear landscape found in Figure 1.1. Despite the existence of charge symmetry breaking effects, mirror symmetry can be a useful tool to understand the properties of a given nucleus in terms of its better known mirror partner. In this section we use the structure of ^{69}Se, the mirror nucleus to ^{69}Br, theoretical shell model calculations, and experimental data to guide our understanding the possible level structure of ^{69}Br.

If isospin were an exact symmetry, one could exactly predict the structure of ^{69}Br from the structure of the mirror nucleus ^{69}Se. A diagram of the low-lying known levels in the ^{69}Se mirror nucleus [77] is shown in Figure 4.3. These are the only levels of any significance to our current analysis which contribute to the

low relative energy part of the spectrum in Figure 3.45. While the energies of a number of levels are known, the spin assignments are uncertain (as indicated by the parenthesis). As mentioned in Subsection 1.3.1, missing experimental information is fairly typical of nuclei near the proton-drip line. Nevertheless, the information in Figure 4.3 can still constrain our investigation. To begin, the three closely spaced low-lying states have spin-parities of $(1/2^-, 3/2^-)$, $(5/2^-)$, and (unassigned). Early measurements of ^{69}Se [78] indicated a preferred ground state spin-parity assignment of $3/2^-$, later studies however found a more probable assignment of $1/2^-$ [79,80,81]. At the highest excitation energies shown there is a state with a tentative spin-parity assignment of $9/2^+$, 573.9 keV above the ground state. Given our experimental resolution and the low statistics in Figure 3.45 we would not be able to resolve the lowest three states in ^{69}Br if this nucleus has the same level structure as ^{69}Se and if all three states are populated in the experiment. It is possible that the low-lying proton emission peak in Figure 3.45 is a convolution of proton emission from these three lowest lying states. If so, decays from all three states must be considered when extracting values for the proton separation energy and its uncertainty.

Alternatively, we could neglect isospin symmetry and look to trends in the neighboring nuclei in order to predict the structure of ^{69}Br. Nuclei in the region near $N = Z \sim 34$ are known to exhibit interesting structural characteristics. Deformation [82,83,84,85], shape coexistence [86,87], and possible mirror level inversions [85,88] are a few of the issues that can distort mirror symmetry while making this an important and challenging region of study. Small violations of mirror symmetry may be sufficient to change the order of the nearly degenerate ground state and 1st excited state in ^{69}Se shown in Figure 4.3, when such states appear in ^{69}Br.

Consequently, we should consider that the ground state spin may be inverted in ^{69}Br with respect to the ordering in ^{69}Se. If this is in fact true then the ^{69}Br ground

state would be assigned a single particle orbit of $l = 3$ (f orbital) as opposed to $l = 1$ (p orbital). This increases the width of the centrifugal barrier, thereby reducing the tunneling probability for the proton as discussed in detail in Section 4.3. While the proximity of the $5/2^-$ level to the ground state ($\Delta E = 39.4\,\mathrm{keV}$) suggests that only a slight perturbation would be needed to invert the level ordering, it should be noted there are no known exceptions of $T = 1/2$ mirror nuclei with inverted ground state spin orderings. Even if one broadens this to other mirror nuclei, there are very few exceptions to this rule.

For example, the only known exception for pairs of $T = 1$ mirror nuclei is the case of ^{16}N and ^{16}F, which is due to the so-called Thomas-Ehrman shift. While analog states in mirror nuclei, after accounting for Coulomb energy differences, are often essentially identical there are isospin non-conserving interactions that result in displacements of the analog levels. One of the main contributions to the level displacements was first suggested by Thomas [89] and Ehrman [90] who studied the levels in ^{13}C and ^{13}N. They found that in the more proton-rich member of the analog pair the proton radial wavefunction is distorted with respect to the neutron wavefunction in the more neutron-rich nucleus. The result is that the proton wavefunction is more extended and excluded from the nuclear interior, thereby reducing the Coulomb energy [52]. This is now known as the Thomas-Ehrman effect. Furthermore, it is found that the energy shifts are more significant for weakly or unbound levels than for bound states, due to the lowered Coulomb barrier, and result in systems that are *more bound* than they would be when just taking into account Coulomb displacement energies. The effect is also dependent on spin, with states of lower orbital angular momentum having larger shifts as a result of the lowered centrifugal barrier. This is also the case for the low-lying levels of ^{16}N ($2^-, 0^-, 3^-, 1^-$) and ^{16}F ($0^-, 1^-, 2^-, 3^-$) where one finds significant Thomas-Ehrman shifts [91]. Here, the last proton in ^{16}F is unbound, leading to

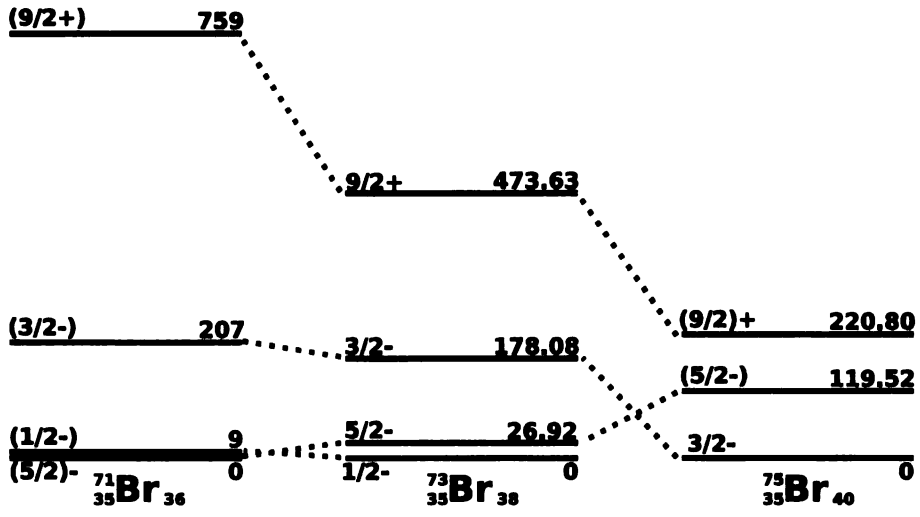

Figure 4.4 – Comparison of low-lying states in the ^{71}Br, ^{73}Br, and ^{75}Br isotopes.

more extended s-wave components of the 0^- and 1^- levels. The reduction in the Coulomb energy is significant enough that the 0^- in ^{16}F is shifted below the 2^- level to become the ground state, thereby altering the correspondance between the analog levels in this mirror pair.

Putting this aside for the moment, we note that an assignment of $5/2^-$ to the ^{69}Br ground state is also supported by shell model calculations using the GX1A interaction [92]. In addition, a crude systematic analysis of the odd Br isotopes near ^{69}Br shown in Figure 4.4 also suggests a ground state assignment of $5/2^-$. So it is reasonable to explore the possibility of an inversion in the ordering of the ground and first excited state in these nuclei.

To restrict our interpretation of the low relative energy ^{69}Br peak a set of assumptions will be applied in the analysis that follows.

1. Mirror symmetry is sufficiently obeyed and there is an approximate correspondence between the lowest lying analog states in ^{69}Se and those in ^{69}Br, although the relative spacing between states and their order may be shifted.

2. The ground state Nilson orbit for ^{69}Se will be taken to be $3/2^-$ with $l = 1$ as the dominant component. While recent measurements indicate that the ground state may be $1/2^-$ this has little impact on the analysis of this section. It is more significant that we choose $l = 1$ for the orbit.

3. The three low-lying excited states in ^{69}Br will be strongly populated relative to higher lying excited states, particularly the $9/2^+$ level, and will for simplicity be assigned spectroscopic factors of 1.

4.3 Lifetime Effects

So far a key element of nuclear decay has been ignored in this dissertation: the effects of finite particle lifetimes. Proton-emitting states in ^{69}Br are contained mostly by the Coulomb and centrifugal barriers. The lifetime of these states is dictated by the transmission through the barrier and observed as resonances in the decay spectrum. The lineshape corresponding to these narrow resonances can be described by a Lorentz distribution, characterized by a width, Γ. It is well known that the decay width and the lifetime, τ of a state are related by,

$$\Gamma = \frac{\hbar}{\tau}. \tag{4.4}$$

For a fixed orbit with specific l, the lifetime is largely determined by the excitation energy. As the excitation energy is increased the barrier width is reduced, decreasing the lifetime. However, states with larger orbital momentum have large centrifugal barriers, making their lifetimes significantly longer.

This is an issue for ^{69}Br since our setup relies on the assumption that the decay is occurring at the target location and that the nucleus is not stable long enough to decay at a position between the target and HiRA. If the lifetime of ^{69}Br is long enough, a significant fraction of the decays will occur beyond the target position

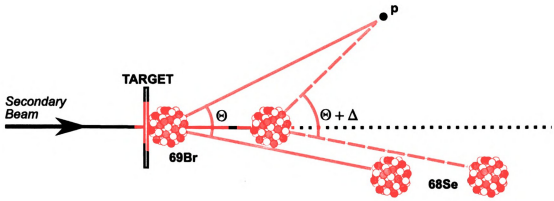

Figure 4.5 – Illustration of finite particle lifetimes on the determination of the emitted proton angle.

and the inferred relative angle between the proton and ^{68}Se will be reduced as shown in Figure 4.5. The error in the proton angle assignment due to lifetime will affect the lineshape of resonances in the relative energy spectrum. For a fixed decay energy the relative momentum, $\vec{p}_{\mathrm{p}} - \vec{p}_{^{68}\mathrm{Se}}$, will decrease since the relative angle decreases. The deduced relative energy for these events will therefore be reduced compared to the true value (see Equation 2.2). In general, the longer the lifetime the larger the number of decays that will be erroneously calculated with a reduced relative energy due to the lifetime effect, leading to tails on the decay peaks that extend toward lower relative energies. This effect is shown in Figure 4.6 where the proton decay from ^{69}Br for a Q-value of 810 keV is simulated for three different lifetimes. In addition to the low relative energy tails the peak height as well as its position is shifted as compared to those decays where $\tau = 0$ s.

The low-lying states in the mirror nucleus ^{69}Se can influence the lineshape of the peak in Figure 3.45. The $5/2^-$ state, assuming it is a pure f orbit, can have a lifetime two orders of magnitude longer than those from a p orbit. If the lowest levels in ^{69}Br are all populated then lifetime effects will have an impact on the lineshape and the determination of the true proton separation energy. For reference,

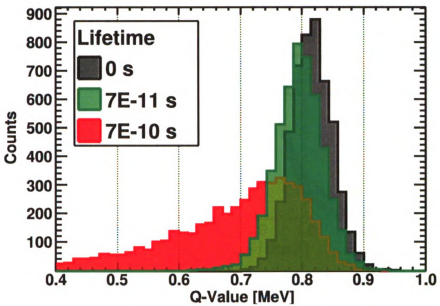

Figure 4.6 – Simulation of proton emission from states with finite lifetimes in ^{69}Br for $Q = 810$ keV.

it should be noted that resolution mainly affects the peak width, as demonstrated in Figure 4.7 where the CsI(Tl) energy resolution is varied for a fixed decay energy. This is a minimal effect compared to that of the lifetime; we conclude that the effects of single particle lifetimes are the largest source of systematic error.

4.4 Barrier Penetration in the WKB Approximation

To properly account for single particle lifetimes, and hence the peak lineshape, as a function of orbital momentum and excitation energy the Wentzel-Kramers-Brillouin (WKB) approximation is applied to calculate the transmission through the barrier. WKB is a well-known semiclassical calculation used to solve the Schrödinger equation for potentials that are slowly varying over the de Broglie wavelength, and typically for potentials for which the Schrödinger equation does not have an exact solution. It has been used successfully in many calculations of α-decay and typically provides half-lives that are within a factor of ~ 2 of the ac-

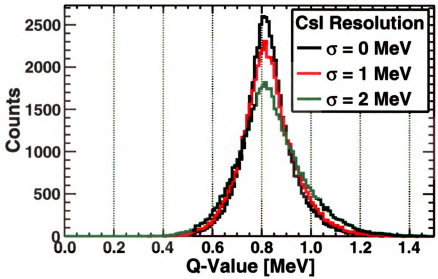

Figure 4.7 – Line shape dependence on CsI energy resolution. Changes in energy resolution effect the width of the peak distribution.

tual experimental measurements. Consequently, it has also been used in numerous studies of proton radioactivity.

Let us outline the main concepts of this approximation and the procedure for its application. Let's consider particle emission from the potential shown in Figure 4.8. The barrier presented to the proton is a superposition of a Coulomb potential, a nuclear potential (which also has a spin-orbit term), and a centrifugal potential. For a given excitation energy E there are two classical turning points with regard to the barrier denoted as R_{in} and R_{out}. Applying the WKB approximation the penetrability, or probability of transmission, for a spherical nucleus is given approximately by,

$$P = \exp\left[\frac{-2}{\hbar}\int_{R_{\text{in}}}^{R_{\text{out}}}\sqrt{2m_{\text{p}}(V(r)-E)}dx\right] \tag{4.5}$$

$$= e^{-2G} \tag{4.6}$$

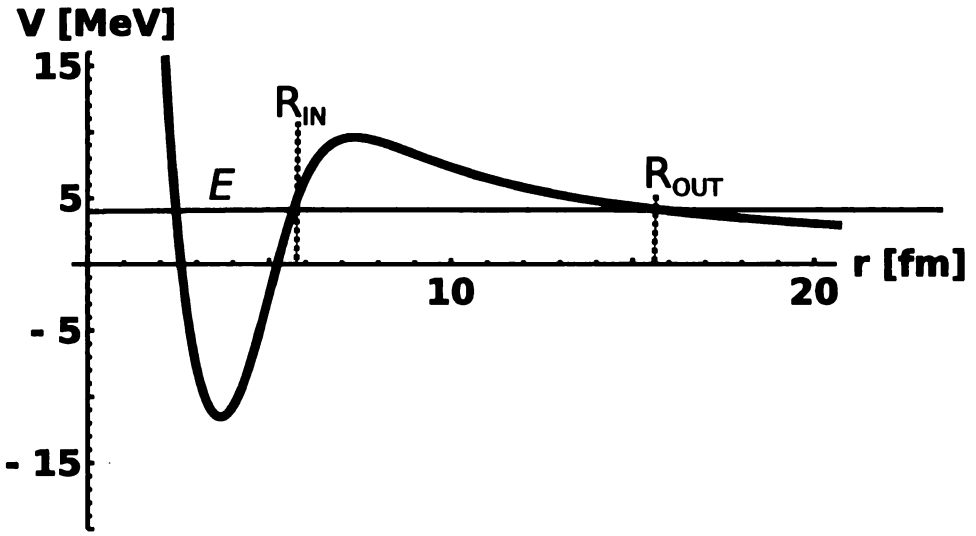

Figure 4.8 – Typical potential used for the WKB approximation.

where G is the Gamow factor [93]. The lifetime given the possibility of transmission through the barrier can be calculated as,

$$\tau = \frac{\hbar}{\Gamma} = \frac{1}{P \cdot \nu \cdot S}. \tag{4.7}$$

Here, P is the penetrability, ν is the collision frequency, and S is the spectroscopic factor that accounts for additional nuclear structure effects not accounted for by the WKB. The frequency with which the proton collides with the barrier is, from [94],

$$\nu = \frac{\sqrt{2}\pi^2\hbar^2}{m_p{}^{3/2}R_c{}^3(Z_1Z_2e^2/R_c - E)^{1/2}}. \tag{4.8}$$

where R_c is the charge radius of the nucleus.

For the lifetime analysis in this dissertation the real part of the optical model potential from Perey and Perey [95] is used. The full potential including the cen-

trifugal term is given by,

$$V(r) = \mathrm{Re}[V_c + V_n] + V_l \tag{4.9}$$

$$= V_c - V_R f(x_0) + \left(\frac{h}{m_\pi c}\right)^2 V_{so}(\sigma \cdot l)\frac{1}{r}\frac{d}{dr} f(x_{so}) + V_l \tag{4.10}$$

with the Coulomb potential V_c, a nuclear central term V_n, a spin-orbit term, and centrifugal potential V_l. More specifically,

$$V_c = \begin{cases} \frac{Z_1 Z_2 e^2}{r}, & \text{for } r \geq R_c \\ \frac{Z_1 Z_2 e^2}{2R_c}\left(3 - \frac{r^2}{R_c^2}\right), & \text{for } r \leq R_c,\ R_c = r_c A^{1/3}, \end{cases} \tag{4.11}$$

$$V_l(r) = l(l+1)\hbar^2/(2m_p r^2), \tag{4.12}$$

and $f(x_i)$ is a Woods-Saxon potential factor governed by the radius $r \sim A^{1/3}$

$$f(x_i) = (1 + e^{x_i})^{-1} \quad \text{where } x_i = (r - r_i A^{1/3})/a_i. \tag{4.13}$$

The parameters used in Equation 4.10 are are also taken from those listed for protons from Perey and Perey but originate from Becchetti and Greenlees [96].

$$V_R = 54.0 - 0.32E + 24(N - Z)/A + 0.4(Z/A^{1/3}) \tag{4.14}$$

$$r_0 = 1.17, \quad a_0 = 0.75 \tag{4.15}$$

$$V_{so} = 6.2, \quad r_{so} = 1.01, \quad a_{so} = 0.75 \tag{4.16}$$

The individual potentials and their superposition for $l = 3$ are shown in Figure 4.9.

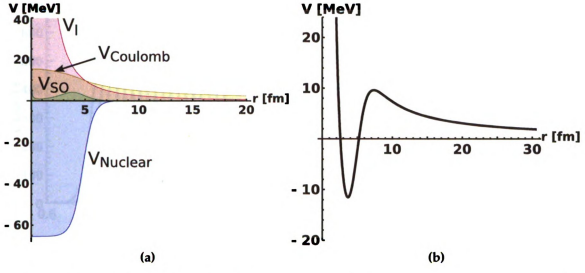

Figure 4.9 – (a) The various components of the optical model + centrifugal potential used to estimate lifetimes in the WKB approximation and (b) the summation of all potential components.

4.5 Fitting Methods and the ^{69}Br Proton Separation Energy

The goal of this section is to obtain a value for the proton separation energy by fitting the low energy region of the relative energy spectrum with simulated data that accounts for the peak lineshape in terms of the possible contributions from the low energy states in ^{69}Br and their lifetimes. First, the procedure used to generate the simulation data is discussed. This is followed by an analysis of the decay peak using the latest mass measurement studies, an analysis just using the mirror states, and finally an analysis that leaves the $5/2^-$ state from the mirror levels unconstrained in energy.

The simulation discussed in Section 3.1 is used to generate spectra for a given decay Q-value and lifetime. To get a sense of the significance of these effects the simulation was run for a set of Q-values for decay from both $l = 1$ and $l = 3$ orbits within the energy range of the low energy decay peak shown in Figure 3.45. The

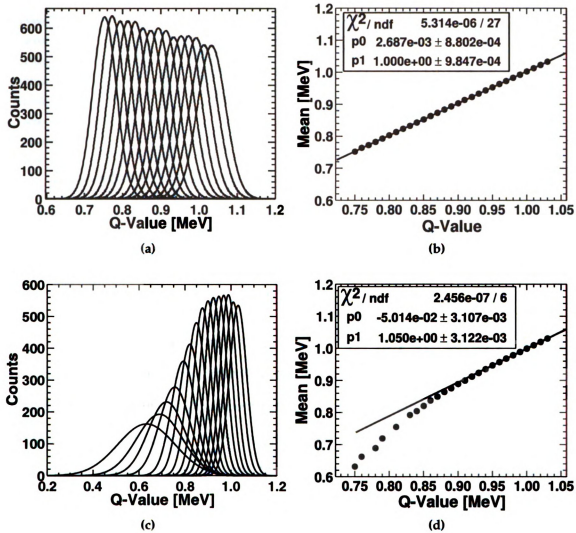

Figure 4.10 – Gaussian fits of simulated decay peaks produced over a range of relevant Q-values for (a) $l = 1$ and (c) $l = 3$ orbits. A comparison of the observed to actual decay Q-value is shown in figures (b) for $l = 1$ and (d) for $l = 3$.

peak positions of the simulated decay spectra are fit with Gaussian functions, as shown in Figure 4.10a and Figure 4.10c, for $l = 1$ and $l = 3$ orbits respectively. Figure 4.10b and Figure 4.10d show the mean peak position from the fit as a function of the actual simulated Q-value. The centrifugal barrier for $l = 1$ does not increase the lifetime such that there is an appreciable effect on the lineshape and the consequent determination of the separation energy. However, the $l = 3$ lineshapes have peak positions that begin to diverge from the actual Q-value. Therefore if an

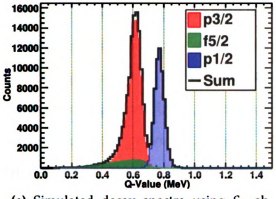

(a) Simulated decay spectra using S_p obtained from mass measurements+Coulomb displacement and the mirror states in ^{69}Se populated based on $2J+1$.

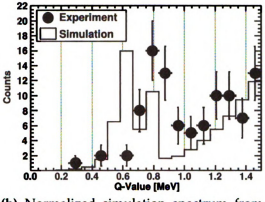

(b) Normalized simulation spectrum from (a) compared to the experimental data.

Figure 4.11

$l = 3$ emission is a large component of the low energy proton decay peak, it will tend to shift the fit peak position to a value that is lower than the actual Q-value. In addition, the observed peak position and lineshape will depend on the relative populations of the lowest states in the mirror nucleus which adds to the uncertainty. In the following we assume that all m-substates of the lowest three levels are equally populated. This means the levels are in proportion to the total angular momentum degeneracy, proportional to $2J+1$.

Initially, we will start the analysis by comparing the recent separation energy obtained from mass measurement together with information on the level scheme from the mirror nucleus. From Section 1.4 the precise measurements from Schury [2] and Savory [3] together with Coulomb displacement yield a value of $S_p = 636\,\text{keV}$. This value is taken as the energy of the ^{69}Br ground state. The energies of the first two excited states are set equal to those in the mirror nucleus ^{69}Se. The results of the simulated spectra without accounting for background are shown in Figure 4.11a. The relative background from Figure 3.45 is folded into the simulated data, normalized to the experimental results, and compared in Figure 4.11b. It is

clear that the simulated peak position is in poor agreement with the data. Moreover, if the ground state is the only contribution to the peak then the peak position will be at ~ 636 keV. This clearly does not reproduce the data.

Finding the best-fit of the peak lineshape based on the states of the mirror nucleus is accomplished by exploring the parameter space allowed by our assumptions stated in the previous sections. A Kolmogorov-Smirnov test [97], which tests whether or not two samples come from the same distribution, is applied to find the data that maximizes the goodness-of-fit probability. The method is explained in detail in Appendix A. This test has several advantages over a standard χ^2-test which include,

1. Advantageous for low statistics analysis.

2. Nonparametric test that is sensitive to the location and shape of the samples being compared.

3. Can be run on the unbinned data as opposed to fitting a binned histogram.

The next step in the analysis assumes that the calculated Coulomb displacement energy is incorrect but that mirror symmetry is obeyed. A collection of simulated data is produced with steps in the ground state Q-value of 5 keV while keeping the relative level spacing the same as in the mirror nucleus. The simulated unbinned data are compared to the unbinned experimental results and the best-fit is shown in Figure 4.12a. Figure 4.12b shows the probability values (p-value), with larger values indicating more statistical significance, for each set of simulated data as a function of the Q-value. We obtain a proton separation energy from this procedure of $S_p = -785^{+34}_{-40}$ keV and a best-fit p-value of 0.86. The uncertainty is taken from the 95 % confidence level given by the results shown in Figure 4.12b together with a 30 keV uncertainty related to the HiRA detector positions.

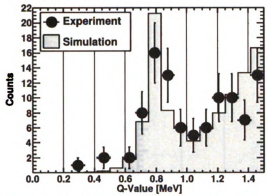

(a) Best-fit of the experimental data from a set of simulations with the same level spacing as in ^{69}Se but with 5 keV steps in the ground state Q-value. The best-fit to the experimental data is chosen using the Kolmogorov-Smirnov probability test.

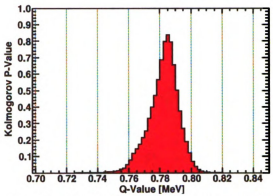

(b) Probability value distribution for each Q-value step in the simulations as a function of Q-value. The best-fit corresponds to the set of data with the largest probability value.

Figure 4.12

Next, since the lowest two states provide the dominant contributions to the peak and the $l = 3$ orbit contributes mostly to the low energy tail, we allow the $5/2^-$ level to be unconstrained in energy with respect to the other mirror levels. The procedure is the same as was performed for the strict mirror symmetry test except now the simulation also iterates over various $5/2^-$ level energies. Interestingly, a best-fit is obtained when the $5/2^-$ level is the ground state with $S_p = -735\,\text{keV} \pm 72\,\text{keV}$ and the $3/2^-$ with the $3/2^-$ placed at an excitation energy of $E_x = 805$ keV. The best-fit simulated data has a p-value of 0.91 and is shown compared to the experimental data in Figure 4.13. This result means that the mirror states could actually be inverted which would be the first such occurrence in a $T = 1/2$ nucleus (see discussions in Section 4.2), although the possibility of such a change in level ordering has been argued before [88, 85]. For this result the $5/2^-$ state would be shifted down relative to the $3/2^-$ by 109.4 keV.

We must now question the reasonability of such a level inversion, given that the inversion of $T = 1/2$ mirror levels is unprecedented. There is not much in-

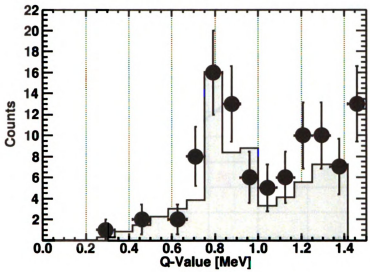

Figure 4.13 – Best-fit of the experimental data from a set of simulations with the level in ^{69}Se but with the $5/2^-$ level unconstrained in energy. The best-fit suggests that the $5/2^-$ and the $3/2^-$ are inverted compared to the mirror nucleus.

formation to constrain our thinking but one may get some ideas by looking at the systematic trends in the region. The systematics of the ordering of Nilson orbits was already shown in Figure 4.4. A systematic lowering of the $5/2$ Nilson orbit is observed as a function of neutron number, which might suggest an inversion of the mirror levels in ^{69}Br with the $5/2^-$ as the ground state. Figure 4.14 shows another representation of the systematic trend for the excitation energy of the $5/2^-$ for the nearby odd A Br isotopes. Extrapolating it to ^{69}Br suggests a $5/2^-$ ground state.

Finally, there exists the much simpler possibility that the low relative energy decay peak is only composed of proton emission from a single state. Therefore, the same analysis and statistics methods are used to determine the proton separation energy assuming emission from a pure $p_{1/2}$, $p_{3/2}$, and $f_{5/2}$ orbit. The values found are -784, -784, and -841 keV respectively.

In summary, it is found that there are five overlapping predictions for the separation energy dependent upon our initial assumptions. It should be noted that the peak location is mainly determined by the $3/2^-$ state since the relative con-

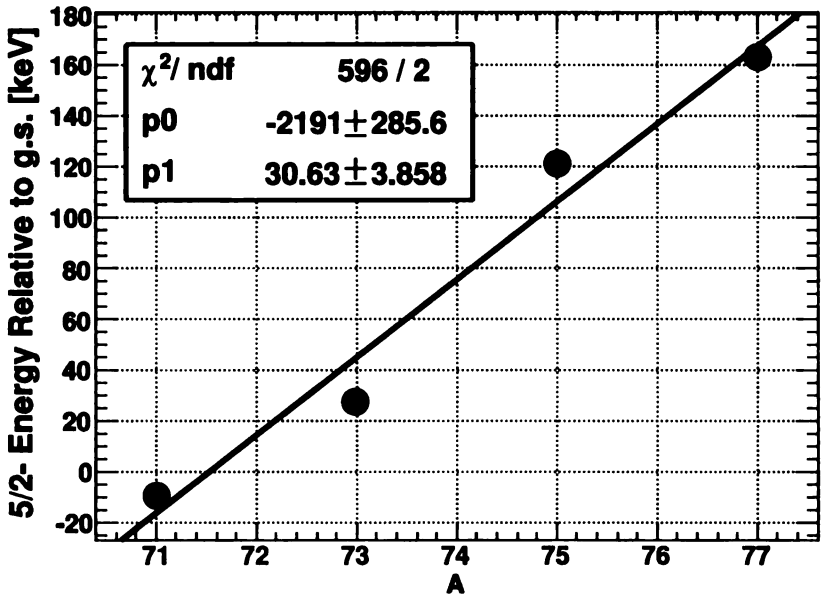

Figure 4.14 – Systematic trends and the predicted level spacing in ^{69}Br based on the known structure of the nearest Br isotopes.

J^π Ordering	Mass Excess [keV]	S_p [keV]
$1/2^-$,-,-	-46116^{+34}_{-64}	-784^{+34}_{-64}
$3/2^-$,-,-	-46116^{+34}_{-64}	-784^{+34}_{-64}
$5/2^-$,-,-	-46059^{+32}_{-36}	-841^{+32}_{-36}
$3/2^-$,$5/2^-$,$1/2^-$	-46115^{+34}_{-40}	-785^{+34}_{-40}
$5/2^-$,$3/2^-$,$1/2^-$	-46165^{+58}_{-72}	-735^{+58}_{-72}

Table 4.1 – Summary of the predictions for the ^{69}Br proton separation energy from this dissertation and their corresponding assumptions.

tribution from the $5/2^-$ state mainly determines the tail at low relative energies. These results are summarized in Table 4.1. The mass excess is calculated using Equation 1.5. The uncertainties for the separation energy is assigned based on the p-values calculated during the fitting procedure (see Figure 4.12b) and added in quadrature with an uncertainty of 30 keV which accounts for uncertainties associated with the detector positions. Given that there are no known $T = 1/2$ mirror nuclei where the ground state and first excited state are inverted we adopt the value found for the ^{69}Se mirror levels of $S_p = -785^{+34}_{-40}$.

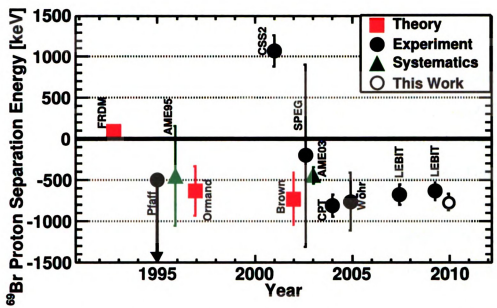

Figure 4.15 – Comparison of the ^{69}Br proton separation energies obtained in this dissertation to previous works.

Our suggested value is compared in Figure 4.15 to some of the previous studies discussed in Section 1.4. Predictions based on pure theoretical calculations are shown as red squares. Predictions based on experimental measurements of ^{68}Se and/or ^{69}Se are shown as filled black circles. Both of the Atomic Mass Evaluation (AME) from 1995 and 2003 are shown as green triangles. Finally, our suggested value is shown as an open black circle. The proton separation energies found in this dissertation are in agreement with the lower limit set by Pfaff [43]. Furthermore, the values are in good agreement with those obtained using the latest LEBIT high precision mass measurements combined with Coulomb displacement energy calculations, although this dissertation finds ^{69}Br to be slightly more unbound. It is interesting to note that the timespan over which measurements have occurred is roughly 20 years. Clearly there is also a wide spread, especially early on, in the predicted values owing to the fact that this is a difficult region to access. It is also difficult to properly understand in terms of theory due to the large uncertainties in the nuclear structure.

4.6 Possible Influential Factors on the Proton Separation Energy

There is a question regarding the physical reason why the proton separation energy found in this dissertation is higher than what is found when utilizing Coulomb displacement calculations. The uncertainty associated with the highly precise penning trap measurements is less than a few keV and the predictions based on Coulomb displacement calculations are typically good within $\sim$ 100 keV [12, 1]. The proton separation energy found in Section 4.5 are at least 100 keV higher than those predicted from the LEBIT mass measurement and Coulomb displacement prediction of Savory *et al.* [3]. Additionally, the Thomas-Ehrman effect, which reduces the Coulomb energy for unbound states, implies that ^{69}Br should be *more bound* than what is predicted with Coulomb displacement. Consequently, it is useful to address some of the possible factors that may influence predictions of the ^{69}Br proton separation energy as well as our measurement. There are a number of possibilities to consider,

1. The LEBIT mass measurements may have a larger systematic error.
2. There may be an unknown systematic error in our ^{69}Br experiment that has not been taken into account.
3. The low energy peak observed in Figure 3.45 may not correspond to emission from the ground state.
4. Deformation and other structure effects can affect the energy levels.
5. The electromagnetic spin-orbit effect may contribute to the Coulomb displacement energy (CDE).

Item 1, while possible, seems very unlikely especially on the level of 100 keV that we are discussing. Item 2 is also difficult to address as it is a complete unknown. This section will attempt to address the last three of these possible differences.

Thomas-Ehrman shifts, especially in light nuclei, can be quite large (as much as a few 100 keV) [98]. Since ^{69}Br is unbound it then may be a surprise to some that this dissertation predicts a less bound ground state as compared to recent predictions involving Coulomb displacement energies, which are the opposite of what one would expect from Thomas-Ehrman. However, recent Coulomb displacement energy calculations are constructed to account, although perhaps rather poorly, for these effects. Results of calculations done by Ormand [52] suggest that near the proton-drip line Thomas-Ehrman shifts should be contained within the uncertainty of the theoretical calculation which were estimated to be 100-250 keV by reference [52]. Similar calculations by Brown [1] are used to determine the separation energy given the mass measurements from Schury *et al.* [2] and Savory *et al.* [3]. From these arguments one may conclude that some of the possible Thomas-Ehrman shifts may be taken into account by the theoretical calculation. Nevertheless, it would be interesting to have more detailed theoretical calculations of the Thomas-Ehrman shift for ^{69}Br.

While a full discussion of the effects of nuclear shapes and their influence on shifts in mirror levels is beyond the scope of this dissertation, they are still worth briefly exploring for the region near ^{69}Br. In general the levels in a deformed nucleus can be described within the Nilsson model as well as by more advanced theories. In general, the Coulomb energy in such systems is sensitive to the overall nuclear shape [99]. For example, recent investigations into the mirror nuclei ^{71}Kr and ^{71}Br by Urkedal and Hamamoto [85] suggested an inversion of ground state spins based on possible nuclear deformation. Fisher *et al.* [88] addressed these ideas with further investigations of the spectroscopy of ^{71}Br. While an inversion of

the ground state was not found, evidence for oblate-prolate shape coexistence was observed. Perhaps more significant is the case of ^{69}Se since it is the mirror partner of ^{69}Br. Wiosna *et al.* [100] was the first to discover an oblate structure for the $g_{9/2}$ band in ^{69}Se which was followed by an extended study by Jenkins *et al.* [84]. In addition, an oblate ground state band structure for ^{68}Se was found by Fischer *et al.* [101]. There is a clear tendency for the isotopes in the region of $N \approx Z \approx 35$ to exhibit a multitude of deformation effects. The uncertain role of such effects should not be discounted as a possible contribution to the differences that exist in the separation energies discussed in this dissertation.

The next question that needs to be addressed is whether the observed decay peak actually corresponds to the true ground state decay. The first concern is that the decays to ^{68}Se are not ground state to ground state and instead a large number of decays go to the first excited state in ^{68}Se. However, the first excited state in ^{68}Se has an energy of 854.2 keV. This relatively large Q-value difference in the decay of ^{69}Br will most likely leave ^{68}Se in its ground state and should not contribute to a mismeasurement of the ground state decay. More precisely, if the observed proton decay at $Q = 785$ keV is to the excited state at $E_x = 854.2$ keV, the Q-value for ground state decay would be about 1.6 MeV. Barring a large spectroscopic factor, the relative branching into this excited state can be calculated using the WKB approximation to be $B_r = \Gamma_{Ex}/\Gamma_{g.s} \sim 10^{-4}/10^{3} = 10^{-7}$. Thus, comparable spectroscopic factors would dictate the observation of an excited state peak of 5×10^{8} counts in the spectra in Figure 3.45 at 1.6 MeV, given the observed yield of 50 counts in the low relative energy peak. To be consistent with it being a decay to the ^{68}Se excited state and the observed yield the spectroscopic factor to the ground state for this level would have to be $< 10^{-7}$. This would seem to be rather small considering that both ground and first excited states of ^{68}Se are believed to be members of the same rotational band [102].

The second concern relates to the possibility that the process by which we produce ^{69}Br results in the population of an isomeric state and that we never actually populate the ground state. It is well known that low-lying states in this region have negative parity. However, there is a $g_{9/2}$ intruder state that also appears with positive parity. Due to the mismatch in angular momentum and parity, γ transitions from this $9/2^+$ state to the ground and low-lying negative parity states are restricted. In ^{69}Se the state is relatively long lived given its excitation energy of 573.9 keV with investigations yielding a half-life of 960 ns [81]. Recently, it has been suggested by Jenkins [103] that the $9/2^+$ isomer is responsible for the non-observation of ^{69}Br in experiments that utilize fusion-evaporation or fragmentation reactions such as those by Pfaff *et al.* [43]. The argument is that in these cases the $9/2^+$ state lies high enough in energy so that it has a lifetime that is short enough so as to decay by proton emission before it can be detected. Jenkins proposed, using the mirrors states in ^{69}Se, taking $Q_p = 850$ keV for the $9/2^+$ so that it would have an estimated half-life of 3 ns. Given the relative separation of the mirror states this places the $3/2^-$ ground state at $Q_p = 276$ keV with an estimated half-life of 233 ms. In this situation no ^{69}Br events would be detected since the proton emission from the $9/2^+$ state has a sufficiently short half-life and the longer lived ground state is not populated due to $9/2^+$ isomer. However, this depends critically on the isomeric ratio, or the amount by which the isomeric state is populated. This ratio is currently not known but would have to be unusually high (near 100 %) in order for this argument to be valid. Emission from the isomeric state is also not supported by a lineshape analysis of the data in this dissertation as shown in Figure 4.16. Although the statistics are low, the low relative energy peak is not as wide as what would be expected for proton decay from a $9/2^+$ nor does the data indicate a significant tail towards low relative energies as expected from the simulation. Lastly, if this peak is the isomeric state, given the spacing between the

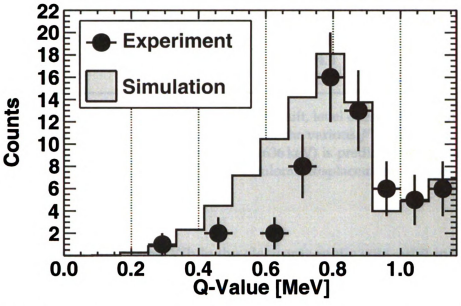

Figure 4.16 – Comparison of simulated decay from a $9/2^+$ ($l = 4$) to the experimental data where the lifetime has been estimated using the WKB approximation. The tail at lower Q-values does not match the data indicating that the decay peak is not due to decays from a long-lived $9/2^+$ state.

$9/2^+$ and the ground state in ^{69}Se of 573.9 keV and assuming mirror symmetry, one would predict that the energy of the ground state in ^{69}Br would be $\sim$ 238 keV. This is a 398 keV disagreement with the value predicted by Savory *et al.* [3] using the measured ^{69}Se mass and the calculated Coulomb displacement energy. This would imply an error in the Coulomb displacement calculation of 398 keV, well outside of the estimated 100 keV uncertainty for such predictions in this mass region.

Finally, there is an additional shift in the Coulomb energy known as the relativistic electromagnetic spin-orbit interaction [12]. In the atom the magnetic field seen by the electron in its orbit through the Coulomb field couples to the electron's magnetic moment. The electron undergoes what is known as Larmor precession in addition to a relativistic interaction that results in Thomas precession. These effects result in the well known spin-orbit interaction in atoms. Analogously, an uncoupled proton or neutron experiences the same effect in the Coulomb field of the nucleus with the main difference being a change in sign of both the Larmor

J^π	Approximate Δ_{so} [keV]	E [keV]	E_x [keV]
$1/2^-$	+74	-710	0
$5/2^-$	+185	-934.4	224.4
$3/2^-$	-37	-801.4	91.4

Table 4.2 – Estimated electromagnetic spin-orbit shift, level energy, and excitation energy assuming a $(1/2^-, 5/2^-, 3/2^-)$ ordering for the various J^π values being considered. The assumed proton separation energy (636 keV) is predicted using the Schury [2] and Savory [3] mass measurements + Coulomb displacement energies of reference [1].

and Thomas interaction terms. While the electromagnetic spin-orbit interaction is typically a very small correction to the Coulomb displacement energy, in certain cases its effect can be significant [104]. From Nolen and Schiffer [12] the shift, Δ_{so}, in the Coulomb displacement energy (in MeV) can be approximated by,

$$\Delta_{so} \simeq 1.2(\mu_p - \frac{1}{2} - \mu_n)\frac{\hbar^2}{2M_p^2c^2}\left(-\frac{Z_< e^2}{{R_C}^3}\right)(\boldsymbol{l}\cdot\boldsymbol{\sigma}) \tag{4.17}$$

$$\simeq -0.15\frac{Z_<}{{R_C}^3}(\boldsymbol{l}\cdot\boldsymbol{\sigma}) \tag{4.18}$$

where,

$$\boldsymbol{l}\cdot\boldsymbol{\sigma} = \begin{cases} l & \text{if } j > l \\ -l-1 & \text{if } j < l \end{cases} \tag{4.19}$$

In Table 4.2 the value of the electromagnetic spin-orbit interaction for the spin-parities of the states being considered as possible ground states in ^{69}Br are given. It is interesting to note that both the $1/2^-$ and $5/2^-$ shifts are quite large and in a direction that would shift the results of the LEBIT+Coulomb displacement energy (CDE) predictions in better agreement with our measured proton separation energy. Moreover, while the $3/2^-$ state was taken as the ground state spin-parity in

the mirror state analysis of this dissertation the $1/2^-$ has recently been proposed as the actual assignment [81]. Also included in Table 4.2 are level and excitation energies for an assumed $(1/2^-, 5/2^-, 3/2^-)$ level ordering given a $1/2^-$ ground state, the ^{69}Se mass, plus a proton separation energy of 636 keV. This shows that the electromagnetic spin-orbit interaction may have an influence on the proton separation energy and should not be discounted.

4.7 X-Ray Burst Calculations

Investigations into the role that the rp-process plays during a type I X-ray burst have been conducted using computer models. These models vary in their level of sophistication but in general allow one to reproduce the light curve, energy generation, isotopic abundances, as well as other quantities and track them over the duration of the burst. For this dissertation full network calculations are used to explore the possible effects of our recently measured ^{68}Se(p,γ)^{69}Br Q-value. Note, that in this section our discussion will involve proton capture Q-values as opposed to the proton separation energy, S_p, where $Q_{p,\gamma} = S_p$.

In this section we consider models designed to simulate the conditions of an X-ray burst occurring on the surface of a neutron star. This scenario (as was discussed in Section 1.3) occurs when hydrogen and helium rich material is transferred to the neutron star from its binary companion. As this material accretes onto the neutron star surface it is compressed and heated until a critical amount of mass builds and ignites due to a thermal instability. The resulting energy release during the ensuing thermonuclear burning is observed in the form of a large release of X-rays on top of the persistent flux originating from the steady accretion. The light curves of the burst tail are found to be governed by the physics of the rp-process.

In order to describe the full dynamics and microphysics of this complex system sophisticated simulations have been developed. For example, the one-dimensional KEPLER code [105] has been used to investigate the explosive burning occurring

during X-ray bursts [33], X-ray burst oscillations [106], and other complex neutron star processes. In principle, the overall characteristics of the X-ray burst can be influenced by the properties of the neutron star at various depths below the surface. In addition, the accretion rate [26] and composition of the accreted matter [32] also play a key role. To handle these effects, codes such as KEPLER break up the surface layers of the neutron star into zones, where the one-dimensional coordinate is the Lagrangian mass (as opposed to length). Each zone is filled with a fixed amount of mass with all zones being tracked during the calculation. These are typically referred to as *multi-zone* models. However, these models are computationally intensive and unnecessary for most studies that only desire to understand relative sensitivities or qualitative effects of the nucleosynthesis. Less complex *one-zone* models have been developed that include most of the key physics needed to test the dependencies and sensitivities of the nuclear physics inputs. These codes do not require large scale computer hardware and typically require less computing power compared to codes such as KEPLER.

The one-zone model by Schatz *et al.* [31] was chosen to investigate, using properly calibrated initial conditions, a long duration X-ray burst. This burst is capable of reaching and processing material up to and beyond the ^{68}Se waiting point. The initial conditions of the burst assume a metallicity of $Z = 10^{-3}$, an accretion rate onto the surface of 0.1 of the Eddington limit, and a flux from the crustal interior of 0.15 MeV accreted nucleon. The total amount of accreted material onto the neutron star surface is 4.7×10^{21} g. In all simulations processing occurs on burst timescales of the order ~ 100 s. Finally, all reaction rates are taken from the recent JINA Reaclib Database* V1.0 [107].

* `http://groups.nscl.msu.edu/jina/reaclib/db/`

4.7.1 No 2p-Capture ($Q(\mathrm{p},\gamma) = -2000\,\mathrm{keV}$)

First, the ^{68}Se(p,γ) Q-value is set to -2000 keV and the reverse reaction rate adjusted accordingly thereby effectively removing the ^{68}Se(2p,γ)^{70}Kr reaction from the rp-process network. Figure 4.17 shows the luminosity, nuclear energy generation, and selected abundance curves for the duration of the burst. At ignition, the density is $\sim 10^6\,\mathrm{g/cm^3}$, and the ignition of helium drives a rapid increase in the luminosity with a risetime of ~ 1 s. The burst reaches a peak temperature of 1.9 GK before it begins to cool. Over the last ~ 200 s the single zone surface layer that was ignited continues to drive the burst at longer times. This is observed as a tail in the luminosity curve, reflecting the burning of the heaviest masses as is observed in the abundance curves. In addition, it is clear that a significant fraction of the processed material ends up in the waiting point nuclei. The relative abundances of both ^{64}Ge and ^{68}Se are large in comparison to the other isotopes that are produced.

Furthermore, as ^{69}Br is highly unbound in this instance ($S_\mathrm{p} = -2000$ keV), there are virtually no ^{69}Br nuclei around to undergo proton capture. As a result the abundance of ^{70}Kr is near zero. In addition, the percentage integrated reaction flow to ^{70}Kr relative to the flow into ^{68}Se is found to be only 2×10^{-6} %.

4.7.2 Non-observation Limit ($Q(\mathrm{p},\gamma) = -500\,\mathrm{keV}$)

For the purposes of comparison the simulation was also run for $Q_{\mathrm{p},\gamma} = -500$ keV with the results shown in Figure 4.18. This corresponds to the non-observation limit set by Pfaff *et al.* [43]. The results are very similar to the previous results discussed in Subsection 4.7.1. However, now a larger abundance of ^{69}Br is produced which is observed to increase the amount of ^{70}Kr, reflecting the larger amount of the reaction flow that bypasses the waiting point via the sequential 2p-capture through ^{69}Br. In this case, it is found that the reaction flow through ^{69}Br to ^{70}Kr is 23 %, relative to the flow into ^{68}Se. The amount of flow through the ^{68}Se in the

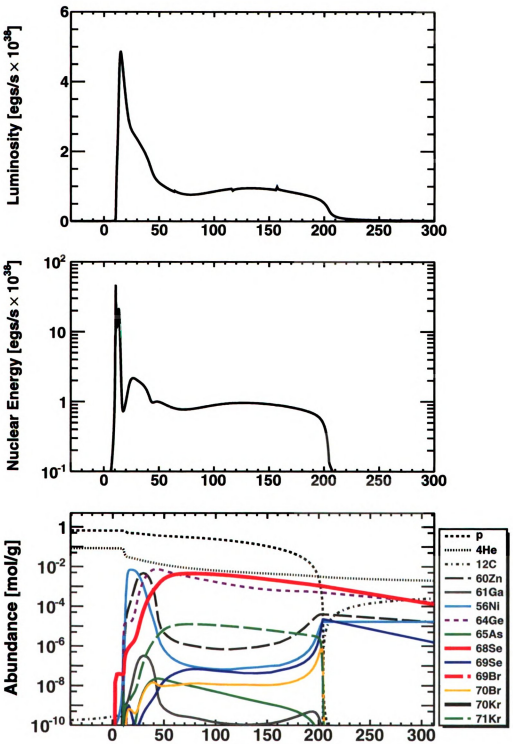

Figure 4.17 – X-ray luminosity, nuclear energy generation, and abundance versus processing time where the 2p-capture on ^{68}Se has been effectively removed from the network calculation. This was accomplished by setting the (p,γ) to a large ($Q_{p,\gamma} = -2000$ keV) value.

present calculation is similar to the results found by Schatz *et al.* [31]. They assumed a ^{68}Se(p,γ) Q-value of -450 keV and found that the flow to ^{70}Kr due to 2p-capture reactions was > 10 %.

4.7.3 Slightly Unbound ($Q(\mathrm{p},\gamma) = -200$ keV)

To exaggerate the influence of ^{69}Br a significantly lower value of $Q_{\mathrm{p},\gamma} = -200$ keV was also chosen. Even though this value is only lowered by 300 keV relative to the previous calculation, the effective half-life of ^{68}Se can be drastically altered by only small changes in Q-value as was demonstrated in Subsection 1.3.1. Indeed, the changes in the abundances and light curves shown in Figure 4.19 illustrate this point. The abundance of ^{69}Br as well as ^{70}Kr has increased by an order of magnitude. This reduces the ^{68}Se abundance through 2p-capture reactions on ^{69}Br, with 30 % of the reaction flow bypassing the waiting-point to ^{70}Kr. In addition the tail in the luminosity curve is shortened by ~ 15 s.

4.7.4 Comparison of Results and Conclusion

In order to investigate the effects of the ^{69}Br proton separation energy found in this dissertation, the simulation is run for $Q_{\mathrm{p},\gamma} = -785$ keV. The luminosity, nuclear energy generation, and abundances are shown in Figure 4.20. The results are almost identical to that of Subsection 4.7.1 with the main exception being an increase in the ^{70}Kr abundance indicating the processing through 2p-captures. However, at $Q_{\mathrm{p},\gamma} = -785$ keV, ^{69}Br is still very unbound as reflected by the lack in its abundance. Furthermore, only 0.16 % of the flow passes through ^{69}Br to ^{70}Kr.

For this choice of X-ray burst initial conditions, lower proton capture Q-values for ^{68}Se tend to reduce the "cooling time" in the tail of the burst. In Figure 4.21 qualitative changes in the luminosity, nuclear energy generation, and temperature due to ^{68}Se(p,γ) Q-value are now more apparent. There is a difference of ~ 15 s between the length of the tail of the light curve for $Q_{\mathrm{p},\gamma} = -200$ keV and $Q_{\mathrm{p},\gamma} =$

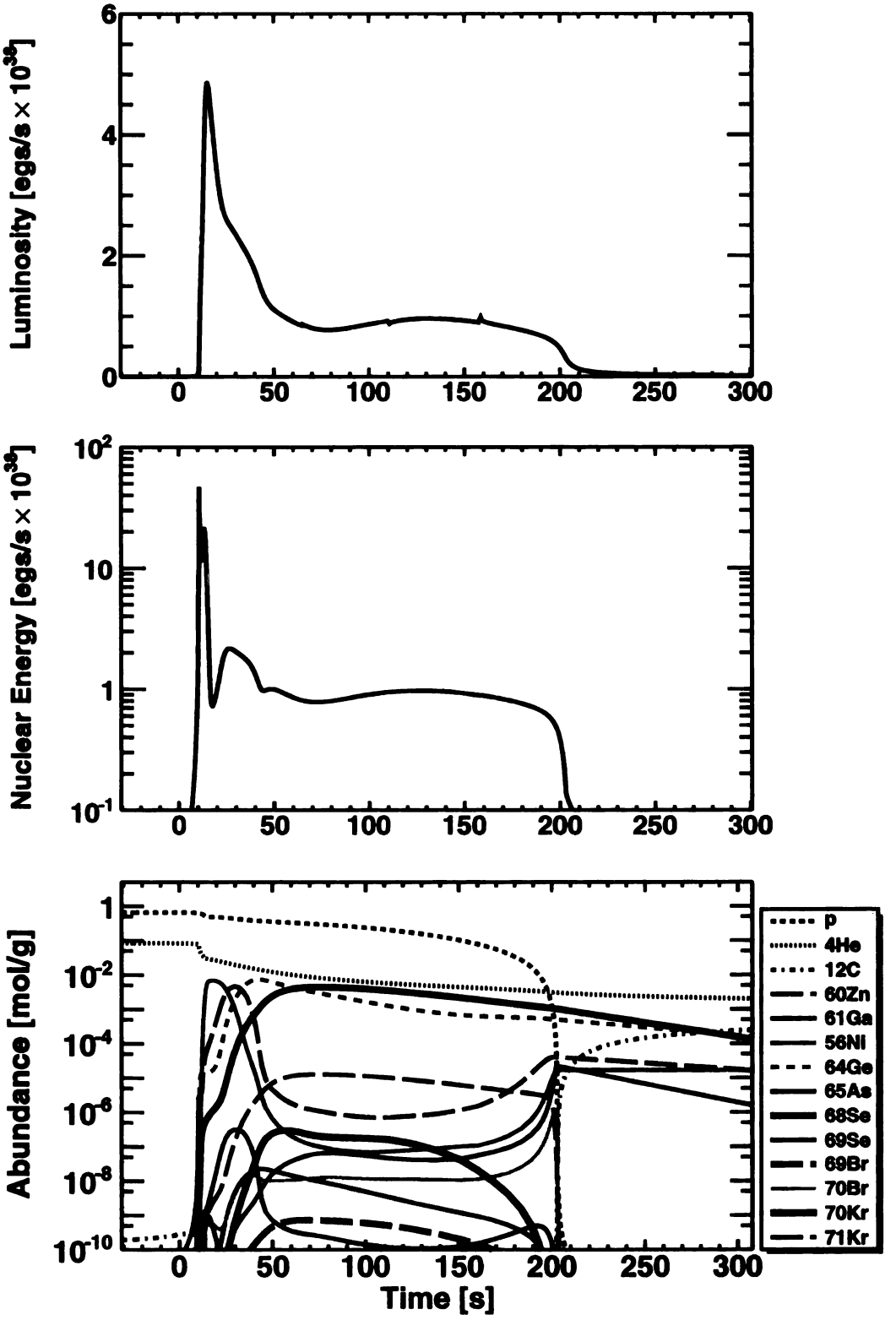

Figure 4.18 – X-ray luminosity, nuclear energy generation, and abundance versus processing time for $Q_{p,\gamma} = -500\,\text{keV}$.

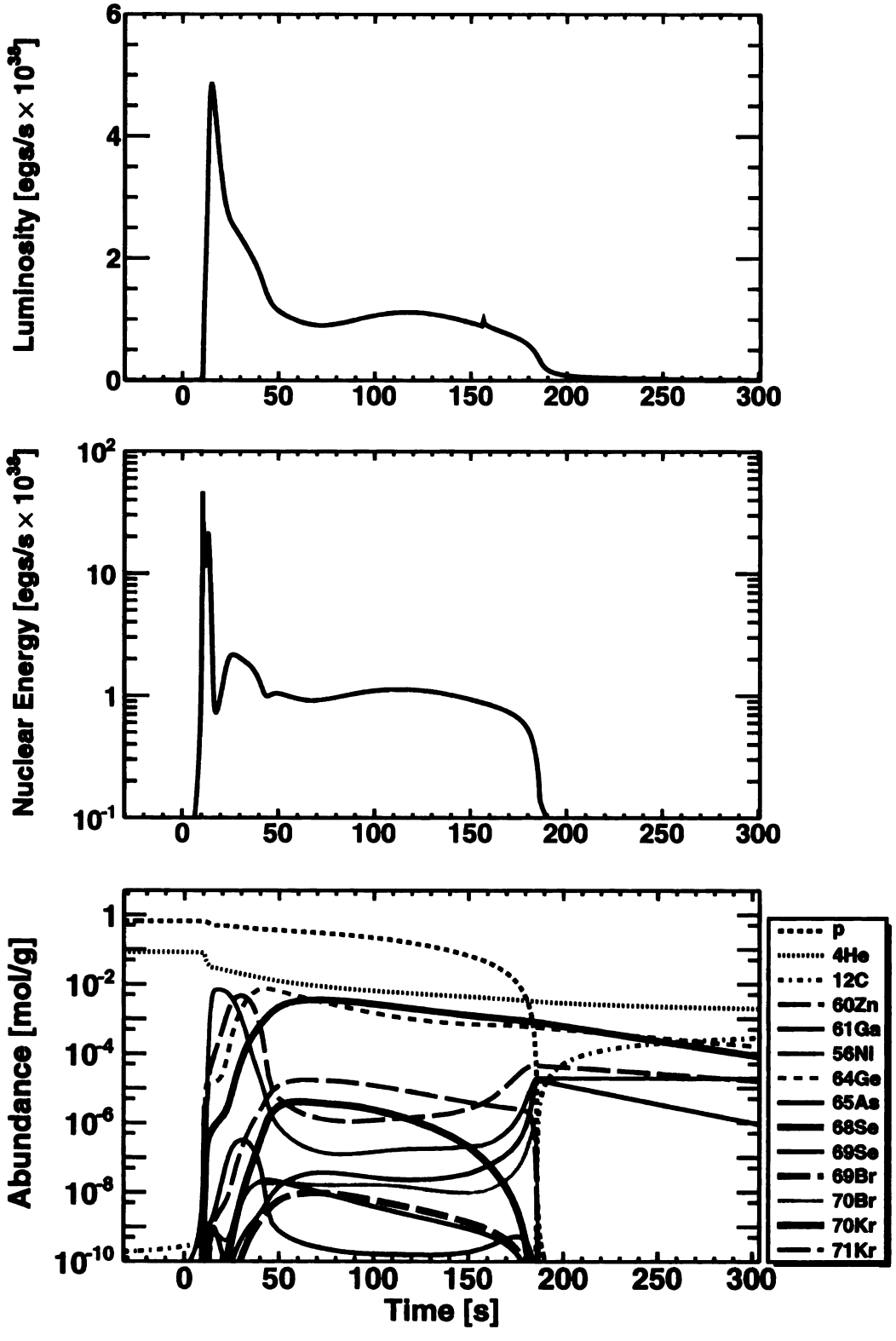

Figure 4.19 – X-ray luminosity, nuclear energy generation, and abundance versus processing time for $Q_{p,\gamma} = -200$ keV.

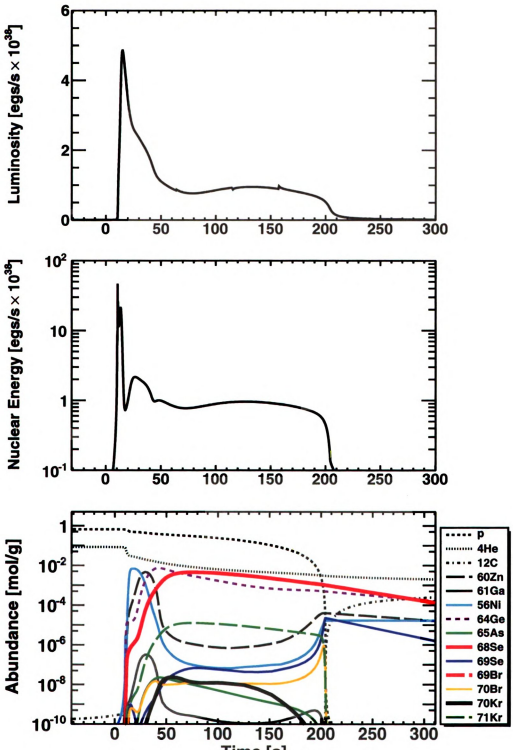

Figure 4.20 – X-ray luminosity, nuclear energy generation, and abundance versus processing time for $Q_{p,\gamma} = -785$ keV.

-785 keV. Furthermore, the luminosity during the middle of the cooling phase is boosted compared to that for $Q_{p,\gamma} = -785$ keV. However, the influence of the 2p-capture branch through ^{69}Br on the luminosity rapidly becomes insignificant as $Q_{p,\gamma}$ becomes more negative since λ_{2p} depends exponentially on $Q_{p,\gamma}$.

Figure 4.23 shows the integrated final abundances for a given mass number at the end of the burst. The effect of the Q-value on the abundance of nuclei beyond ^{68}Se is clearer in Figure 4.23 where the difference between the final abundance for $Q_{p,\gamma} = -785$ keV and the final abundance for $Q_{p,\gamma} = -500$ keV is shown. Here, the increase in the final abundances for $A = 68$ and $A = 72$ masses due to the ^{68}Se and ^{72}Kr waiting-points is evident. Also, a reduction in the synthesis of elements beyond mass 90 is observed although the longer processing time for $Q_{p,\gamma} = -785$ keV allows the flow to build at $A = 106$. These differences amount to corrections to the final abundances at the percent level.

For the initial conditions in this X-ray burst simulation and the proton separation energies determined in this dissertation, the sensitivity of the light curves and the abundance distribution to the uncertainties in proton separation energy in our measurement are negligible. We therefore conclude, that for all practical purposes, one can neglect the 2p-capture through ^{69}Br in calculating the abundances and light curves for this type of X-ray burst.

4.8 Extended Duration X-Ray Burst

To further explore the sensitivities of our measurement a more extreme burst, compared to the simulated burst in the last section, is simulated. A key difference in this X-ray burst is that it occurs over an extended timescale, giving the material more time to undergo processing. The results are organized in the same manner as the results of the burst discussed in the previous section. The X-ray burst luminosity, nuclear energy generation, and abundances are shown for $Q_{p,\gamma} = -2000$, -500, -200, and -785 keV in Figure 4.24, Figure 4.26, Figure 4.18, and Figure 4.27

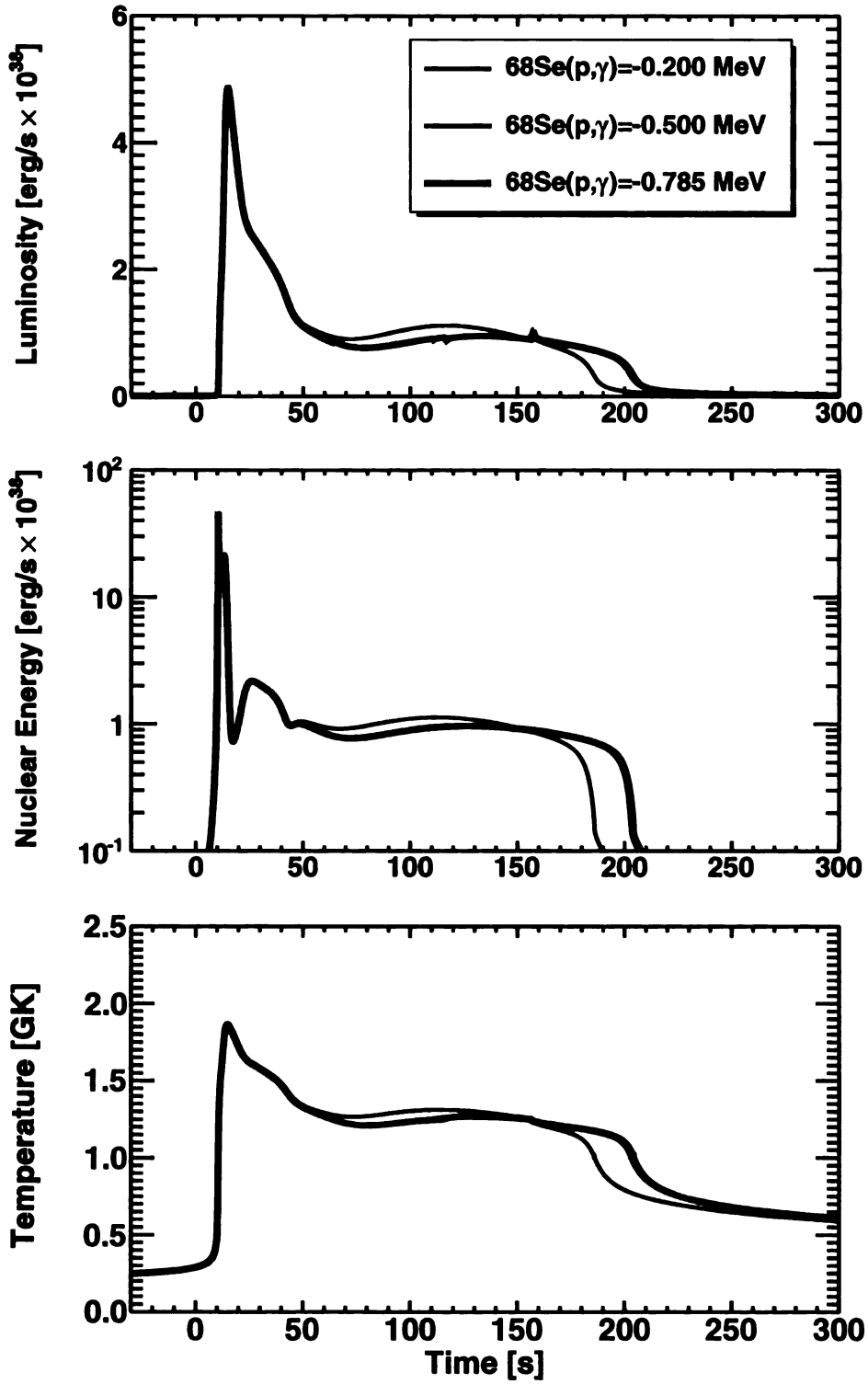

Figure 4.21 – Comparison of the luminosity, nuclear energy generation, and temperature for ^{68}Se(p, γ)^{69}Br Q-values of -200, -500, and -785 keV.

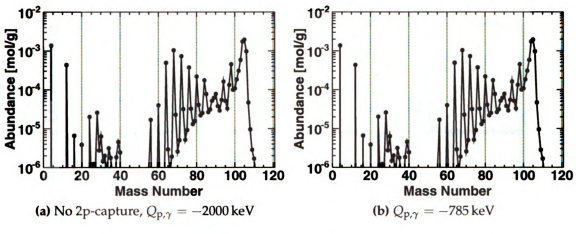

(a) No 2p-capture, $Q_{p,\gamma} = -2000$ keV

(b) $Q_{p,\gamma} = -785$ keV

(c) $Q_{p,\gamma} = -500$ keV

(d) $Q_{p,\gamma} = -200$ keV

Figure 4.22 – Final abundances versus mass number for the Q-values used in the one-zone X-ray burst model. The recommended ^{64}Ge(p, γ) Q-value was used in this calculation.

respectively. Figure 4.28 shows a comparison of the lightcurves for $Q_{p,\gamma}$ =−200, −500, and −785 keV. Finally, the difference between final abundances for $Q_{p,\gamma}$ = −500 keV and $Q_{p,\gamma} = -785$ keV is shown in Figure 4.29.

The burst has many similarities to the first burst we considered. While the burst continues twice as long ($\sim$ 400 s) as the shorter burst of the last section the evolution of the abundance curves is roughly the same, just carried out for a longer time. However, the lightcurves are observed to be even less sensitive to changes in the Q-value compared to the shorter burst. The reaction flows through ^{69}Br to ^{70}Kr for $Q_{p,\gamma}$ =−2000, −500, −200, and −785keV are 8.4×10^{-5} %, 10 %, 33 %, and 0.8 %

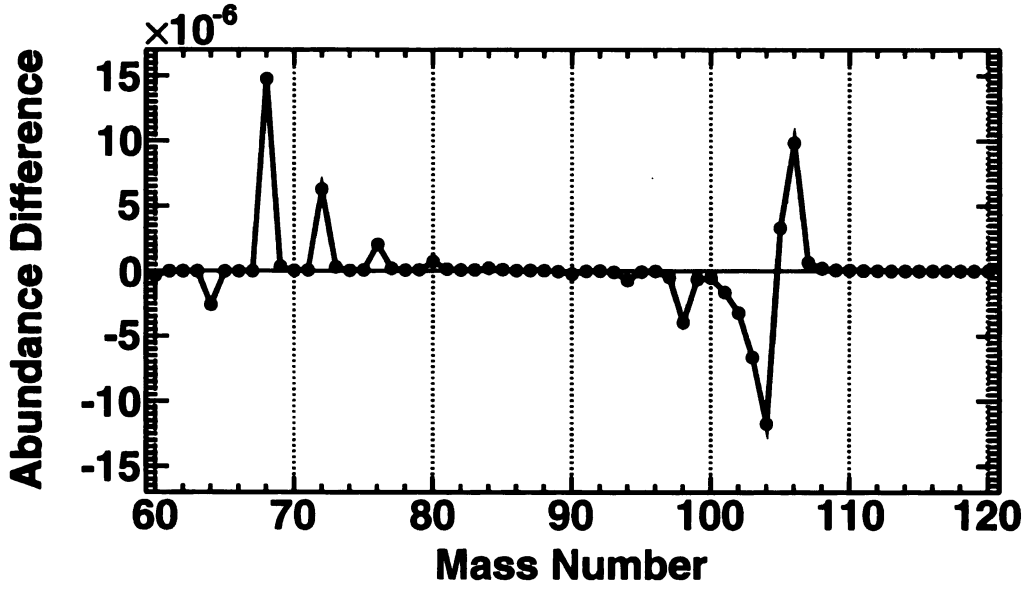

Figure 4.23 – Difference between the final abundances for $Q_{p,\gamma} = -785\,\text{keV}$ and $Q_{p,\gamma} = -500\,\text{keV}$.

respectively, again mirroring the order of magnitude of the reaction flow values from the burst in the previous section. Given the similarities, we conclude that the X-ray burst is again insensitive the 2p-capture branch through ^{69}Br for this second set of conditions.

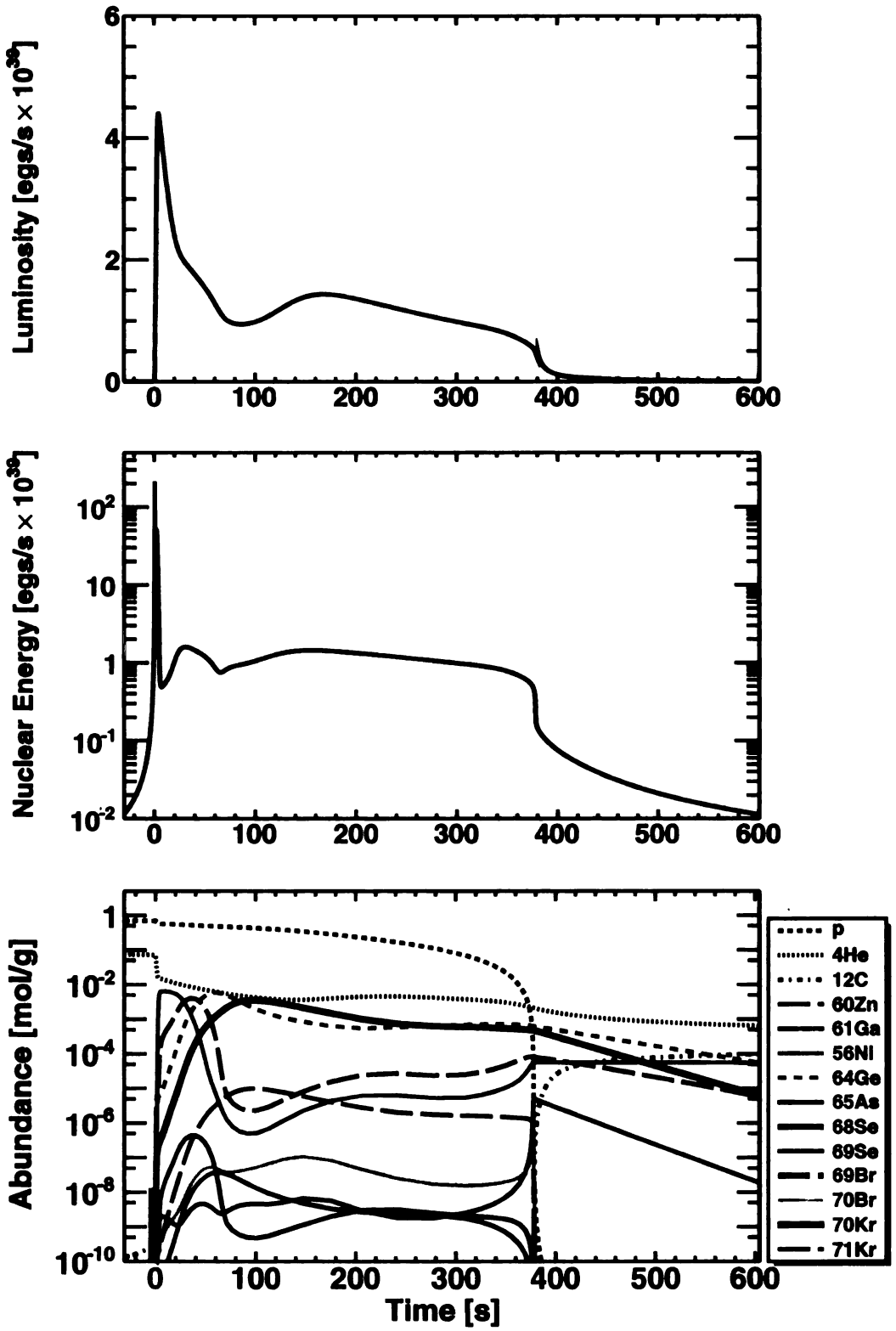

Figure 4.24 – X-ray luminosity, nuclear energy generation, and abundance versus processing time for $Q_{p,\gamma} = -2000$ keV for the extended duration burst.

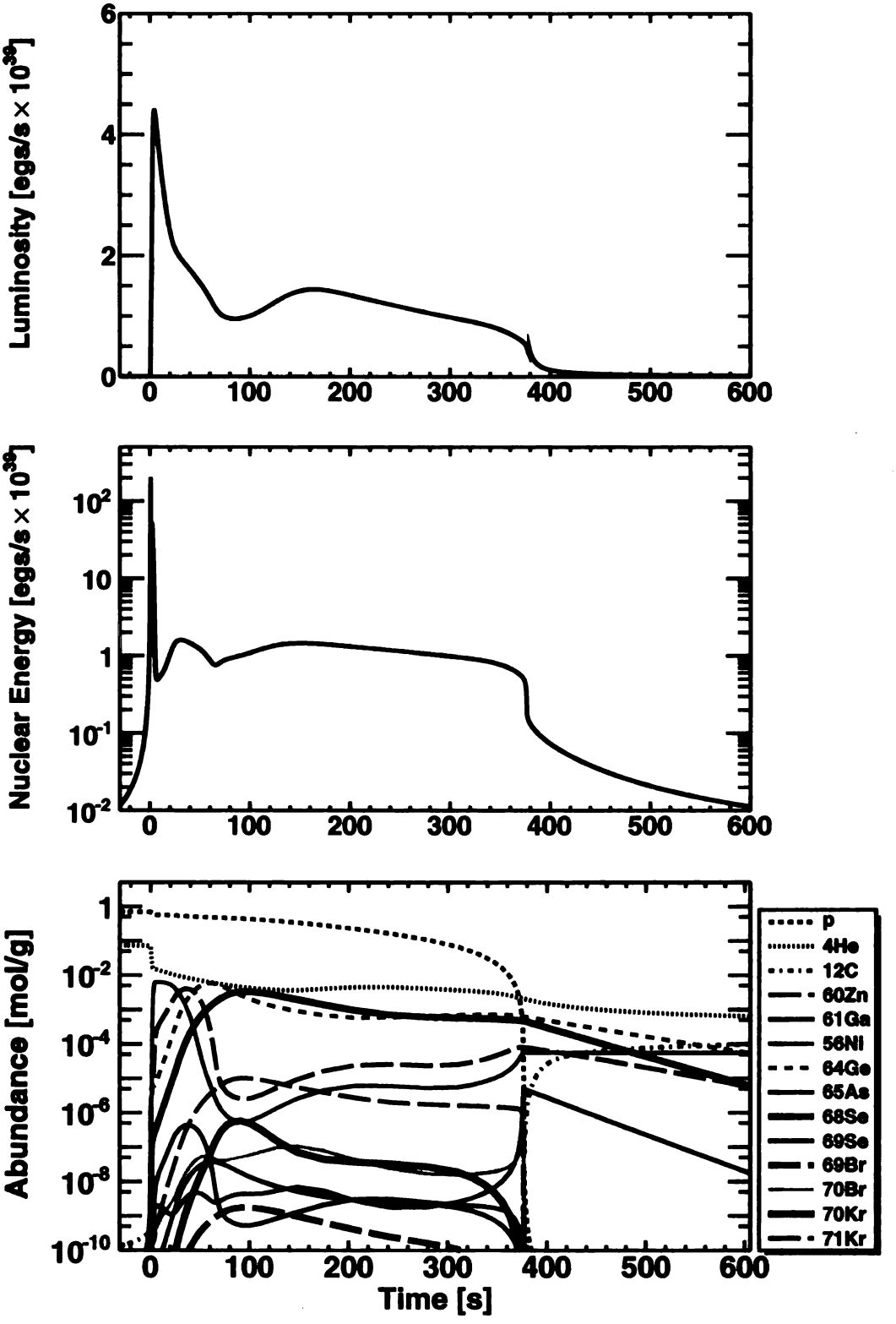

Figure 4.25 – X-ray luminosity, nuclear energy generation, and abundance versus processing time for $Q_{p,\gamma} = -500$ keV for the extended duration burst.

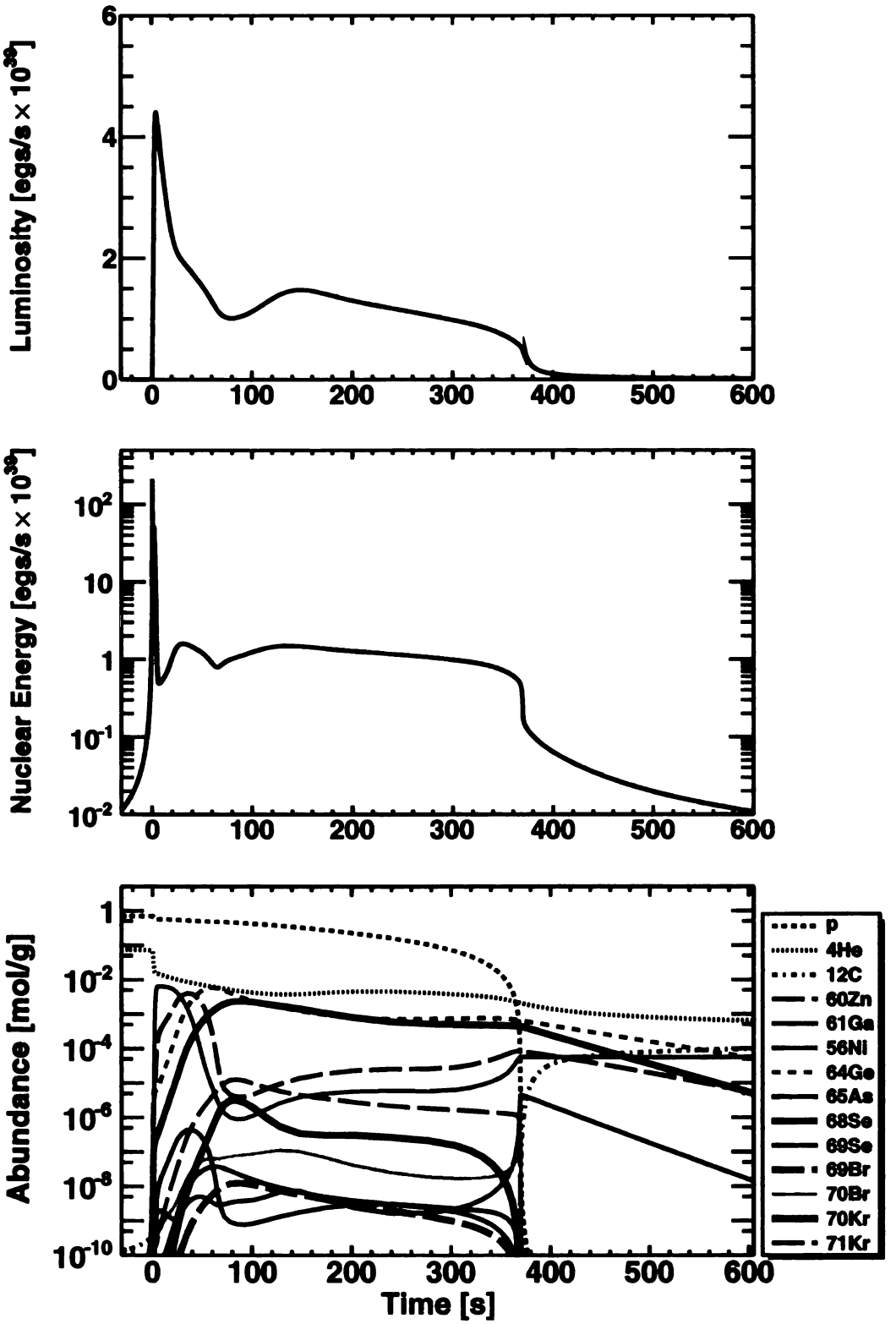

Figure 4.26 – X-ray luminosity, nuclear energy generation, and abundance versus processing time for $Q_{p,\gamma} = -200$ keV for the extended duration burst.

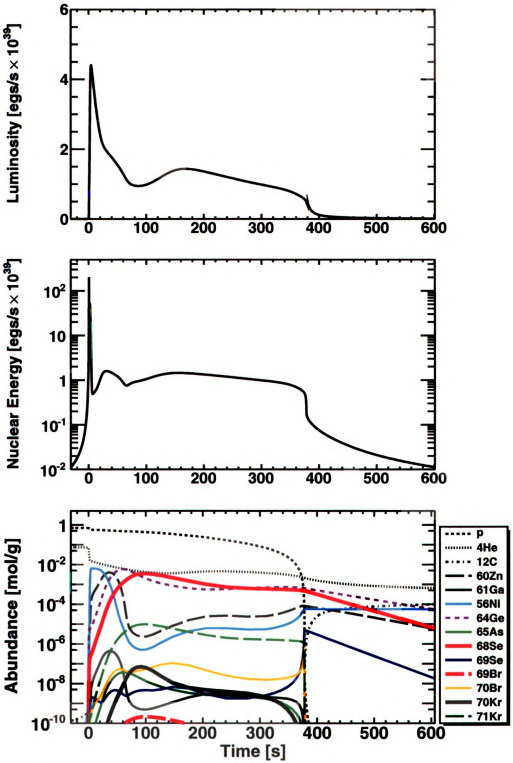

Figure 4.27 – X-ray luminosity, nuclear energy generation, and abundance versus processing time for $Q_{p,\gamma} = -785$ keV for the extended duration burst.

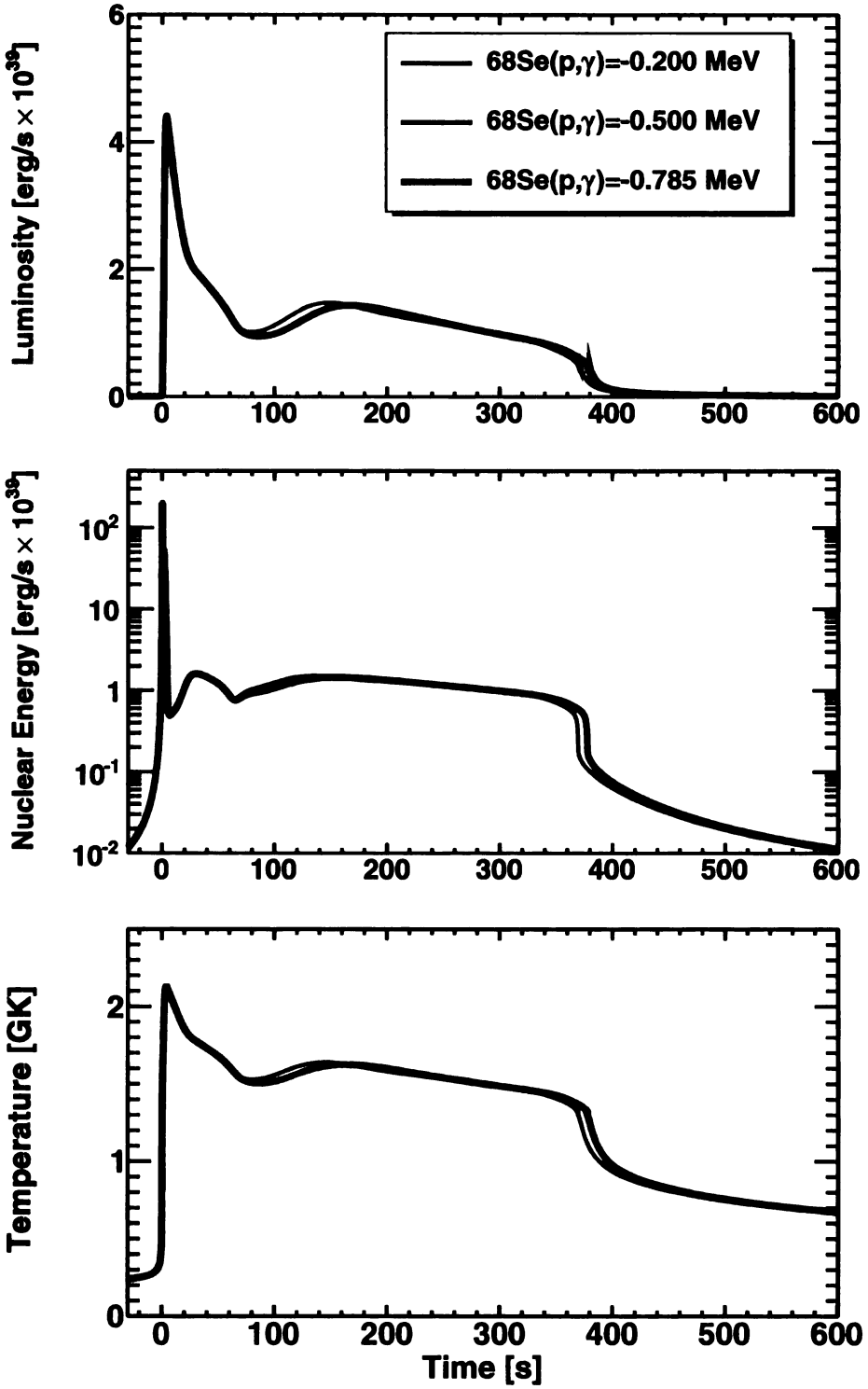

Figure 4.28 – Comparison of the luminosity, nuclear energy generation, and temperature for ^{68}Se(p, γ)^{69}Br Q-values of -200, -500, and -785 keV for the extended duration burst.

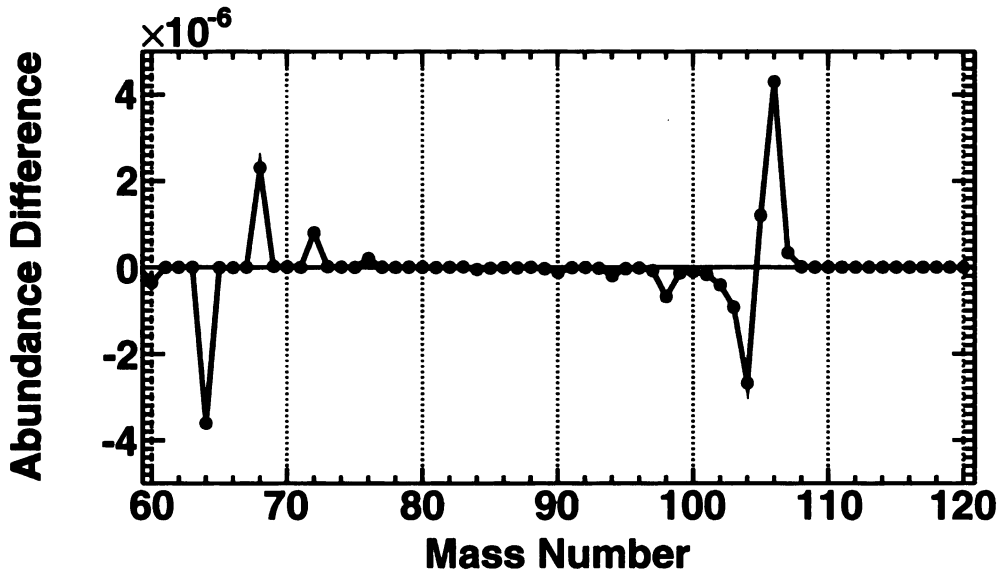

Figure 4.29 – Difference between the final abundances for $Q_{p,\gamma} = -785\,\text{keV}$ and $Q_{p,\gamma} = -500\,\text{keV}$ for the extended duration burst.

Chapter 5

Summary

The need for precise experimental data on nuclei at the proton drip-line is paramount if one is to understand and model the rp-process and the sites, such as Type I X-ray bursts, where it is thought to occur. Sparse data exists for many of the nuclei along the proton drip-line. These nuclei are challenging to measure due to their low production cross-sections and short lifetimes. This is especially the case for the proton unbound nucleus ^{69}Br as is evident from the numerous previous studies that have been done over the past 20 years. However, despite the challenges, these studies have been motivated by the importance of contraining the uncertainties in the rp-process ^{68}Se waiting-point.

As was shown in chapter 1, it is possible to bypass this waiting-point through sequential 2p-capture through ^{69}Br to ^{70}Kr. The reaction rate, however, depends exponentially on the proton separation energy of ^{69}Br. Prior to this disertation, the uncertainty is determined almost completely by the theoretical uncertainties in the Coulomb displacement energy (CDE) of 100 keV.

We performed an experiment to measure directly, via a full kinematic reconstruction method, the proton separation energy of ^{69}Br in order to reduce the uncertainty in the rp-process ^{68}Se waiting-point. This experiment, described in this dissertation, is the first to utilize the High Resolution Array (HiRA) as well as our MCP tracking system. The observed relative energy spectrum shown in Figure 3.45 for ^{69}Br proton decay events shows evidence of a clear decay peak at low relative energies which come from low-lying states in ^{69}Br.

5.1 Results

A number of ^{69}Br proton separation energies are possible depending on assumptions about the level structure. Assuming the structure of ^{69}Br has the same ordering of levels in ^{69}Se, we deduce a value of $S_p = 785^{+34}_{-40}$ keV for the proton separation energy. If one allows for other possible orderings of levels, the separation energy could differ mainly because of the possible distortion coming from long lived states. In the other likely scenerio, we obtain $S_p = 735^{+58}_{-72}$ keV if one allows the $5/2^+$ level to be the ground state.

The effects of the new results reported in this dissertation on the rp-process were investigated using a one-zone X-ray burst code using initial conditions provided by Schatz *et al.* The differences between the two assumptions about level ordering has little effect on the light curves and final abundances produced during the X-ray burst. Moreover, the differences observed for proton separation energies less than the non-observation limit, $S_p < -500$ keV, were not very significant. Additionally, the reaction flow through ^{69}Br to ^{70}Kr, which is 23 % at $S_p = -500$ keV, decreases exponentially to 0.16 % at $S_p = -785$ keV. In conclusion, bypassing ^{68}Se with 2p-captures through ^{69}Br does not appear to be favorable for the type of X-ray burst explored in this dissertation, therefore ^{68}Se should remain a substantial waiting point in the rp-process.

5.2 Outlook

We have explored different initial conditions in the one-zone X-ray burst model to see whether other scenerios may exist where 2p-capture through ^{69}Br might become important. One possible direction to explore would be to have a succession of short X-ray bursts where the seed nuclei from the pervious burst plays a more important role in the energy generation. This may be worth exploring in the future.

This dissertation was successful at measuring the proton separation energy for ^{69}Br. If an improved value for the ^{69}Br proton separation energy is needed or if the present techniques could be useful for other proton unbound nuclei, the statistics and setup could be improved. First of all, the reduced data collection time contributed to low statistics in the relative energy spectra. In addition, there were gaps in the angular coverage of HiRA that could be removed by better optimizing the positions of the detectors. The angular coverage was chosen conservatively to minimize the possibility of direct beam hitting the HiRA detectors. Later, it became clear that one could place detectors safely at smaller angles relative to the beam. If the telescopes could be placed closer to the beam, one would have a higher efficiency for the lowest energy decay protons that are detected. With both a longer data collection time and a reconfiguration of the detector positions, one could probably increase the statistics by a factor of 5-10.

5.2.1 The Influence of the ^{64}Ge Waiting-Point

While this dissertation focused exclusively on the ^{68}Se waiting-point there are other influential nuclei along the rp-process path. In particular, the ^{64}Ge waiting-point is also poorly constrained and determines the reaction flow into the ^{68}Se region. To explore the effects of this waiting-point the (p, γ) Q-value for the ^{64}Ge waiting point was varied within its current uncertainty using the first set of initial conditions from Section 4.7 in order to test its influence on the rp-process within the model. As before, we only use the Q-value of $Q_{p,\gamma} = -785\,\mathrm{keV}$ found in Section 4.5 as the experimental value in this evaluation.

The effects on the X-ray burst are illustrated in Figure 5.1 where the luminosity, nuclear energy generation, and temperature curves are shown for the various ^{68}Se(p, γ) Q-values at two extremes of the ^{64}Ge waiting point proton capture Q-values. For this choice of X-ray burst initial conditions, lower Q-values for the ^{64}Ge

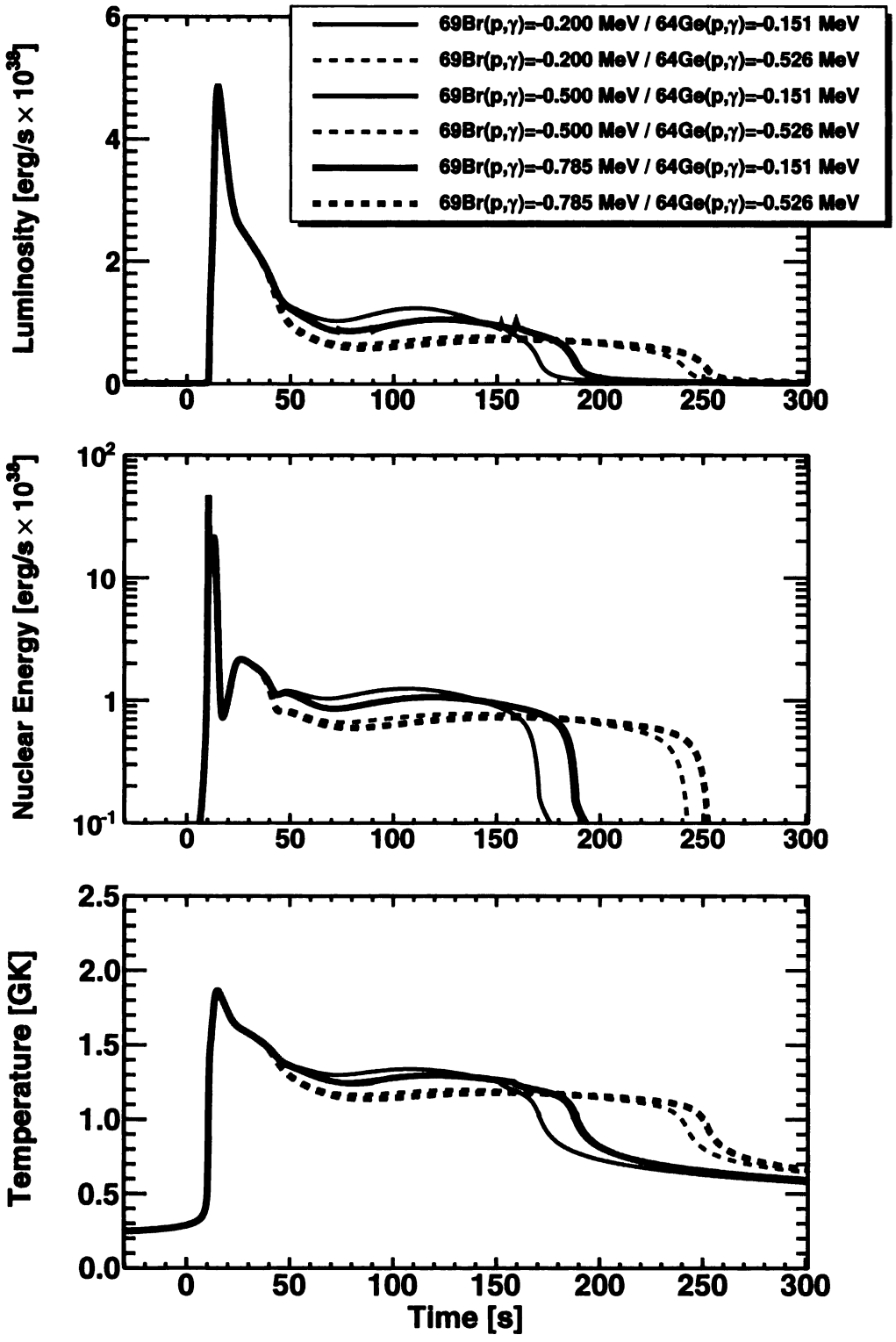

Figure 5.1 – Comparison of the luminosity, nuclear energy generation, and temperature for ^{68}Se(p,γ)^{69}Br Q-values of -200, -500, and -785 keV at high and low ^{64}Ge(p,γ)^{65}As Q-values corresponding to the current uncertainty in the waiting point.

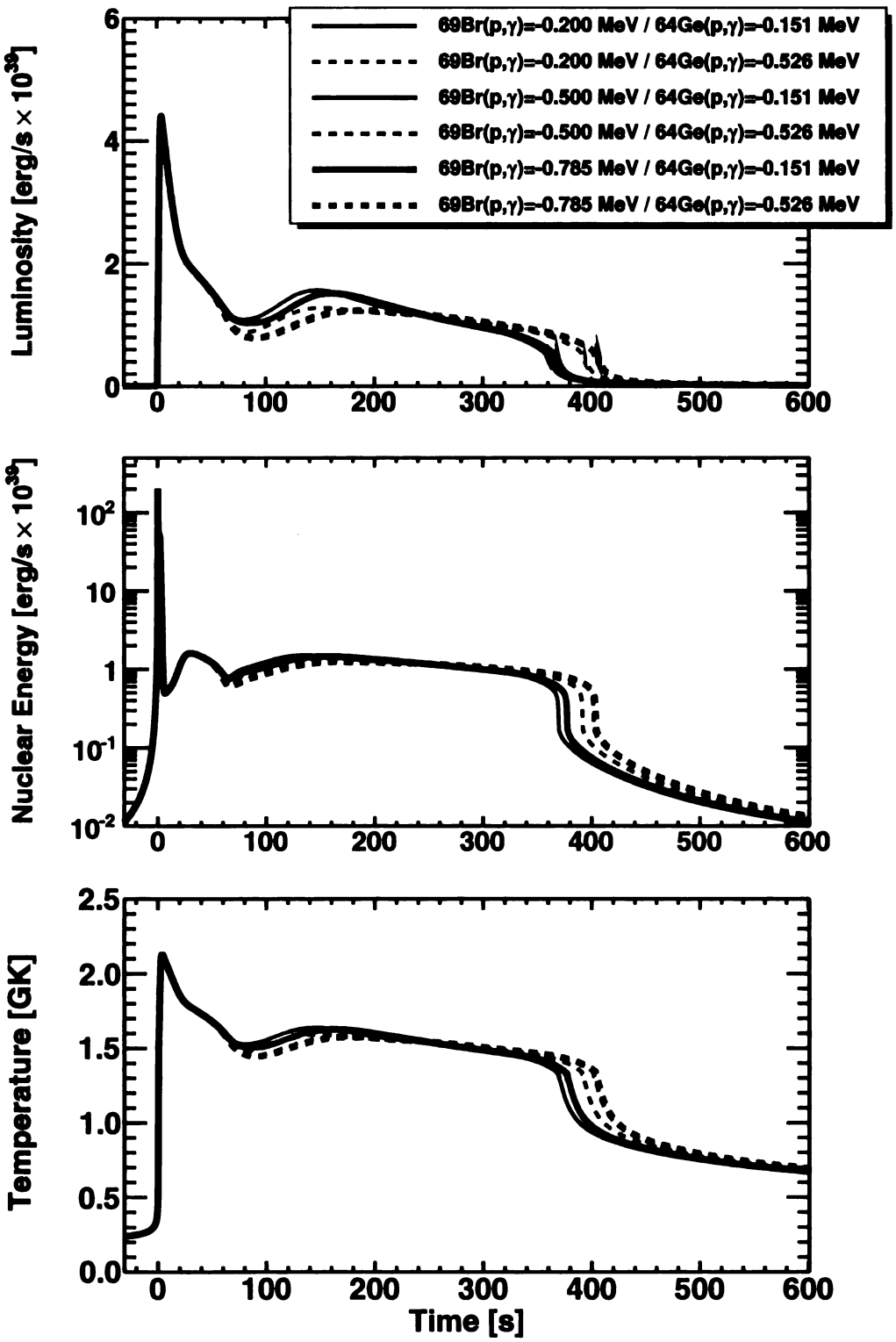

Figure 5.2 – Comparison of the luminosity, nuclear energy generation, and temperature for ^{68}Se(p, γ)^{69}Br Q-values of -200, -500, and -785 keV for the extended burst.

waiting-point tend to reduce the "cooling time" in the tail of the burst. Indeed, it is clear from the X-ray burst calculations that one of the major uncertainties in the rp-process lies with the ^{64}Ge waiting point. Small variations in the ^{65}As proton separation energy have pronounced effects of the light curve of the X-ray burst. The uncertainties in the ^{65}As proton separation energy could be reduced, for instance, by measuring the Q-value for the ^{66}As(p, d) reaction using the known mass of ^{66}As.

In addition, for the production of masses with $A > 73$, it may still be insightful to explore the ^{72}Kr waiting point by measuring the proton separation energy of ^{73}Rb. This could be done using the same techniques as used in this dissertation. Therefore, future experiments devoted to these waiting points should be performed to reduce the overall uncertainty in the rp-process in this region and beyond.

Appendices

Chapter A

Kolmogorov-Smirnov Test

The Kolmogorov-Smirnov test (K-S test) is a statistical test that attempts to determine whether a sample comes from a given reference distribution [97]. It is a nonparametric test, meaning it makes no assumption about the underlying probability distribution (i.e. whether the data come from a normal distribution, binomial, log-normal, or etc.). The sample can be compared to either another reference sample (two-sample test) or to a defined probability distribution (one-sample test). In this dissertation the data from the Monte Carlo simulations (see Section 3.1 and Section 4.5) are taken as reference samples. The low relative energy data from Figure 3.45 is compared to these references. The simulated reference data which yields the maximum probability value (p-value) for the statistic test is the best-fit to the data.

The Kolmogorov-Smirnov test is based on the comparison of either the empirical distribution function (EDF) of two datasets or the comparison of the EDF of data to be tested to the cumulative distribution function (CDF) of the reference probability distribution. Given a set of data points, X_i the EDF is given by,

$$F_n(x) = \frac{1}{n}\sum_{i=1}^{n} I_{X_i \leq x} \tag{A.1}$$

where $I_{X_i \leq x}$ is the so-called indicator function,

$$I_{X_i \leq x} = \begin{cases} 1 & \text{if } X_i \leq x, \\ 0 & \text{Otherwise.} \end{cases} \tag{A.2}$$

The EDF is a function that increases by a step of 1/n at each data point in the set since for a given value of x the summation counts the number of data points that are $\leq x$. For example, suppose we have a set of 10 unordered numbers,

$$X_i = \{4, -5, 8, 3, -2, 9, -10, 5, 6, 1\} \tag{A.3}$$

then the EDF for this set, as shown in Figure A.1, is given by,

$$F_{10}(x) = \begin{cases} 0/10 = 0 & \text{for } x < -10 \\ 1/10 = 0.1 & \text{for } -10 \leq x < -5 \\ 2/10 = 0.2 & \text{for } -5 \leq x < -2 \\ 3/10 = 0.3 & \text{for } -2 \leq x < 1 \\ \dots & \dots \\ 10/10 = 1 & \text{for } x \geq 9. \end{cases} \tag{A.4}$$

The Kolmogorov-Smirnov goodness-of-fit statistic for a two-sample test is,

$$D_{m,n} = \sup_x |F_m(x) - F_n(x)| \tag{A.5}$$

where sup denotes the supremum, or maximum value*, of the distance between the two EDF. And similarly, for tests that utilize a CDF, the statistic is,

$$D_m = \sup_x |F_m(x) - F(x)| \tag{A.6}$$

where $F(x)$ is the CDF.

Figure A.2 demonstrates how the Kolmogorov-Smirnov method works. For

* This is true for the sets of real number that we consider although for other sets the supremum is a more general mathematical concept.

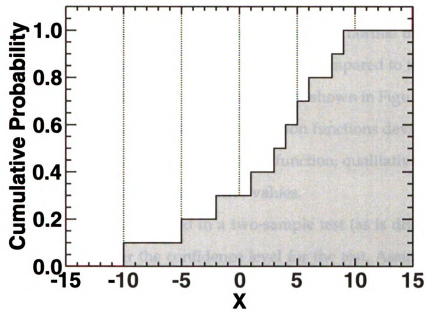

Figure A.1 – Empirical distribution function (EDF) for the example dataset in Equation A.3. The EDF increases by 1/n at each data point in the set.

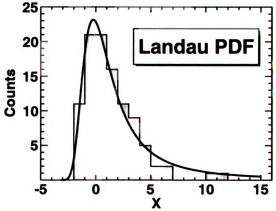

(a) Probability density function for a 100 random samples of a Landau distribution with a mean of 0 and $\sigma = 1$.

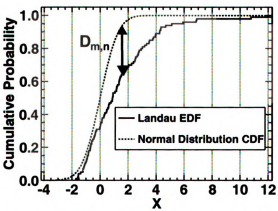

(b) Comparison of the random sample EDF to the CDF for a normal distribution with mean 0 and $\sigma = 1$. The distance, $D_{m,}$ is the test statistic used to quantify if the functions come from the same distribution.

Figure A.2

this example, 100 random points were sampled from a Landau distribution with the resulting probability density function shown in Figure A.2a. Let's suppose we want to test if this set of points has come from a standard normal distribution. In this case, the EDF for the randomly sampled points is compared to the CDF of the normal distribution. The maximum difference, D_m, as shown in Figure A.2b, quantifies their compatibility. Clearly, the two distribution functions deviate from each other for values greater than zero as the Landau function, qualitatively, is less like the standard normal distribution for positive values.

For a given set of data compared in a two-sample test (as is done in this dissertation) one can computer the confidence level for the test. Assuming the null hypothesis, the probability that the Kolmogorov-Smirnov test exceeds the value z, defined by,

$$z = \sqrt{\frac{mn}{m+n}} D_{m,n} \tag{A.7}$$

is,

$$P(z) = 2 \sum_{(i=1)}^{\infty} (-1)^{i-1} e^{-2i^2x^2}. \tag{A.8}$$

Bibliography

Bibliography

[1] B. A. Brown, R. R. C. Clement, H. Schatz, A. Volya, and W. A. Richter. Proton drip-line calculations and the rp process. *Phys. Rev. C*, 65(4):045802, Mar 2002.

[2] P. Schury, C. Bachelet, M. Block, G. Bollen, D. A. Davies, M. Facina, C. M. Folden III, C. Guenaut, J. Huikari, E. Kwan, A. Kwiatkowski, D. J. Morrissey, R. Ringle, G. K. Pang, A. Prinke, J. Savory, H. Schatz, S. Schwarz, C. S. Sumithrarachchi, and T. Sun. Precision mass measurements of rare isotopes near $N = Z = 33$ produced by fast beam fragmentation. *Physical Review C*, 75(5):055801, 2007.

[3] J. Savory, P. Schury, C. Bachelet, M. Block, G. Bollen, M. Facina, C. M. Folden III, C. Guenaut, E. Kwan, A. A. Kwiatkowski, D. J. Morrissey, G. K. Pang, A. Prinke, R. Ringle, H. Schatz, S. Schwarz, and C. S. Sumithrarachchi. rp process and masses of $N \approx Z \approx 34$ nuclides. *Physical Review Letters*, 102(13):132501, 2009.

[4] Michal Mocko. *Rare Isotope Production*. PhD thesis, Michigan State University, 2006.

[5] DN Spergel, R. Bean, O. Dore, MR Nolta, CL Bennett, J. Dunkley, G. Hinshaw, N. Jarosik, E. Komatsu, L. Page, et al. Three-year Wilkinson Microwave Anisotropy Probe (WMAP) observations: implications for cosmology. *The Astrophysical Journal Supplement Series*, 170(2):377–408, 2007.

[6] B.E.J. Pagel. *Nucleosynthesis and Chemical Evolution of Galaxies*. Cambridge University Press, 1997.

[7] E. Margaret Burbidge, G. R. Burbidge, William A. Fowler, and F. Hoyle. Synthesis of the elements in stars. *Rev. Mod. Phys.*, 29(4):547–650, Oct 1957.

[8] Pierrick Martin and Jacco Vink. Linking ^{44}Ti explosive nucleosynthesis to the dynamics of core-collapse supernovae. *New Astronomy Reviews*, 52(7-10):401–404, 2008. Astronomy with Radioactivities. VI - Proceedings of International Workshop Held at Ringberg Castle of Max Planck Gesellschaft in Kreuth, Germany, 7-10 January 2008.

[9] D. Lunney, J. M. Pearson, and C. Thibault. Recent trends in the determination of nuclear masses. *Rev. Mod. Phys.*, 75(3):1021–1082, Aug 2003.

[10] G. Audi, A. H. Wapstra, and C. Thibault. The 2003 atomic mass evaluation: (II). tables, graphs and references. *Nuclear Physics A*, 729(1):337–676, 2003. The 2003 NUBASE and Atomic Mass Evaluations.

[11] DD Warner, MA Bentley, and P. Van Isacker. The role of isospin symmetry in collective nuclear structure. *Nature Physics*, 2(5):311–318, 2006.

[12] J A Nolen and J P Schiffer. Coulomb energies. *Annual Review of Nuclear Science*, 19(1):471–526, 1969.

[13] M.A. Bentley and S.M. Lenzi. Coulomb energy differences between high-spin states in isobaric multiplets. *Progress in Particle and Nuclear Physics*, 59(2):497–561, 2007.

[14] B. Blank. Two-proton radioactivity. *Reports on Progress in Physics*, 71(4):46301–46500, 2008.

[15] VI Goldanskh. Modes of radioactive decay involving proton emission. *Annual review of nuclear science*, 16(1):1–30, 1966.

[16] K.P. Jackson, C.U. Cardinal, H.C. Evans, N.A. Jelley, and J. Cerny. ^{53m}Co: A proton-unstable isomer. *Physics Letters B*, 33(4):281–283, 1970.

[17] O. Klepper, T. Batsch, S. Hofmann, R. Kirchner, W. Kurcewicz, W. Reisdorf, E. Roeckl, D. Schardt, and G. Nyman. Direct and beta-delayed proton decay of very neutron-deficient rare-earth isotopes produced in the reaction ^{58}Ni+^{92}Mo. *Name: Z. Phys. A*, 1982.

[18] S. Hofmann, W. Reisdorf, G. Münzenberg, FP Heßberger, JRH Schneider, and P. Armbruster. Proton radioactivity of ^{151}Lu. *Zeitschrift für Physik A Hadrons and Nuclei*, 305(2):111–123, 1982.

[19] T. Faestermann, A. Gillitzer, K. Hartel, P. Kienle, and E. Nolte. Evidence for proton radioactivity of ^{113}Cs and ^{109}I. *Physics Letters B*, 137(1-2):23 – 26, 1984.

[20] H. Mahmud, C. N. Davids, P. J. Woods, T. Davinson, A. Heinz, G. L. Poli, J. J. Ressler, K. Schmidt, D. Seweryniak, M. B. Smith, A. A. Sonzogni, J. Uusitalo, and W. B. Walters. Proton radioactivity of ^{117}La. *Phys. Rev. C*, 64(3):031303, Aug 2001.

[21] P. J. Woods, P. Munro, D. Seweryniak, C. N. Davids, T. Davinson, A. Heinz, H. Mahmud, F. Sarazin, J. Shergur, W. B. Walters, and A. Woehr. Proton decay of the highly deformed nucleus ^{135}Tb. *Phys. Rev. C*, 69(5):051302, May 2004.

[22] B. Blank and M.J.G. Borge. Nuclear structure at the proton drip line: Advances with nuclear decay studies. *Progress in Particle and Nuclear Physics*, 60(2):403–483, 2008.

[23] B. Buck, A. C. Merchant, and S. M. Perez. Ground state proton emission from heavy nuclei. *Phys. Rev. C*, 45(4):1688–1692, Apr 1992.

[24] Sven Åberg, Paul B. Semmes, and Witold Nazarewicz. Spherical proton emitters. *Phys. Rev. C*, 56(4):1762–1773, Oct 1997.

[25] D.N. Poenaru and M.S. Ivascu. *Particle emission from nuclei*. CRC Press, 1989.

[26] RK Wallace and SE Woosley. Explosive hydrogen burning. *Astrophys. J., Suppl. Ser*, 45(2), 1981.

[27] W.H.G. Lewin and M. van der Klis. *Compact stellar X-ray sources*. Cambridge Univ Press, 2006.

[28] J. Audouze, J.W. Truran, and B.A. Zimmerman. Hot CNO-Ne cycle hydrogen burning. thermonuclear evolution at constant temperature and density. *The Astrophysical Journal*, 184:493, 1973.

[29] R. E. Taam. Nuclear processes at neutron star surfaces. *Annual Review of Nuclear and Particle Science*, 35:1–23, 1985.

[30] S. Wanajo. The rp-process in neutrino-driven winds. *The Astrophysical Journal*, 647(2):1323–1340, 2006.

[31] H. Schatz, A. Aprahamian, J. Gorres, M. Wiescher, T. Rauscher, JF Rembges, F.K. Thielemann, B. Pfeiffer, P. Moller, K.L. Kratz, H. Herndl, B.A. Brown, and H. Rebel. rp-process nucleosynthesis at extreme temperature and density conditions. *Physics reports*, 294(4):167–263, 1998.

[32] Hendrik Schatz, Lars Bildsten, Andrew Cumming, and Michael Wiescher. The rapid proton process ashes from stable nuclear burning on an accreting neutron star. *The Astrophysical Journal*, 524(2):1014–1029, 1999.

[33] SE Woosley, A. Heger, A. Cumming, RD Hoffman, J. Pruet, T. Rauscher, JL Fisker, H. Schatz, BA Brown, and M. Wiescher. Models for type I x-ray bursts with improved nuclear physics. *The Astrophysical Journal Supplement Series*, 151(1):75–102, 2004.

[34] George Wallerstein, Icko Iben, Peter Parker, Ann Merchant Boesgaard, Gerald M. Hale, Arthur E. Champagne, Charles A. Barnes, Franz Käppeler, Verne V. Smith, Robert D. Hoffman, Frank X. Timmes, Chris Sneden, Richard N. Boyd, Bradley S. Meyer, and David L. Lambert. Synthesis of the elements in stars: forty years of progress. *Rev. Mod. Phys.*, 69(4):995, Oct 1997.

[35] H. Schatz, A. Aprahamian, V. Barnard, L. Bildsten, A. Cumming, M. Ouellette, T. Rauscher, F.-K. Thielemann, and M. Wiescher. End point of the rp process on accreting neutron stars. *Phys. Rev. Lett.*, 86(16):3471–3474, Apr 2001.

[36] V.-V. Elomaa, G. K. Vorobjev, A. Kankainen, L. Batist, S. Eliseev, T. Eronen, J. Hakala, A. Jokinen, I. D. Moore, Yu. N. Novikov, H. Penttila, A. Popov, S. Rahaman, J. Rissanen, A. Saastamoinen, H. Schatz, D. M. Seliverstov,

C. Weber, and J. Aysto. Quenching of the SnSbTe cycle in the rp process. *Physical Review Letters*, 102(25):252501, 2009.

[37] A. P. Robinson, C. N. Davids, G. Mukherjee, D. Seweryniak, S. Sinha, P. Wilt, and P. J. Woods. Proton decay study of ^{150}Lu and ^{150m}Lu. *Phys. Rev. C*, 68(5):054301, Nov 2003.

[38] C.-H. Yu, J. C. Batchelder, C. R. Bingham, R. Grzywacz, K. Rykaczewski, K. S. Toth, Y. Akovali, C. Baktash, A. Galindo-Uribarri, T. N. Ginter, C. J. Gross, M. Karny, S. H. Kim, B. D. MacDonald, S. D. Paul, D. C. Radford, J. Szerypo, and W. Weintraub. In-beam spectroscopy study of the proton emitter ^{151}Lu. *Phys. Rev. C*, 58(6):R3042–R3045, Dec 1998.

[39] J. D. Robertson, J. E. Reiff, T. F. Lang, D. M. Moltz, and Joseph Cerny. Search for ground state proton emission from ^{65}As and ^{69}Br. *Phys. Rev. C*, 42(5):1922–1928, Nov 1990.

[40] E. Hourani, F. Azaiez, P. Dessagne, A. Elayi, S. Fortier, S. Gales, JM Maison, P. Massolo, C. Miehe, and A. Richard. Search for proton radioactivity in ^{65}As, ^{69}Br and ^{77}Y. *Zeitschrift für Physik A Hadrons and Nuclei*, 334(3):277–283, 1989.

[41] M. F. Mohar, D. Bazin, W. Benenson, D. J. Morrissey, N. A. Orr, B. M. Sherrill, D. Swan, J. A. Winger, A. C. Mueller, and D. Guillemaud-Mueller. Identification of new nuclei near the proton-drip line for $31 \leq Z \leq 38$. *Phys. Rev. Lett.*, 66(12):1571–1574, Mar 1991.

[42] B. Blank, S. Andriamonje, S. Czajkowski, F. Davi, R. Del Moral, J. P. Dufour, A. Fleury, A. Musquère, M. S. Pravikoff, R. Grzywacz, Z. Janas, M. Pfützner, A. Grewe, A. Heinz, A. Junghans, M. Lewitowicz, J.-E. Sauvestre, and C. Donzaud. New isotopes from ^{78}Kr fragmentation and the ending point of the astrophysical rapid-proton-capture process. *Phys. Rev. Lett.*, 74(23):4611–4614, Jun 1995.

[43] R. Pfaff, D. J. Morrissey, W. Benenson, M. Fauerbach, M. Hellström, C. F. Powell, B. M. Sherrill, M. Steiner, and J. A. Winger. Fragmentation of ^{78}Kr projectiles. *Phys. Rev. C*, 53(4):1753–1758, Apr 1996.

[44] A. S. Lalleman, G. Auger, W. Mittig, M. Chabert, M. Chartier, J. Fermé, A. Gillibert, A. Lépine-Szily, M. Lewitowicz, M. H. Moscatello, N. A. Orr, G. Politi, F. Sarazin, H. Savajols, P. Van Isacker, and A. C. C. Villari. Mass measurements of exotic nuclei around $N = Z = 40$ with CSS2. *Hyperfine Interactions*, 132(1):313–320, 2001.

[45] G. F. Lima, A. Lépine-Szily, G. Audi, W. Mittig, M. Chartier, N. A. Orr, R. Lichtenthaler, J. C. Angelique, J. M. Casandjian, A. Cunsolo, C. Donzaud,

A. Foti, A. Gillibert, M. Lewitowicz, S. Lukyanov, M. MacCormick, D. J. Morrissey, A. N. Ostrowski, B. M. Sherrill, C. Stephan, T. Suomijarvi, L. Tassan-Got, D. J. Vieira, A. C. C. Villari, and J. M. Wouters. Direct mass measurements of proton-rich isotopes of Ge, As, Se, and Br. *Phys. Rev. C*, 65(4):044618, Apr 2002.

[46] J. A. Clark, G. Savard, K. S. Sharma, J. Vaz, J. C. Wang, Z. Zhou, A. Heinz, B. Blank, F. Buchinger, J. E. Crawford, S. Gulick, J. K. P. Lee, A. F. Levand, D. Seweryniak, G. D. Sprouse, and W. Trimble. Precise mass measurement of ^{68}Se, a waiting-point nuclide along the rp process. *Phys. Rev. Lett.*, 92(19):192501, May 2004.

[47] G. Audi and A. H. Wapstra. The 1995 update to the atomic mass evaluation. *Nuclear Physics A*, 595(4):409–480, 1995.

[48] G. Audi, O. Bersillon, J. Blachot, and A. H. Wapstra. The Nubase evaluation of nuclear and decay properties. *Nuclear Physics A*, 624(1):1–124, 1997.

[49] A. H. Wapstra, G. Audi, and C. Thibault. The 2003 atomic mass evaluation: (I). evaluation of input data, adjustment procedures. *Nuclear Physics A*, 729(1):129–336, 2003. The 2003 NUBASE and Atomic Mass Evaluations.

[50] Peter Möller, J. Rayford Nix, William D. Myers, and Wladyslaw J. Swiatecki. The coulomb redistribution energy as revealed by a refined study of nuclear masses. *Nuclear Physics A*, 536(1):61–71, 1992.

[51] P. Moller, J. R. Nix, W. D. Myers, and W. J. Swiatecki. Nuclear ground-state masses and deformations. *Atomic Data and Nuclear Data Tables*, 59(2):185–381, 1995.

[52] W. E. Ormand. Mapping the proton drip line up to $A = 70$. *Phys. Rev. C*, 55(5):2407–2417, May 1997.

[53] A. Wöhr, A. Aprahamian, P. Boutachkov, J.L. Galache, J. Görres, M. Shawcross, A. Teymurazyan, M.C. Wiescher, D.S. Brenner, C.N. Davids, S.M. Fischer, A.M. Heinz, R.V.F. Janssens, and D. Seweryniak. The $N = Z$ rp-process waiting-point nucleus ^{68}Se and its astrophysical implications. *Nuclear Physics A*, 742(3-4):349–362, 2004.

[54] F. Marti, P. Miller, D. Poe, M. Steiner, J. Stetson, and XY Wu. Commissioning of the coupled cyclotron system at NSCL. *AIP CONFERENCE PROCEEDINGS*, pages 64–68, 2001.

[55] DJ Morrissey and N. Staff. A new high-resolution separator for high-intensity secondary beams. *Nuclear Instruments and Methods in Physics Research B*, 126:316–319, 1997.

[56] DJ Morrissey, BM Sherrill, M. Steiner, A. Stolz, and I. Wiedenhoever. Commissioning the A1900 projectile fragment separator. *Nuclear Instruments and Methods in Physics Research B*, 204:90–96, 2003.

[57] J. Yurkon, D. Bazin, W. Benenson, DJ Morrissey, BM Sherrill, D. Swan, and R. Swanson. Focal plane detector for the S800 high-resolution spectrometer. *Nuclear Instruments and Methods in Physics Research Section A: Accelerators, Spectrometers, Detectors and Associated Equipment*, 422(1):291–295, 1999.

[58] D. Bazin, JA Caggiano, BM Sherrill, J. Yurkon, and A. Zeller. The S800 spectrograph. *Nuclear Instruments and Methods in Physics Research B*, 204:629–633, 2003.

[59] Th. G. Brown, K. Creath, H. Krogenlnik, M.A. Kriss, J. Schmit, and M.J. Weber, editors. *The Optics Encyclopedia*, volume 1. Wiley-VCH, 2004.

[60] M. Berz, K. Joh, J. A. Nolen, B. M. Sherrill, and A. F. Zeller. Reconstructive correction of aberrations in nuclear particle spectrographs. *Phys. Rev. C*, 47(2):537–544, Feb 1993.

[61] Joseph Caggiano. *Spectroscopy of Exotic Nuclei with the S800 Spectrograph.* PhD thesis, Michigan State University, 1999.

[62] SR Klein, P. Barale, E. Beuville, F. Bieser, K. Dao, S. Kleinfelder, V. Lindenstruth, MA Lisa, C. McParland, T. Noggle, et al. Front end electronics for the STAR TPC. *IEEE Transactions on Nuclear Science*, 43(3 Part 2):1768–1772, 1996.

[63] J. Adams and B.W. Manley. The mechanism of channel electron multiplication. *IEEE Transactions on Nuclear Science*, NS-13:88, June 1966.

[64] Joseph Ladislas Wiza. Microchannel plate detectors. *Nuclear Instruments and Methods*, 162(1-3):587–601, 1979.

[65] E. C. Pollacco, J. C. Jacmart, Y. Blumenfeld, Ph. Chomaz, N. Frascaria, J. P. Garron, and J. C. Roynette. A compact gridless channel plate detector for time-of-flight measurements. *Nuclear Instruments and Methods in Physics Research*, 225(1):51–56, 1984.

[66] O. H. Odland, W. Mittig, A. Lépine-Szily, G. Fremont, M. Chartier, M. MacCormick, and J. M. Casandjian. A fast position sensitive microchannel plate detector for ray-tracing of charged particles. *Nuclear Instruments and Methods in Physics Research Section A: Accelerators, Spectrometers, Detectors and Associated Equipment*, 378(1-2):149–154, 1996.

[67] J. L. Culhane. Position sensitive detectors in x-ray astronomy. *Nuclear Instruments and Methods in Physics Research Section A: Accelerators, Spectrometers, Detectors and Associated Equipment*, 310(1-2):1–13, 1991.

[68] D. Shapira, T. A. Lewis, and L. D. Hulett. A fast and accurate position-sensitive timing detector based on secondary electron emission. *Nuclear Instruments and Methods in Physics Research Section A: Accelerators, Spectrometers, Detectors and Associated Equipment*, 454(2-3):409–420, 2000.

[69] D. Shapira, T. A. Lewis, L. D. Hulett, and Z. Ciao. Factors affecting the performance of detectors that use secondary electron emission from a thin foil to determine ion impact position. *Nuclear Instruments and Methods in Physics Research Section A: Accelerators, Spectrometers, Detectors and Associated Equipment*, 449(1-2):396–407, 2000.

[70] MS Wallace, MA Famiano, M.J. van Goethem, AM Rogers, WG Lynch, J. Clifford, F. Delaunay, J. Lee, S. Labostov, M. Mocko, et al. The high resolution array (HiRA) for rare isotope beam experiments. *Nuclear Inst. and Methods in Physics Research, A*, 583(2-3):302–312, 2007.

[71] MS Wallace. *Experimental and Theoretical Challenges in Understanding the rp-Process on Accreting Neutron Stars*. PhD thesis, Michigan State University, 2005.

[72] G.L. Engel, M. Sadasivam, M. Nethi, J.M. Elson, L.G. Sobotka, and R.J. Charity. A multi-channel integrated circuit for use in low-and intermediate-energy nuclear physics-HINP16C. *Nuclear Inst. and Methods in Physics Research, A*, 573(3):418–426, 2007.

[73] G.F. Knoll. *Radiation Detection and Measurement*. Wiley, 3rd edition, 2000.

[74] A. Wagner, W. P. Tan, K. Chalut, R. J. Charity, B. Davin, Y. Larochelle, M. D. Lennek, T. X. Liu, X. D. Liu, W. G. Lynch, A. M. Ramos, R. Shomin, L. G. Sobotka, R. T. de Souza, M. B. Tsang, G. Verde, and H. S. Xu. Energy resolution and energy-light response of CsI(Tl) scintillators for charged particle detection. *Nuclear Instruments and Methods in Physics Research Section A: Accelerators, Spectrometers, Detectors and Associated Equipment*, 456(3):290–299, 2001.

[75] JF Ziegler. The Transport of Ions in Matter (TRIM), version 95.9. *IBM-Research, Yorktown, NY, USA*, 1995.

[76] A.S. Goldhaber. Statistical models of fragmentation processes. *Physics Letters B*, 53(4):306–308, 1974.

[77] M. R. Bhat and J. K. Tuli. Nuclear data sheets for $A = 69$. *Nuclear Data Sheets*, 90(2):269 – 390, 2000.

[78] J. A. Macdonald, J. C. Hardy, H. Schmeing, T. Faestermann, H. R. Andrews, J. S. Geiger, R. L. Graham, and K. P. Jackson. proton precursors : (I). the decay of ^{69}Se. *Nuclear Physics A*, 288(1):1–22, 1977.

[79] J. W. Arrison, D. P. Balamuth, T. Chapuran, D. G. Popescu, J. Görres, and U. J. Hüttmeier. Structure of the $N = Z + 1$ nucleus ^{69}Se. *Phys. Rev. C*, 40(5):2010–2023, Nov 1989.

[80] Ph. Dessagne, Ch. Miehé, P. Baumann, A. Huck, G. Klotz, M. Ramdane, G. Walter, and J. M. Maison. Erratum: β^+-electron-capture decay of ^{69}Se. *Phys. Rev. C*, 41(3):1319–1320, Mar 1990.

[81] K. R. Pohl, D. F. Winchell, J. W. Arrison, and D. P. Balamuth. Isomeric transitions in ^{69}Se and the spin of the ground state. *Phys. Rev. C*, 51(2):519–525, Feb 1995.

[82] C. J. Lister, P. J. Ennis, A. A. Chishti, B. J. Varley, W. Gelletly, H. G. Price, and A. N. James. Shape changes in $N = Z$ nuclei from germanium to zirconium. *Phys. Rev. C*, 42(4):R1191–R1194, Oct 1990.

[83] A. Gade, D. Bazin, A. Becerril, C. M. Campbell, J. M. Cook, D. J. Dean, D.-C. Dinca, T. Glasmacher, G. W. Hitt, M. E. Howard, W. F. Mueller, H. Olliver, J. R. Terry, and K. Yoneda. Quadrupole deformation of the self-conjugate nucleus ^{72}Kr. *Phys. Rev. Lett.*, 95(2):022502, Jul 2005.

[84] D. G. Jenkins, D. P. Balamuth, M. P. Carpenter, C. J. Lister, S. M. Fischer, R. M. Clark, A. O. Macchiavelli, P. Fallon, C. E. Svensson, N. S. Kelsall, and R. Wadsworth. Stability of oblate shapes in the vicinity of $N = Z = 34$ ^{68}Se: Bands in ^{69}Se and ^{67}As. *Phys. Rev. C*, 64(6):064311, Nov 2001.

[85] P. Urkedal and I. Hamamoto. Deformation and one-particle orbits in $^{36}_{71}\mathrm{Kr}_{35}$ and $^{35}_{71}\mathrm{Br}_{36}$. *Phys. Rev. C*, 58(4):R1889–R1892, Oct 1998.

[86] J. H. Hamilton, A. V. Ramayya, W. T. Pinkston, R. M. Ronningen, G. Garcia-Bermudez, H. K. Carter, R. L. Robinson, H. J. Kim, and R. O. Sayer. Evidence for coexistence of spherical and deformed shapes in ^{72}Se. *Phys. Rev. Lett.*, 32(5):239–243, Feb 1974.

[87] J. H. Hamilton, H. L. Crowell, R. L. Robinson, A. V. Ramayya, W. E. Collins, R. M. Ronningen, V. Maruhn-Rezwani, J. A. Maruhn, N. C. Singhal, H. J. Kim, R. O. Sayer, T. Magee, and L. C. Whitlock. Lifetime measurements to test the coexistence of spherical and deformed shapes in ^{72}Se. *Phys. Rev. Lett.*, 36(6):340–342, Feb 1976.

[88] S. M. Fischer, T. Anderson, P. Kerns, G. Mesoloras, D. Svelnys, C. J. Lister, D. P. Balamuth, P. A. Hausladen, and D. G. Sarantites. Shape coexistence in ^{71}Br and the question of the ground-state spin of ^{71}Kr. *Phys. Rev. C*, 72(2):024321, Aug 2005.

[89] R. G. Thomas. An analysis of the energy levels of the mirror nuclei, ^{13}C and ^{13}N. *Phys. Rev.*, 88(5):1109–1125, Dec 1952.

[90] Joachim B. Ehrman. On the displacement of corresponding energy levels of ^{13}C and ^{13}N. *Phys. Rev.*, 81(3):412–416, Feb 1951.

[91] K. Ogawa, H. Nakada, S. Hino, and R. Motegi. Thomas-Ehrman shifts in nuclei around ^{16}O and role of residual nuclear interaction. *Physics Letters B*, 464(3-4):157–163, 1999.

[92] B. A. Brown. private communication, 2009.

[93] G. Gamow. Zur quantentheorie des atomkernes. *Z. Physik*, 52:510, 1928.

[94] H. A. Bethe. Nuclear physics b. nuclear dynamics, theoretical. *Rev. Mod. Phys.*, 9(2):69, Apr 1937.

[95] C. M. Perey and F. G. Perey. Compilation of phenomenological optical-model parameters 1954-1975. *Atomic Data and Nuclear Data Tables*, 17(1):1–101, 1976.

[96] FD Becchetti and GW Greenlees. Nucleon-nucleus optical-model parameters, $A > 40$, $E < 50$ MeV. *Physical Review*, 182(4):1190–1209, 1969.

[97] I.M. Chakravarti, RG Laha, and J. Roy. *Handbook of Methods of Applied Statistics: Techniques of computation, descriptive methods, and statistical inference*. Wiley, 1967.

[98] E. Comay, I. Kelson, and A. Zidon. The Thomas-Ehrman shift across the proton dripline. *Physics Letters B*, 210(1-2):31–34, 1988.

[99] William D. Myers and Wladyslaw J. Swiatecki. Nuclear masses and deformations. *Nuclear Physics*, 81(1):1–60, 1966.

[100] M. Wiosna, J. Busch, J. Eberth, M. Liebchen, T. Mylaeus, N. Schmal, R. Sefzig, S. Skoda, and W. Teichert. Identification of excited levels in ^{69}Se and evidence for oblate deformed $g9/2$ bands in ^{69,71}Se. *Physics Letters B*, 200(3):255–258, 1988.

[101] S. M. Fischer, D. P. Balamuth, P. A. Hausladen, C. J. Lister, M. P. Carpenter, D. Seweryniak, and J. Schwartz. Evidence for collective oblate rotation in $N = Z$ ^{68}Se. *Phys. Rev. Lett.*, 84(18):4064–4067, May 2000.

[102] BNL national nuclear data center. Internet, 10 2009.

[103] David G. Jenkins. Waiting points in the astrophysical rp process: How unbound are ^{69}Br and ^{73}Rb. *Physical Review C (Nuclear Physics)*, 78(1):012801, 2008.

[104] J. Ekman, D. Rudolph, C. Fahlander, A. P. Zuker, M. A. Bentley, S. M. Lenzi, C. Andreoiu, M. Axiotis, G. de Angelis, E. Farnea, A. Gadea, Th. Kröll, N. Mărginean, T. Martinez, M. N. Mineva, C. Rossi-Alvarez, and C. A. Ur. Unusual isospin-breaking and isospin-mixing effects in the $A = 35$ mirror nuclei. *Phys. Rev. Lett.*, 92(13):132502, Apr 2004.

[105] TA Weaver, GB Zimmerman, and SE Woosley. Presupernova evolution of massive stars. *The Astrophysical Journal*, 225:1021, 1978.

[106] A. Heger, A. Cumming, and SE Woosley. Millihertz quasi-periodic oscillations from marginally stable nuclear burning on an accreting neutron star. *The Astrophysical Journal*, 665(2):1311–1320, 2007.

[107] Richard Cyburt et al. Unpublished. http://groups.nscl.msu.edu/jina/reaclib/db/.